Electrical and Energy Engineering

7 papers

Hour-Ahead and Day-Ahead Short-Term Load Forecasting for the Nepal Power System Using Statistical, LSTM and Hybrid Models

Ravi Lal Pokhrel[1], Basanta Kumar Gautam[1*]

[1]Department of Electrical Engineering, Pulchowk Campus, Institute of Engineering, Tribhuvan University
Lalitpur, Nepal
080mspse018.ravi@pcampus.edu.np; basanta.gautam@pcampus.edu.np
[*]Corresponding author:080mspse018.ravi@pcampus.edu.np

Abstract

Short-term load forecasting supports the daily scheduling and balancing of power systems, yet the choice between classical, deep-learning and hybrid methods depends on the forecast horizon and on the system studied. This study develops and compares five methods for the Nepal Electricity Authority (NEA) system at one-hour-ahead and 24-hour-ahead horizons: Simple Exponential Smoothing (SES), Double Exponential Smoothing (DES), Holt-Winters, a Long Short-Term Memory (LSTM) network and a hybrid Holt-Winters–LSTM model. Two years of hourly SCADA data (17,535 observations, 19 July 2024 to 19 July 2026) were combined with a regionally weighted national weather series built from elevation-classified Department of Hydrology and Meteorology stations, cyclical time features, and separate indicators for public holidays, festivals and weekly-off days. All methods were evaluated under one protocol with a chronological 80:20 split. The hybrid model, which supplies the Holt-Winters forecast to the LSTM as an additional input, achieved the lowest error at both horizons (hour-ahead: RMSE 98.73 MW, R^2 0.9552, MAPE 3.56%; day-ahead: RMSE 151.87 MW, R^2 0.8941, MAPE 6.30%). The plain LSTM clearly outperformed Holt-Winters at one hour ahead but was only marginally better at 24 hours ahead (RMSE 156.99 versus 157.84 MW). Margins between the leading methods are small, each neural network was trained once, and the study is retrospective and assesses forecast accuracy only.

Keywords: short-term load forecasting, LSTM, Holt-Winters, hybrid model, Nepal Electricity Authority

Introduction

Electricity cannot be stored economically at scale, so generation and demand must be balanced continuously and every scheduling decision rests on an estimate of demand that has not yet occurred. Load forecasting is conventionally classified by horizon, and short-term forecasting, covering roughly one hour to one week ahead, supports unit commitment, dispatch scheduling and day-to-day operational planning (Dong et al., 2024). The horizon determines which variables carry predictive information and therefore which methods are appropriate: recent load history, weather and calendar effects dominate at short horizons, whereas population, economic activity and policy dominate at long horizons.

A wide range of methods has been applied to short-term forecasting. Classical exponential-smoothing methods are inexpensive and interpretable and remain competitive benchmarks, deep-learning models such as the Long Short-Term Memory (LSTM) network can represent nonlinear relationships between load, weather and calendar variables but need more data and computation, and hybrids of the two are increasingly reported. Which is preferable is an empirical question

whose answer depends on the horizon, the data available and the characteristics of the system. Systematic reviews note that side-by-side evaluation of classical, deep-learning and hybrid methods across several horizons on a common dataset remains uncommon (Dong et al., 2024).

In Nepal, the Nepal Electricity Authority (NEA) is the state-owned utility responsible for generation, transmission, distribution and system operation, and its Load Dispatch Center (LDC) records the state of the national grid through SCADA and performs load forecasting principally for planning purposes (Nepal Electricity Authority [NEA], 2026). Published short-term studies for the Nepali system have generally evaluated a single model family at a single horizon (Bhandari et al., 2018; Dhakal, 2022). Nepal is also an unusual forecasting environment: its terrain spans about 60 m to over 8,000 m within a short horizontal distance, so no single weather station represents national conditions; its holiday calendar is dominated by lunar-calendar festivals whose Gregorian dates move from year to year; and its weekly-off convention changed during the study period.

This paper addresses the absence of a like-for-like comparison of classical statistical, deep-learning and hybrid short-term forecasting methods for the NEA system at more than one horizon. Its objective is to develop and compare five methods (SES, DES, Holt-Winters, LSTM and a hybrid Holt-Winters–LSTM model) at the hour-ahead and day-ahead horizons using one dataset, one feature set and one evaluation protocol. The contributions are (a) an elevation-based, regionally weighted national weather series for Nepal, (b) a calendar representation that separates public holidays, festivals and weekly-off days and accommodates the change in the weekly-off policy on 6 April 2026, and (c) a horizon-qualified comparison of the three method families for the Nepali system. The remainder of the paper reviews related work, describes the data and methods, presents and discusses the results, states the limitations and concludes.

Literature Review / Related Work

Statistical Methods, Machine Learning and LSTM

Before the widespread adoption of machine learning, load forecasting relied mainly on statistical time-series methods. Exponential smoothing remains a standard benchmark because it needs little data, fits quickly and is easy to interpret: SES tracks a level, DES adds a trend, and Holt-Winters adds a seasonal component that suits series with a strong repeating cycle, such as electricity load. Their small number of parameters, however, limits their ability to represent nonlinear interactions among several drivers, which motivates machine-learning methods. These treat forecasting as supervised regression from historical load, weather and calendar features to a future load value, and typically follow a workflow of preprocessing, a 70:30 or 80:20 train–test split, and validation with metrics such as MAPE and RMSE (Singla et al., 2019).

The LSTM is a recurrent network designed to remain trainable over long sequences. A memory cell carries information across time steps and is regulated by forget, input and output gates, which allows the network to preserve long-range dependencies that a standard recurrent network loses through vanishing gradients. This suits hourly load series, in which informative history extends from a few hours of autocorrelation to a full daily or weekly cycle.

Weather and Calendar Effects

Weather variables are common exogenous inputs, but the temperature–load relationship is not monotonic in general: it depends on the appliance stock and consumption behaviour of consumers, and weather variables are correlated with each other and with the time of day, which

complicates attribution of explanatory power. Calendar effects are a second standard source of information. Holidays are usually handled by a binary indicator, a separate similar-day model or adjustment factors. A single indicator assumes that all non-working days affect demand alike, which is questionable in Nepal, where gazetted public holidays close offices, banks and schools nationwide, many community festivals do not involve a general closure, and multi-day festivals such as Dashain and Tihar coincide with large changes in household activity.

Related Work

Singla et al. (2019) applied an artificial neural network to 24-hour-ahead forecasting with data from a 66 kV sub-station in Bathinda, India, and reported reasonably accurate forecasts. Other work has used fuzzy logic with extreme learning machines (Hassan et al., 2015) and ensemble methods for industrial and residential facilities (Porteiro et al., 2022). Abumohsen et al. (2023) compared LSTM, gated recurrent unit and plain recurrent architectures and found that LSTM and GRU achieved comparable accuracy and both outperformed a plain RNN, which supports LSTM as the deep-learning backbone used here. Ullah et al. (2022) combined a deep convolutional LSTM with a stacked GRU, and Dong et al. (2024) confirm in a comprehensive survey that hybrid deep-learning architectures have become dominant.

More recent studies span Transformer-based and hybrid statistical–deep-learning designs, including stacked Transformer–ANN–fuzzy models (Elakkiya et al., 2025), BiLSTM–Transformer hybrids with dynamic adaptive fusion (Xu et al., 2026), Transformer-based short-term forecasting (Zhao et al., 2021), CNN-LSTM hybrids (Ullah et al., 2024), LSTM-XGBoost hybrids (Sadik et al., 2026) and hybrid LSTM with online correction (Lu et al., 2024). Comparative and applied studies include ensemble deep learning for the Algerian market (Hadjout et al., 2022), comparisons of LSTM, CNN-LSTM and CNN-GRU models (Gunay et al., 2025), single-layer versus hybrid deep-learning techniques (Jang et al., 2024), LSTM-based short-term forecasts (Muzaffar & Afshari, 2019) and machine-learning forecasting reported at a recent engineering conference (Panda et al., 2025). Residential demand has been estimated from socio-economic factors (Ariyarathne et al., 2021) and with a PSO-tuned ANFIS that accounts for pandemic-era effects (Alam & Ali, 2024), and Martínez-Álvarez et al. (2015) survey data-mining techniques for electricity-related time series.

Within Nepal, Bhandari et al. (2018) applied an artificial neural network to short-term load forecasting for the Kathmandu Valley, and Dhakal (2022) forecast day-ahead peak demand for a single NEA distribution centre using deep learning. Neither study uses a systematically weighted, elevation-aware treatment of meteorological data, and neither compares hybrid statistical–deep-learning models against both classical and pure deep-learning baselines at more than one horizon.

Research Gap

Three gaps follow. First, deep-learning methods remain underexplored for load forecasting in Nepal. Second, existing Nepali work uses a single weather station or an unweighted station average despite strong elevation-driven climate variation, and represents holiday effects, when at all, by a single undifferentiated indicator. Third, few studies compare classical, deep-learning and hybrid approaches side by side at more than one horizon on one dataset and protocol (Dong et al., 2024). This study addresses all three.

Materials and Methods

Data Sources

Two secondary data sources were combined at hourly resolution over 19 July 2024 to 19 July 2026. Electrical data were extracted from the SCADA system of NEA's Load Dispatch Center (LDC), Syuchatar (NEA, 2026). The extract contains frequency, export, import, generation, total national load and total system load, and the forecasting target throughout is the SCADA-computed total system load (System_Load) used operationally by the LDC. The record comprises 17,535 hourly observations from 19 July 2024 00:00 to 19 July 2026 14:00, with no missing or duplicated timestamps and no missing values. Hourly temperature, humidity and precipitation, with station coordinates and elevations, were obtained from the automatic weather station network of the Department of Hydrology and Meteorology (DHM, 2024–2026). Weather values were available for every SCADA timestamp, so merging on the hourly timestamp required no imputation and gave 17,535 complete rows.

Regionally Weighted Weather Series

Each DHM station was assigned to the Terai (60–600 m), Hill (600–3,000 m) or Mountain (above 3,000 m) zone using its DHM-supplied elevation. Hill and Mountain stations were pooled into one Hill + Mountain group because only three Mountain stations report temperature and because the available regional load information separates the Terai from the rest of the country. After pooling, 48 Terai and 92 Hill + Mountain stations reported temperature, 54 and 130 reported humidity, and 100 and 238 reported precipitation. At each hour a simple mean across reporting stations was taken within each group, and the two means were combined into a national value for each variable using daily weights (Equation 1).

(1)

where $W(t)$ is the weighted national value at hour t, d is the calendar day containing t, $s_T(d)$ and $s_{HM}(d)$ are the Terai and Hill + Mountain shares of regional load on day d (fractions summing to 1), and $Terai_{avg}(t)$ and $HM_{avg}(t)$ are the zonal station means at hour t.

The daily shares come from regional load records that the LDC made available during a site visit. Records were not available for every day, and the shares for the remaining days were filled in by the author by interpolation between neighbouring recorded values. The result is 731 daily shares in which the Terai share ranges from 62% to 75% (mean 68.5%), applied to all 24 hours of each day. The shares are an approximation used only to construct an exogenous weather input; they are not applied to the load data and do not affect the forecasting target, and measured and interpolated days are not separately flagged in the final series.

Calendar Features

Hour of day and day of week were encoded as sine–cosine pairs (periods of 24 and 7) so that adjacent hours and days remain numerically close. Three separate binary indicators were constructed instead of a single non-working-day flag: Public_Holiday_Flag (gazetted nationwide public holidays), Festival_Flag (community, regional or group-specific festivals) and Weekly_Off_Flag (weekly-off days under the policy in force). The holiday calendar was compiled from Nepal Gazette and Ministry of Home Affairs notices for 2081 and 2082 B.S. and 2083 B.S. cabinet notices, cross-checked against published Nepali calendar listings (Hamro Patro, 2024–2026), and converted to Gregorian dates because the major festivals follow lunar

and lunisolar calendars. Two observances that are not days off (Ethnic Discrimination and Untouchability Eradication Day and Civil Service Day) were excluded.

Nepal's weekly holiday was Saturday only until the Cabinet declared Saturday and Sunday the weekly public holiday for government offices and schools, effective 6 April 2026. The weekly-off indicator is therefore defined piecewise about the cut-off date t_c = 6 April 2026 (Equation 2). Table 1 summarises the coverage of the three indicators. The indicators are overlapping rather than mutually exclusive (three dates carry both a public-holiday and a festival flag), and the two-day weekend covers only the final fifteen weeks of the record.

(2)

Table 1

Calendar Indicator Coverage of the Study Period

Indicator	Days flagged	Hours flagged	Share of record
Public_Holiday_Flag	59	1,416	8.08%
Festival_Flag	28	672	3.83%
Weekly_Off_Flag	—	2,871	16.37%
of which Saturdays	105	2,520	14.37%
of which Sundays (from 6 April 2026)	15	351	2.00%

Note. Computed on the 17,535-hour modelling dataset. The weekly-off total is the sum of Saturday and Sunday hours.

Data Preparation and Leakage Safeguards

The model input consists of lagged System_Load, the three weighted weather variables, the four cyclical time features and the three calendar indicators; the hybrid model adds the Holt-Winters forecast as one further feature. The data were split chronologically 80:20, training on the earlier portion and testing on the most recent 20% (roughly 3,500 hourly observations), consistent with common practice (Singla et al., 2019). All variables were min–max scaled to [0, 1] using bounds computed on the training portion only. Overlapping sliding windows of w past hours of all features were paired with the load h hours beyond the end of the window (Equation 3).

(3)

where x_i is the vector of input features at hour i, w is the lookback window, h is the forecast horizon, and $f(\cdot)$ is the mapping learned by the network or, for the classical methods, the corresponding smoothing-based forecast. Table 2 gives the configuration at each horizon. No smoothing was applied to the target series at either horizon, and weather enters the models only as observed past values within the window; no forecast weather is used.

Table 2

Experimental Configuration at the Two Forecast Horizons

Parameter	Hour-ahead	Day-ahead
Forecast horizon h	1 hour	24 hours (same hour, next day)
Lookback window w	60 hours	72 hours
Train : test split	80 : 20, chronological	80 : 20, chronological
Seasonal period p (classical models)	24 hours	24 hours
Target series	Raw hourly System_Load	Raw hourly System_Load

Note. Both horizons use the same dataset, feature set and evaluation protocol.

Information leakage was guarded against at each stage. Input windows end h hours before the target. The smoothing parameters of SES, DES and Holt-Winters were fitted on the training portion only, and every forecast for hour t is produced from the smoothing state at origin t − h, using only observations available at that origin. The Holt-Winters feature supplied to the hybrid model is the same h-step-ahead forecast. The validation set used for early stopping is the final 10% of the training array. One asymmetry should be noted: because an h-step-ahead classical forecast has no valid origin until h steps into the series, the hybrid's input frame omits the first h rows, so its test set begins one hour later at the hour-ahead horizon and up to nineteen hours later at the day-ahead horizon, out of roughly 3,500 hours.

Forecasting Models

Five methods were developed at each horizon. SES, DES and Holt-Winters with multiplicative seasonality (p = 24 hours) were implemented with direct h-step-ahead forecasts from the smoothing state h steps back rather than by chaining one-step forecasts. For Holt-Winters the forecast is given by Equation 4, where E_t, T_t and S are the smoothed level, trend and seasonal index and p is the seasonal period. The smoothing parameters were fitted by numerical minimisation of the sum of squared h-step-ahead errors on the training portion, separately for each horizon.

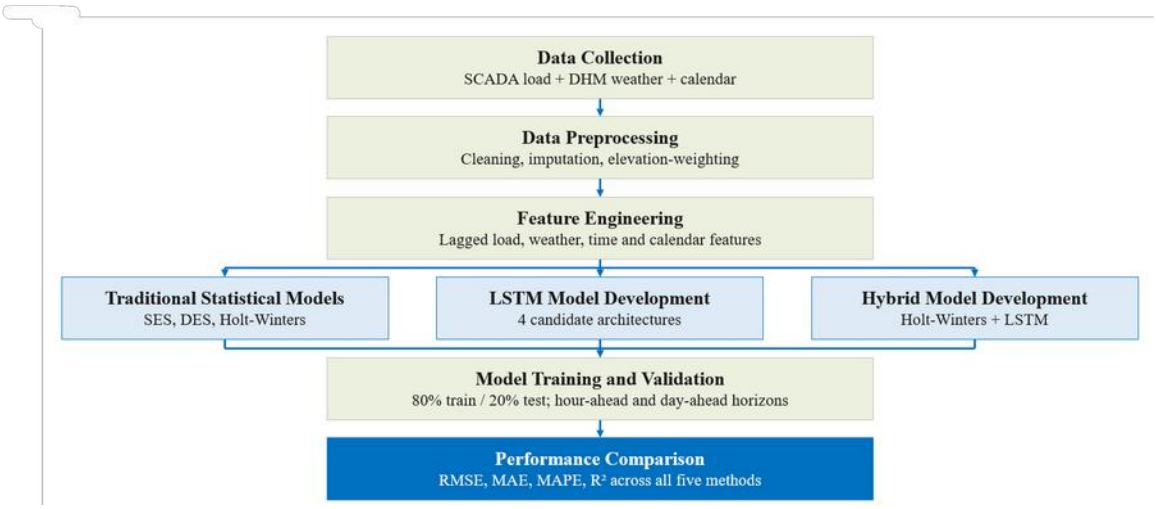
(4)

Four candidate LSTM architectures, each a single LSTM layer of 40 units followed by a stack of dense layers with a linear output (Appendix A, Table A1), were trained independently at each horizon. They differ in the number of dense layers and in the mix of sigmoid and ReLU activations, so that differences are attributable to the dense head rather than to recurrent capacity. The architecture with the highest test-set R^2 at each horizon was carried forward as the representative LSTM and as the neural component of the hybrid. The hybrid model retrains that architecture on every input of the plain LSTM plus the Holt-Winters h-step-ahead forecast for the corresponding hour, and predicts the actual load directly rather than a residual correction.

Training and Implementation

The LSTM and hybrid models were trained with the Adam optimiser, mean-squared-error loss and a batch size of 32, for at most 150 epochs. Early stopping monitored validation loss only after a 50-epoch warm-up, with a patience of 12 epochs and restoration of the best weights, and the learning rate was halved after six epochs without improvement (floor 1×10^{-5}). Fixed random seeds were set for NumPy and TensorFlow. Among the runs reported, training lasted between about 63 and 82 epochs, so no run reached the ceiling. Data preparation and modelling were implemented in Python 3.12.13 with pandas, NumPy, SciPy, scikit-learn, Matplotlib and TensorFlow 2.20.0 (Keras), and executed in a Kaggle notebook with a GPU accelerator (Tesla T4 × 2). Figure 1 summarises the pipeline.

Figure 1



Methodology pipeline from data collection to performance comparison

Evaluation Metrics

All models at both horizons were evaluated on the held-out test set using RMSE, MAE, MAPE and R^2 (Equations 5–8).

(5)

(6)

(7)

(8)

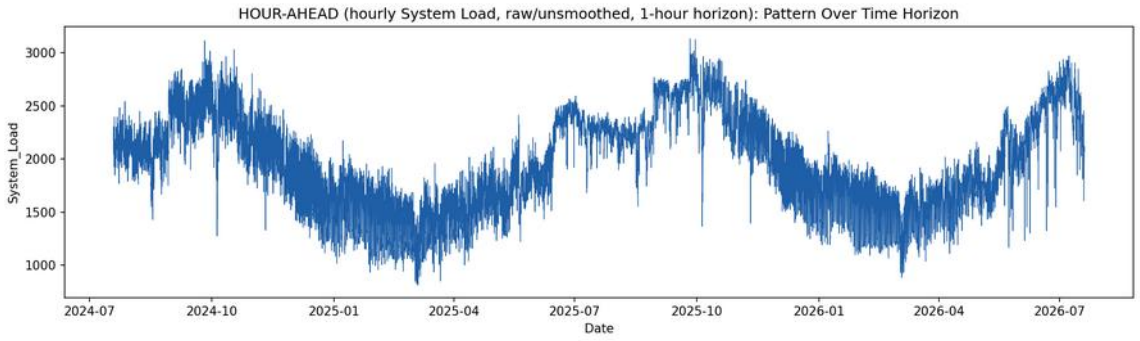
where y_i is the actual load, $\hat{y}_i$ the predicted load, $\bar{y}$ the mean actual load and n the number of test observations. RMSE and MAE are in MW; MAPE is a percentage of actual load; R^2 is the proportion of load variance explained. All four are reported because they weigh errors differently and may disagree on the ranking of close methods.

Results

Load Pattern and Descriptive Statistics

Mean hourly System_Load was 1,956.01 MW (SD = 452.32 MW; median = 1,942.03 MW), ranging from 813.76 MW in off-peak hours to 3,130.42 MW at peak. Figure 2 shows two annual peaks around October separated by a trough around February and March, superimposed on a strong daily cycle. The hourly distribution is visibly bimodal, consistent with the sharp daily ramps.

Figure 2



Raw hourly System Load over the observation period (19 July 2024 to 19 July 2026)

Correlation and Calendar Analysis

Table 3 and Figure 3 report Pearson correlations between System_Load and the candidate features. Temperature shows the strongest linear association (r = 0.494), followed by precipitation (r = 0.321) and humidity (r = 0.290), whereas all calendar and time features have |r| below about 0.09. These coefficients measure linear association only over the whole record; they do not establish causation, they absorb seasonality (the warmest and wettest months coincide with the monsoon and the autumn demand peak), and weather variables are correlated with each other and with the time of day (for example, temperature with Hour_cos at −0.340 and humidity with Hour_cos at 0.480). A weak coefficient for hour-of-day does not imply an unimportant feature, because load depends on hour through a shape rather than a straight line.

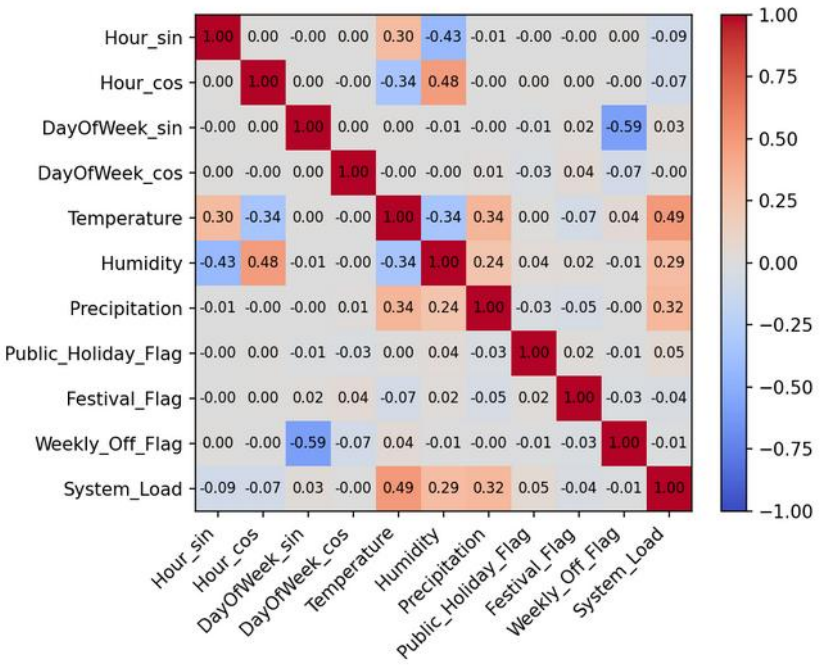
Table 3

Pearson Correlation of System Load With Candidate Features

Feature	Correlation with System_Load
Temperature	0.494
Precipitation	0.321
Humidity	0.290
Public_Holiday_Flag	0.053
DayOfWeek_sin	0.028
DayOfWeek_cos	−0.002
Weekly_Off_Flag	−0.015
Festival_Flag	−0.037
Hour_cos	−0.074
Hour_sin	−0.086

Note. Pearson r computed over all 17,535 hourly observations.

Figure 3



Correlation heat-map of System Load, weather and calendar features

Table 4 compares mean load on each category of day with ordinary working hours (hours with none of the three indicators), unadjusted and within calendar months. For public holidays the two comparisons disagree in sign: Dashain and Tihar fall in autumn, the annual demand peak, so the unadjusted comparison is dominated by season, and within the same month public-holiday hours sit about 27 MW below working hours. The three categories therefore differ from ordinary working hours by different amounts, which supports representing them as separate features, but the table does not quantify the effect of any category on forecast accuracy.

Table 4

Mean Hourly System Load by Calendar Category

Category	Hours	Mean load (MW)	Unadjusted difference (MW)	Within-month difference (MW)
Ordinary working hours	12,936	1,953.6	—	—
Public holiday hours	1,416	2,036.9	+83.3	−26.9
Festival hours	672	1,872.9	−80.8	−0.6
Weekly-off hours	2,871	1,940.7	−12.9	−34.5

Note. Differences are relative to ordinary working hours. The within-month difference compares each category with working hours of the same calendar month; it does not control for hour of day, weather or position within a multi-day festival.

LSTM Architecture Selection

At the day-ahead horizon the four architectures performed similarly (R^2 from 0.8751 to 0.8868). Model 3 had the lowest RMSE (156.99 MW), the highest R^2 (0.8868) and the lowest MAE (113.36 MW), and was selected. At the hour-ahead horizon the architectures were almost indistinguishable (R^2 from 0.9530 to 0.9536, RMSE spread of 0.62 MW), and Model 2 (RMSE

100.51 MW, R^2 0.9536) was selected, although on so narrow a spread the selection carries little information. Full results are in Appendix A (Tables A2 and A3).

Comparison of All Methods

Tables 5 and 6 compare the five methods at the two horizons. Among the classical methods, Holt-Winters led on RMSE and R^2 at both horizons. At the day-ahead horizon it was clearly the strongest (RMSE 157.84 MW), ahead of SES (164.32 MW) and DES (181.72 MW). At the hour-ahead horizon its MAE (72.73 MW) was slightly higher than that of SES (71.52 MW) and DES (71.59 MW) even though its RMSE was lower (109.02 MW), indicating that it reduced large errors more than typical ones.

Table 5

Forecast Accuracy of All Methods, Hour-Ahead Horizon

Method	RMSE (MW)	R^2	MAE (MW)	MAPE (%)
SES	114.02	0.9403	71.52	4.02
DES	114.21	0.9401	71.59	4.03
Holt-Winters	109.02	0.9454	72.73	3.93
LSTM (Model 2)	100.51	0.9536	67.18	3.65
Hybrid (Holt-Winters + LSTM)	98.73	0.9552	64.75	3.56

Note. RMSE = root mean squared error; MAE = mean absolute error; MAPE = mean absolute percentage error. Metrics are computed on the held-out chronological test set (about 3,500 hourly observations).

Table 6

Forecast Accuracy of All Methods, Day-Ahead Horizon

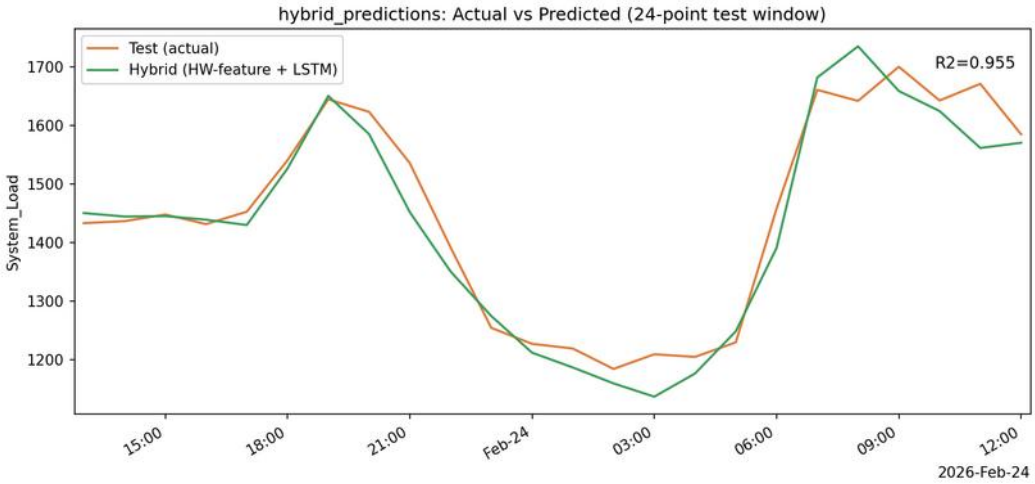
Method	RMSE (MW)	R^2	MAE (MW)	MAPE (%)
SES	164.32	0.8760	118.08	6.42
DES	181.72	0.8484	131.29	7.16
Holt-Winters	157.84	0.8856	115.87	6.39
LSTM (Model 3)	156.99	0.8868	113.36	6.40
Hybrid (Holt-Winters + LSTM)	151.87	0.8941	111.97	6.30

Note. RMSE = root mean squared error; MAE = mean absolute error; MAPE = mean absolute percentage error. Metrics are computed on the held-out chronological test set (about 3,500 hourly observations).

At the hour-ahead horizon (Table 5), the hybrid model ranked first on every metric (RMSE 98.73 MW, R^2 0.9552, MAE 64.75 MW, MAPE 3.56%), improving on the plain LSTM by 1.77 MW of RMSE (about 1.8%) and on Holt-Winters by about 9.4%. Both neural models beat all three classical methods on every metric, and the plain LSTM improved on Holt-Winters by about 7.8% of RMSE. At the day-ahead horizon (Table 6), the hybrid again ranked first on every metric (RMSE 151.87 MW, R^2 0.8941, MAE 111.97 MW, MAPE 6.30%), improving on the plain LSTM by 5.12 MW (about 3.3%) and on Holt-Winters by 5.97 MW (about 3.8%). The plain LSTM and Holt-Winters were close: the LSTM had the lower RMSE (by 0.85 MW, about 0.5%), higher R^2 and lower MAE, whereas Holt-Winters had a marginally lower MAPE (6.39% against 6.40%). By RMSE the day-ahead ordering is Hybrid, LSTM, Holt-Winters, SES, DES. All methods were substantially more accurate one hour ahead than 24 hours ahead, with MAPE

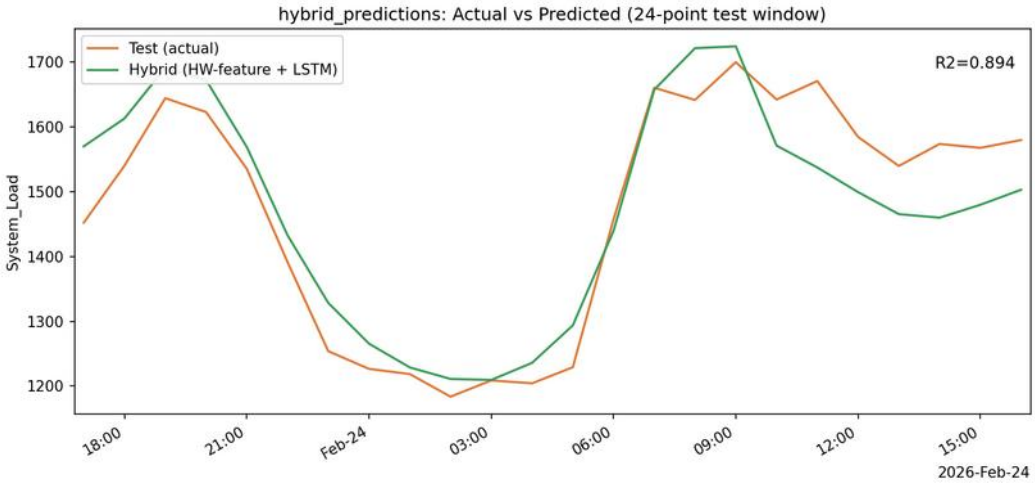
falling from roughly 6.3–7.2% to roughly 3.6–4.0%. Figures 4 and 5 show the hybrid forecasts over a 24-hour test window at the two horizons.

Figure 4



Hybrid Holt-Winters–LSTM, hour-ahead: actual versus predicted load over a 24-hour test window

Figure 5



Hybrid Holt-Winters–LSTM, day-ahead: actual versus predicted load over a 24-hour test window

Discussion

The hybrid Holt-Winters–LSTM model achieved the lowest error of the five methods at both horizons, but the margins are small and each neural model was trained once, so the result is consistent with, rather than conclusive proof of, a genuine advantage. The improvement of the hybrid over the plain LSTM was smaller at the hour-ahead horizon (about 1.8%) than at the day-ahead horizon (about 3.3%), and both are small relative to the spread between architectures at the day-ahead horizon (Appendix A).

The standing of the plain LSTM depends on the horizon. At one hour ahead it beat every classical method on every metric, whereas at 24 hours ahead it was within about 0.5% of Holt-Winters in RMSE and behind it on MAPE. A plausible reading, consistent with the structure of the methods, is that a 24-hour-ahead forecast of an hourly series is largely a request to reproduce the daily cycle one period forward, which Holt-Winters encodes explicitly through its multiplicative seasonal index while the LSTM must infer it from a 72-hour window. That the hybrid, which has access to both the learned representation and the explicit seasonal projection, outperformed each of its components is consistent with this reading. It is offered as an interpretation of the design of the methods and not as a demonstrated mechanism, because no ablation isolating the Holt-Winters feature was run. This result qualifies the common expectation that deep-learning models dominate classical baselines at every horizon, and it agrees with the observation that cross-horizon comparisons are scarce (Dong et al., 2024).

The ordering among the classical methods follows their structure. DES was weakest at the day-ahead horizon because its linear trend is extrapolated 24 steps in a series whose dominant structure is cyclical, and SES was penalised less because the level one day ahead is on average close to the current level. At one hour ahead the three classical methods converge because a one-step forecast is anchored to the most recent observation, and the same reason explains why all methods are far more accurate at that horizon and why dense-layer depth was not a meaningful lever there. The finding that LSTM and GRU variants outperform plain recurrent networks (Abumohsen et al., 2023) supports the choice of backbone, but the present results show that on this system the backbone alone is not enough to dominate a well-fitted seasonal benchmark at 24 hours.

The weather and calendar analysis is descriptive. Temperature carried the most linear signal, but the correlations absorb seasonality and the diurnal cycle, and at the day-ahead horizon the observed weather in the window is at least 24 hours old relative to the target, which limits what it can contribute. The sign reversal of the public-holiday difference between the unadjusted and within-month comparisons shows why raw group means cannot assign a direction of effect to a calendar category and why a single undifferentiated indicator is inadequate; the contribution of the weather weighting and of the three-way holiday representation to forecast accuracy, however, was not isolated. Compared with earlier Nepali studies that evaluated one model family at one horizon (Bhandari et al., 2018; Dhakal, 2022), the practical implication is that Holt-Winters is a cheap and strong benchmark, and any claim that a deep-learning method is preferable for the NEA system should be qualified by horizon and by the size of the margin.

Limitations

Several limitations qualify the findings. First, the regional shares used to weight the weather series are partly measured and partly interpolated, are not flagged by day, are applied uniformly to all 24 hours of a day, and are an approximation rather than a measured hourly regional load series; the sensitivity of accuracy to the weights was not tested. Second, the study uses about two years of data, which covers the annual cycle only twice and gives a weak basis for inter-annual variability; an atypical monsoon or festival season is absorbed into what the models treat as normal. Third, no forecast weather is used, so the evaluation does not include weather-forecast error. Fourth, the two-day weekend took effect on 6 April 2026, so the models have almost no training exposure to it and no conclusion about the policy change can be drawn. Fifth, each architecture was trained once with a fixed seed, architecture selection used test-set R^2, and no

repeated-seed variance estimate is available, so architecture rankings are indicative. Sixth, no ablation experiment was performed, so the contribution of individual feature groups is not quantified. Finally, population growth, economic growth, electrification and tariffs are not represented, the evaluation is retrospective, and no operational, market or economic outcome is assessed.

Conclusion

This study compared five short-term load forecasting methods for the NEA system at one-hour-ahead and 24-hour-ahead horizons under a common dataset, feature set and protocol, using two years of hourly SCADA data, an elevation-weighted national weather series and a calendar representation that separates public holidays, festivals and weekly-off days. A hybrid model that supplies the Holt-Winters forecast to the LSTM as an additional input achieved the lowest error at both horizons (RMSE 98.73 MW and 151.87 MW). The plain LSTM held a clear advantage over Holt-Winters at one hour ahead (about 7.8% of RMSE) but only a marginal one at 24 hours ahead (about 0.5%), so conclusions drawn at one horizon do not transfer to the other, and Holt-Winters remains a strong benchmark at the day-ahead horizon.

The margins between the leading methods are small and rest on a single training run per model, so the findings are specific to this dataset and configuration. Future work should obtain a longer, continuous measured regional load series so that interpolation of the weather-weighting shares is unnecessary, test the sensitivity of accuracy to the weighting, run ablations of the weather and calendar feature groups with repeated seeds, and, if the work is extended to medium- and long-term forecasting, incorporate population and economic growth.

Acknowledgments

The authors thank the Department of Electrical Engineering, Pulchowk Campus, Institute of Engineering, Tribhuvan University, for academic support; the Load Dispatch Center of the Nepal Electricity Authority, Syuchatar, for the SCADA records and the regional load information; and Mr. Ashok Bakhrel, Meteorologist, Nepal Meteorological Department, for providing the meteorological data and station information.

Funding

The author(s) received no financial support for the research, authorship, or publication of this paper.

Conflict of Interest

The authors declare no conflict of interest.

Author Contributions

Ravi Lal Pokhrel: conceptualization, methodology, software, validation, formal analysis, investigation, data curation, writing original draft, visualization.

Basanta Kumar Gautam: conceptualization, supervision, writing review and editing, project administration.

Data Availability

The SCADA data were obtained from the Load Dispatch Center of the Nepal Electricity Authority and the meteorological data from the Department of Hydrology and Meteorology, Government of Nepal. Both organizations have requested that the data not be shared, so the datasets are not publicly available.

Ethical Approval / Consent

Not applicable. The study used only aggregate power-system and meteorological records and involved no human participants, animals or personal data.

References

Abumohsen, M., Owda, A. Y., & Owda, M. (2023). Electrical load forecasting using LSTM, GRU, and RNN algorithms. *Energies, 16*(5), Article 2283. https://doi.org/10.3390/en16052283

Alam, S. M. M., & Ali, M. H. (2024). Residential load forecasting by a PSO-tuned ANFIS2 method considering the COVID-19 influence. *Frontiers in Energy Research, 11*, Article 1292183. https://doi.org/10.3389/fenrg.2023.1292183

Ariyarathne, Y. S. S., Jayatissa, N. W. K., & De Silva, D. S. M. (2021). Domestic electricity usage estimation model using socio-economic factors for Sri Lanka. *Journal of Science, University of Kelaniya, 14*, 17–30. https://doi.org/10.4038/josuk.v14i0.8031

Bhandari, B., Shakya, S. R., & Jha, A. K. (2018). Short term electric load forecasting of Kathmandu Valley of Nepal using artificial neural network. *Kathford Journal of Engineering and Management, 1*(1), 43–48.

Department of Hydrology and Meteorology. (2024–2026). *Meteorological data: Temperature, relative humidity, precipitation and station elevation*. Government of Nepal. https://www.dhm.gov.np

Dhakal, O. P. (2022). *Day ahead peak electricity demand forecasting of Panchkhal Distribution Center of Nepal Electricity Authority (NEA) using deep learning* [Master's thesis, Tribhuvan University, Institute of Engineering, Pulchowk Campus].

Dong, Q., Huang, R., Cui, C., Towey, D., Zhou, L., Tian, J., & Wang, J. (2024). *Short-term electricity-load forecasting by deep learning: A comprehensive survey* (arXiv:2408.16202). arXiv. https://doi.org/10.48550/arXiv.2408.16202

Elakkiya, E., Antony Raj, S., Balakrishnan, A., Sanisetty, B., & Bandaru, R. B. (2025). Stacked hybrid model for load forecasting: Integrating transformers, ANN, and fuzzy logic. *Scientific Reports, 15*, Article 19688. https://doi.org/10.1038/s41598-025-04210-1

Gunay, M., Yildirim, O., & Demir, Y. (2025). Deep learning-based approaches for short-term residential electricity consumption prediction: A comparative study of LSTM, CNN-LSTM, and CNN-GRU models. In *Proceedings of the 11th World Congress on Electrical Engineering and Computer Systems and Science (EECSS'25)* (Paper EEE 112). https://doi.org/10.11159/eee25.112

Hadjout, D., Torres, J. F., Troncoso, A., Sebaa, A., & Martínez-Álvarez, F. (2022). Electricity consumption forecasting based on ensemble deep learning with application to the

Algerian market. *Energy, 243*, Article 123060. https://doi.org/10.1016/j.energy.2021.123060

Hamro Patro. (2024–2026). *Nepali calendar and public holidays*. https://www.hamropatro.com

Hassan, S., Khosravi, A., & Jaafar, J. (2015). Training of interval type-2 fuzzy logic system using extreme learning machine for load forecasting. In *Proceedings of the 9th International Conference on Ubiquitous Information Management and Communication (IMCOM '15)*. ACM. https://doi.org/10.1145/2701126.2701177

Jang, J., Kim, B., & Kim, I. (2024). Comparative analysis of deep learning techniques for load forecasting in power systems using single-layer and hybrid models. *International Transactions on Electrical Energy Systems, 2024*, Article 5587728. https://doi.org/10.1155/2024/5587728

Lu, N., Ouyang, Q., Li, Y., & Zou, C. (2024). *Electrical load forecasting model using hybrid LSTM neural networks with online correction* (arXiv:2403.03898). arXiv. https://doi.org/10.48550/arXiv.2403.03898

Martínez-Álvarez, F., Troncoso, A., Asencio-Cortés, G., & Riquelme, J. C. (2015). A survey on data mining techniques applied to electricity-related time series forecasting. *Energies, 8*(11), 13162–13193. https://doi.org/10.3390/en81112361

Muzaffar, S., & Afshari, A. (2019). Short-term load forecasts using LSTM networks. *Energy Procedia, 158*, 2922–2927. https://doi.org/10.1016/j.egypro.2019.01.952

Nepal Electricity Authority. (2026). *A year in review: Fiscal year 2025/2026*. https://www.nea.org.np

Panda, S. K., Panda, M. K., Sahoo, P. K., Rout, D. K., & Shah, H. A. (2025). Short term load forecasting using machine learning technique. In *Proceedings of the Parul University International Conference on Engineering and Technology (PiCET 2025)*. https://doi.org/10.1049/icp.2025.1667

Porteiro, R., Hernández-Callejo, L., & Nesmachnow, S. (2022). Electricity demand forecasting in industrial and residential facilities using ensemble machine learning. *Revista Facultad de Ingeniería Universidad de Antioquia*(102), 9–25. https://doi.org/10.17533/udea.redin.20200584

Sadik, Y., Nejmi, A., Oumiguil, L., & Baite, M. (2026). Forecasting energy consumption using a hybrid LSTM-XGBoost model. *Engineering Proceedings, 144*, Article 4. https://doi.org/10.3390/engproc2026144004

Singla, M. K., Gupta, J., Nijhawan, P., & Oberoi, A. S. (2019). Electrical load forecasting using machine learning. *International Journal of Advanced Trends in Computer Science and Engineering, 8*(3), 615–619. https://doi.org/10.30534/ijatcse/2019/45832019

Ullah, F. U. M., Ullah, A., Khan, N., Lee, M. Y., Rho, S., & Baik, S. W. (2022). Deep learning-assisted short-term power load forecasting using deep convolutional LSTM and stacked GRU. *Complexity, 2022*, Article 2993184. https://doi.org/10.1155/2022/2993184

Ullah, K., Ahsan, M., Hasanat, S. M., Haris, M., Yousaf, H., Raza, S. F., Tandon, R., Abid, S., & Ullah, Z. (2024). Short-term load forecasting: A comprehensive review and simulation study with CNN-LSTM hybrids approach. *IEEE Access, 12*, 111858–111881. https://doi.org/10.1109/ACCESS.2024.3440631

Xu, J., Zhang, L., & Zhang, Z. (2026). Research on BiLSTM–Transformer power load forecasting method based on dynamic adaptive fusion. *Energies, 19*(6), Article 1473. https://doi.org/10.3390/en19061473

Zhao, Z., Xia, C., Chi, L., Chang, X., Li, W., Yang, T., & Zomaya, A. Y. (2021). Short-term load forecasting based on the Transformer model. *Information, 12*(12), Article 516. https://doi.org/10.3390/info12120516

Appendix A

This appendix reports the candidate LSTM architectures and the complete model-selection results that support the selection of the representative LSTM at each horizon (see Materials and Methods and Results).

Table A1

Candidate LSTM Architectures Evaluated

Model	Architecture
Model 1	LSTM(40) → Dense(30, sigmoid) → Dense(20, sigmoid) → Dense(1, linear)
Model 2	LSTM(40) → Dense(20, relu) → Dense(10, sigmoid) → Dense(1, linear)
Model 3	LSTM(40) → Dense(30, relu) → Dense(15, relu) → Dense(10, sigmoid) → Dense(1, linear)
Model 4	LSTM(40) → Dense(20, relu) → Dense(15, relu) → Dense(10, relu) → Dense(10, sigmoid) → Dense(1, linear)

Note. All candidates share a single LSTM layer of 40 units; the final layer is linear because the task is regression.

Table A2

LSTM Model-Selection Results, Day-Ahead Horizon

Model	RMSE (MW)	R^2	MAE (MW)	MAPE (%)
Model 1	164.95	0.8751	119.17	6.68
Model 2	159.03	0.8839	113.68	6.37
Model 3 (selected)	156.99	0.8868	113.36	6.40
Model 4	157.20	0.8865	113.72	6.37

Note. Selection was based on the highest test-set R^2. Each architecture was trained once with a fixed seed.

Table A3

LSTM Model-Selection Results, Hour-Ahead Horizon

Model	RMSE (MW)	R^2	MAE (MW)	MAPE (%)
Model 1	101.03	0.9531	67.24	3.687
Model 2 (selected)	100.51	0.9536	67.18	3.648
Model 3	101.13	0.9530	67.40	3.681
Model 4	100.81	0.9533	67.32	3.681

Note. Selection was based on the highest test-set R^2. Each architecture was trained once with a fixed seed.

LONG RANGE REMOTE MONITORING AND REAL TIME DATA TRANSMISSION FOR HYDROPOWER APPLICATIONS

Aavanish Koirala[1], Arshia Joshi[2*], Bishal Sah[3*], Sanjay Rizal[4*], Sushant Poudel[5*]

Department of Electrical and Electronics Engineering, Kathmandu University
Dhulikhel, Nepal
aavanishk@gmail.com
[*2]arshia3824@student.ku.edu.np, [*3]bs22051321@student.ku.edu.np, *[4]sanjayrizal77@gmail.com,
[*5]sushantpoudel523@gmail.com

Abstract

In developing countries like Nepal, Hydropower sector lack proper means of communication to relay the status of reservoir to the control personnel. The wired communication infrastructure can be difficult and costly to deploy, particularly in hilly regions of Nepal. This study proposes a low-power, long-range wireless system based on LoRa communication for transmitting reservoir data from a remote sensing location to the control room. The proposed system consists of a remote monitoring node with multiple sensors, a microcontroller based LoRa transmitter, and a receiving gateway connected to a control-room monitoring interface using SX1262 LoRa Module. The system is designed to take reservoir parameters at certain intervals and transmit the measurements wirelessly to the control room for real-time visualization, data logging as well as alarm generation.

Communication performance is evaluated in terms of transmission latency, communication range, and signal to noise ratio, data reliability under various environmental conditions. The proposed approach aims to provide a cost effective solution for remote hydropower monitoring and can potentially be extended to multiple sensing module for reservoir, gate, and environmental parameter monitoring.

Keywords: LoRa, Latency, Signal to Noise Raio, Transmitter, Receiver

Introduction

The hydropower projects in countries like Nepal are often located in geographically challenging areas making the communication between reservoirs and control rooms unreliable. Establishing a wired communication system can be a challenge in such an area. Thus, low power and long range reliable wireless communication could support remote observation of reservoirs.

Long Range radio technology is designed for low power and long range communication and by now has been studied for rural connectivity in Nepal (Pandey et al.,2023). Work on relay assisted communication for remote environments provides basis for considering intermediate nodes where a direct radio link is obstructed (Haniz et al., 2022). These study shows the relevance of LoRa communication in monitoring applications.

The main question in this study is weather a LoRa-based prototype is useful tool for hydropower applications. The paper contains the prototype design of a LoRa based communication and monitoring system along with the analysis and study of various communication parameters such as latency, packet delivery ratio, packet loss, received signal strength and variation of such parameters with spreading factor.

The study has three major aims. First, the study gives a prototype architecture to transmit the parameters and readings among nodes and establishing a link. Second, it tests the various communication indicators across various distance range and latency at spreading factors SF7, SF9 and SF11. Third, it discusses the system's potential application to remote hydropower monitoring in context of Nepal.

Research Questions and Objectives

The study involved the following research questions:

- How does the distance and communication link conditions affects RSSI, SNR, PDR, packet loss and latency in developing the prototype?
- How are the packet delivery reliability and latency affected by spreading factors in tested parameters?
- What practical and regulatory considerations should be addressed before deployment of such systems?

To answer these questions, the major objectives of the paper includes the development of a prototype and establishment of the link between the communication nodes, evaluation of the communication parameters using the module and study of the consideration of selected frequency band in context of Nepal.

Literature Review / Related Work

Pandey et al. (2023) presented a LoRa-based communication system for monitoring water quality in lakes and reservoirs. Their work highlights the application of long-range, low-power wireless communication for remote water monitoring, providing a basis for deploying sensor networks in locations where conventional wired communication is difficult.

Pokharel et al. (2024) evaluated LoRa technology for rural connectivity in Nepal through experimental analysis. Their study is particularly relevant to mountainous and geographically challenging environments, where communication performance can be affected by terrain and distance. Parameters such as received signal strength indicator (RSSI), signal-to-noise ratio (SNR), and packet loss are useful for evaluating the reliability of LoRa links under such conditions.

Shrestha et al. (2026) developed a real-time river water-level monitoring and flood-alert system using ESP32 and LoRa technology. Their work demonstrates the relevance of integrating embedded controllers, water-level sensors, and long-range wireless communication for remote hydrological monitoring and timely alerts. Similar principles can be applied to reservoir-level monitoring in hydropower facilities.

Fathoni et al. (2020) investigated a LoRaWAN-based monitoring system for water quality at Tunghai Lake. This study provides a reference for applying low-power wide-area networking to environmental monitoring. LoRaWAN-based approaches are relevant to distributed sensing applications where data from remote monitoring points must be collected and made accessible for further analysis.

Rahimi Azghadi et al. (2024) examined an energy-efficient LoRa-based IoT system for water monitoring, discussing lessons learned and application use cases. Energy efficiency is an important consideration for remote monitoring installations, particularly where sensors and

communication equipment operate in locations with limited access to electrical infrastructure. Their work supports the consideration of power consumption alongside communication reliability in the design of remote sensing systems.

Haniz et al. (2022) proposed a hybrid SUN–LoRa network for remote water-quality monitoring which explored combining communication technologies with a low-altitude platform to support remote connectivity. Such hybrid architectures provide an alternative to relying on a single communication link and are relevant to monitoring applications in geographically challenging areas where direct communication may be constrained.

Materials and Methods

A. System Architecture and Design

The prototype developed in this paper uses a transmitter and receiver node.

The transmitter node uses a ESP-32 microcontroller which receives the data from various environmental sensors and creates packets to be transmitted using the SX1262 LoRa module that uses 868 MHz frequency band which is an unlicensed frequency band in Nepal used for IoT cellular application. The node also consists of environmental sensors which includes the rotary encoder to study the gate position, float switch and ultrasonic sensor used for water level indication and rain sensor to indicate the rainfall in the area.

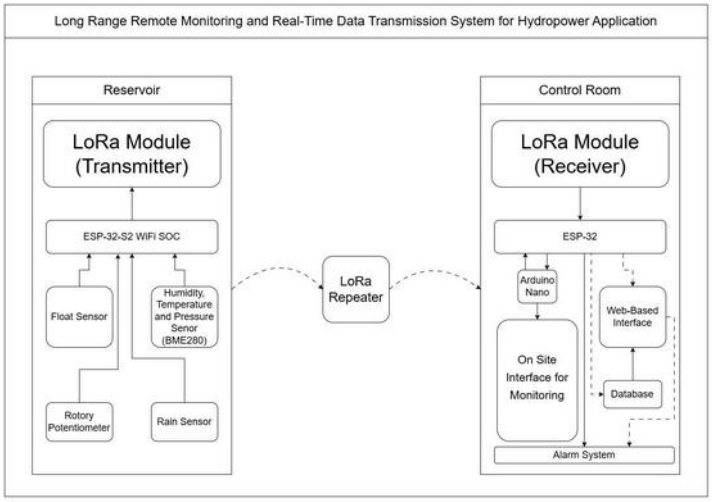


Figure 1: Block diagram of LoRa remote monitoring and real time data transmission system

The receiver node consist of SX1262 LoRa module as receiver, ESP-32 microcontroller which is used to receive the data and send it to the monitor interface, Arduino nano that communicated with ESP-32 using UART communication and sends data to an OLED screen to monitor the received data. The ESP-32 also sends data to a remote monitoring interface and stores data in the developed database structure.

For Longer communication in Hilly areas. LoRa repeater must be used.

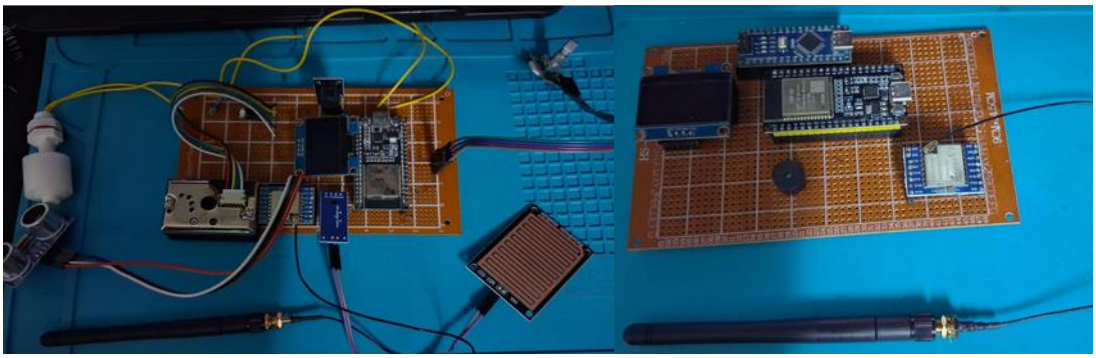


Figure 2: Hardware implementation of transmitter and receiver node

The designed data flow structure includes the storage of all the environmental sensors and communication of data to the web based interface.

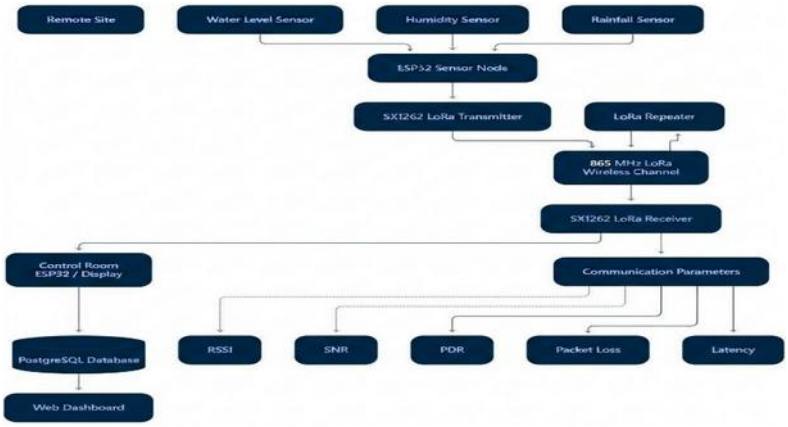


Figure 3: Data Storage Scheme for Database Design

B. **Performance Metrics**

Sensor data was transmitted over a LoRa link between the transmitter and receiver node. The link was tested at multiple distances and at different spreading factors. The various communication parameters were tested. All the performance metrics were taken using ESP-32 libraries.

Packet Delivery Ratio (%) : Represents the share of transmitted packets successfully

Signal to Noise Ratio (dB) : Represents the signal quality relative to background noise

Received Signal Strength Indicator (RSSI): Characterizes the signal strength

Latency (ms): Represents the delay in transmission

C. **Test Distance and Communication**

The distance based measurement were reported in different locations in July of 2025 AD. The reported RSSI, SNR, PDR, Latency and Packet Loss were taken at distance span of 0.5 to 3.10 km and the spreading factor data were taken in span of 0.20 to 1.30km, The measured data were not entirely under line of sight conditions.

D. Analysis Procedure and Regulatory Considerations

The recorded data readings were compared with the distance to identify the variation with relation to parameter metrics. The frequency 865-868 MHz is listed as frequency for unsilenced applications on non-executive and non-protective basis and indicates no frequency fee according to Nepal Telecommunication Authority (NTA), Radio Frequency Policy 2080 (First Amendment). The numerical transmit power limit is also not specified for this frequency band.

Results

The following results were taken using the prototype.

A. Distance Based Data Reading and Link Performance

Table 1 presents the readings of performance metrics from 0.52 to 3.10 km.

Distance (km)	RSSI (dBm)	SNR (dB)	PDR (%)	Packet loss (%)	Latency (ms)
0.52	−74	9.7	98	2	84
0.91	−76	8.3	97	3	91
1.28	−80	6.4	96	4	95
1.74	−84	4.8	94	6	101
2.08	−89	3.6	92	8	104
2.32	−93	2.9	90	10	107
2.93	−94	2.4	89	11	110
3.10	−97	1.5	86	14	114

Table 1. Reported LoRa link performance as a function of distance.

Across the distance range, RSSI decreased from −74 dBm at 0.52 km to −97 dBm at 3.10 km, while SNR decreased from 9.7 dB to 1.5 dB. PDR declined from 98% to 86%, and packet loss increased from 2% to 14%. Reported latency increased from 84 ms to 114 ms. The final reported observation is at 3.10 km.

B. Spreading Factor Comparison : Packet Delivery Ratio

Table 2 compares PDR at SF7, SF9, and SF11 over approximately 0.20–1.30 km.

Distance (km)	SF7 PDR (%)	SF9 PDR (%)	SF11 PDR (%)
0.20	99	99	100
0.35	98	99	99
0.50	97	98	99
0.65	96	98	99
0.80	94	97	98
0.95	91	96	98
1.10	88	94	97
1.30	84	92	96

Table 2. Reported packet delivery ratio for different spreading factors.

PDR decreased with increasing distance for all three spreading factors. At 1.30 km, the reported PDR was 84% for SF7, 92% for SF9, and 96% for SF11. The higher spreading factors therefore maintained better packet delivery in this test.

C. Spreading Factor Comparison : Latency

Table 3 presents the latency measurements reported for the same spreading-factor test.

Distance (km)	SF7 latency (ms)	SF9 latency (ms)	SF11 latency (ms)
0.20	86	95	118
0.35	89	98	123
0.50	94	96	121
0.65	92	103	128
0.80	101	106	134
0.95	98	104	131
1.10	108	112	140
1.30	115	118	147

Table 3. Reported latency for different spreading factors.

Latency generally increased with distance, although small variations appeared in the SF7 and SF11 readings. At 1.30 km, latency was 115 ms for SF7, 118 ms for SF9, and 147 ms for SF11.

Discussion

The distance based measurements show a consistent lowering in link quality as the transmitter–receiver separation increases. The received signal becomes weaker, SNR decreases, PDR falls, packet loss rises, and latency increases. This is important for reservoir monitoring as delayed packets can reduce the timeliness and completeness of the information available to operators. In the test, the link has delivered 86% of packets at 3.10 km but a packet loss of 14% may be insufficient for sensitive application.

The spreading factor (SF) measurements show that SF9 and SF11 achieved higher PDR than SF7 at longer tested distances. At 1.30 km, the difference between SF7 and SF11 was 12 percentage points in PDR. However, SF11 also had the highest latency, reaching 147 ms at 1.30 km compared with 115 ms for SF7.

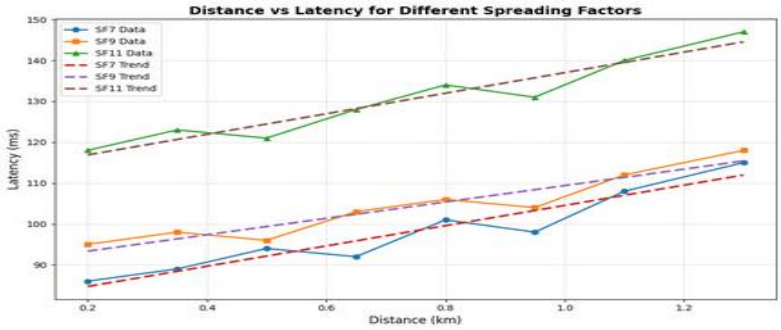


Figure 4. Distance vs Latency for Different Spreading Factors

The choice of spreading factor should therefore depend on the application’s acceptable balance between packet delivery and delay.

Some environmental monitoring may tolerate some additional delay in exchange for improved packet reception, while time-sensitive alarms may require careful end-to-end testing.

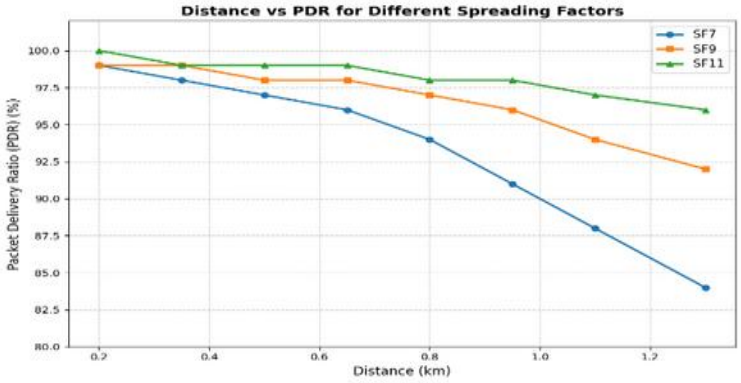


Figure 5. Distance vs PDR for Different Spreading Factors

The prototype architecture combines sensing, wireless transmission, reception, data storage, and a web interface. The environmental and communication parameters read were stored in a PostgreSQL database and displayed through a web dashboard.

For field use, a repeater or elevated relay should be evaluated at sites where terrain blocks a direct link. Further tests should also examine antenna height and orientation, weather and seasonal effects, power use, message retransmission, and failure recovery. Frequency and equipment compliance should be verified with the current official NTA requirements before deployment in real life applications.

Limitations

- The measurements were taken at specific locations around Kathmandu University; they do not establish performance across all hydropower sites or terrain types in Nepal.
- The line of site requirement may not be practical in hilly terrain of Nepal.
- The deployment of the LoRa module of other frequencies such as 433 MHz and so do require permission according to the NTA policy for commercial use.
- The electronic module may not be durable in the challenging environmental condition in Nepal.
- Power supply to the sensors and electronic modules in major challenge in remote areas.

Conclusion

The study presented a prototype for long-range remote monitoring and real time monitoring intended for hydropower application. The results indicate that LoRa is a promising option for remote monitoring, while the communication settings should be selected according to the sensitivity, reliability and acceptable delay.

Before the deployment, the type of LoRa module, operating frequency, NTA regulations, placement and energy consumption should be evaluated alongside the performance communication metrics and properly tested for validation of sensing, storage and alarm conditions.

Funding

The author(s) received no financial support for research, authorship or publication of this paper.

Conflict of Interest

The author(s) declare no conflict of interest.

Data Availability

All data supporting the findings of this study are included in the paper. The source code, hardware configuration details or any required support may also be requested from corresponding author, subject to availability.

References

Fathoni, H., Miao, H.-Y., Chen, C.-Y., & Yang, C.-T. (2020). A monitoring system of water quality Tunghai Lake using LoRaWAN. In Proceedings of the 2020 International Conference on Pervasive Artificial Intelligence (ICPAI) (pp. 281–283). https://doi.org/10.1109/ICPAI51961.2020.00060

Haniz, A., Matsumura, T., Alobaidy, H. A. H., Behjati, M., Nordin, R., Abdullah, N. F., Mandeep, J. S., & Ramli, N. B. (2022). Hybrid SUN-LoRa network on a low altitude platform for remote water quality monitoring. In Proceedings of the 2022 25th International Symposium on Wireless Personal Multimedia Communications (WPMC). https://doi.org/10.1109/WPMC55625.2022.10014878

Pandey, R., Sharma, N. K., & Saharia, M. (2023). LoRa-based communication system for monitoring water quality of lakes and reservoirs. In Proceedings of the 2023 International Conference on Machine Intelligence, GeoAnalytics and Remote Sensing (MIGARS) (Vol. 1, pp. 1–4). https://doi.org/10.1109/MIGARS57353.2023.10064590

Pokharel, A., Sapkota, P., Sapkota, D., Dahal, S., Karki, S., & Budhathoki, R. K. (2024). Performance evaluation of LoRa technology for rural connectivity: An experimental analysis in Nepal. arXiv preprint arXiv:2412.04563.

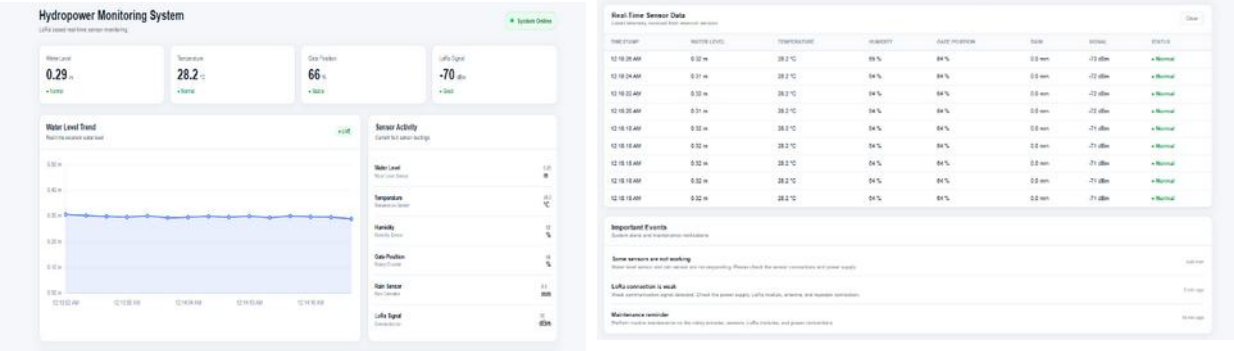
Rahimi Azghadi, S. A., Aghajamali, K., Wachowicz, M., Palma, F., Church, I., & Cao, H. (2024). An energy-efficient LoRa IoT system for water monitoring: Lessons learned and use cases. In Proceedings of the 2024 IEEE International Conference on Consumer Electronics–Asia (ICCE-Asia) (pp. 1–4). https://doi.org/10.1109/ICCE-Asia63397.2024.10773992

Shrestha, R., Rajkarnikar, S., Gautam, S., & Shrestha, S. (2026). Real-time river water level monitoring and flood alert system using ESP32 and LoRa technology. International Journal of Research Publication, 190(1), 66–79. https://doi.org/10.47119/IJRP1001901220268644

Nepal Telecommunications Authority. (2026). Radio frequency (allocation and pricing) for telecommunication service policy, 2023 (First Amendment, April 6, 2026). https://www.nta.gov.np/uploads/contents/Radio-Frequency-Policy-2080-First-Amendment-Translated.pdf

Appendix A

I. Web-Interface



II. Database Interface

	environ [PK] big	node_id integer	recorded_a timestamp	water_level numeric (10,2)	humidity numeric (6,2)	rainfall numeric (10,2)	temperature numeric (6,2)	flow_rate numeric (10,2)	pressure numeric (10,2)
1	1	1	2026-1…	82.40	91.00	25.30	18.70	39.60	836.00

	communi [PK] bigint	node_id integer	measured_at timestamp without	distance numeric	rssi_dbr numeric	snr_db numeric	packets_s integer	packets_re integer	pdr_percen numeric (6,	packet_loss_perc numeric (6,2)
1	3	1	[null]	0.500	-74.00	9.80	100	98	98.00	2.00
2	10	1	[null]	0.520	-74.00	9.70	0	0	98.00	2.00
3	9	1	[null]	0.910	-76.00	8.30	0	0	97.00	3.00
4	7	1	[null]	1.280	-80.00	6.40	0	0	96.00	4.00
5	6	1	[null]	1.300	-79.00	6.10	100	96	96.00	4.00
6	8	1	[null]	1.740	-84.00	4.80	0	0	94.00	6.00
7	5	1	[null]	2.000	-89.00	3.50	100	91	91.00	9.00

Sequential Monte Carlo Based Reliability Analysis of Converter-Dominated Power Systems

Ghanendra Rajbanshi[1*], Sujan Adhikari[2]

[1,2]Department of Electrical Engineering, Pulchowk Campus, Institute of Engineering, Tribhuvan University
Lalitpur, Nepal
*080mspse010.ghanendra@pcampus.edu.np
sujan.adhikari@pcampus.edu.np

Abstract

The growing use of photovoltaic (PV) and wind generation in modern power systems has increased dependence on power electronic converters. As these converters age, the reliability of their internal components may decrease, reducing renewable-generation availability and affecting overall system adequacy. This study develops a component-to-system reliability framework to evaluate this effect. Representative 500 kW PV and wind-turbine converters are assessed using one-year mission profiles from Jumla and Kagbeni, Nepal. Electrical and thermal stresses of insulated-gate bipolar transistors (IGBTs) and DC-link capacitors are evaluated to estimate accumulated damage and component lifetime. Monte Carlo simulation and two-parameter Weibull fitting are used to determine age-dependent component reliability, converter availability, and expected energy not produced (EENP). The resulting reliability characteristics are incorporated into 400 MW of renewable generation integrated into a modified IEEE Reliability Test System-24 (IEEE RTS-24). Three cases are investigated: the original conventional system, renewable integration with constant converter availability, and renewable integration with age-dependent converter wear-out. Sequential Monte Carlo simulation is then used for system-level adequacy assessment. Compared with the constant-availability case, loss of load expectation (LOLE) increases from 78.52 to 80.95 h/year, while expected energy not supplied (EENS) increases from 12,445 to 12,831.1 MWh/year, corresponding to increases of 3.09% and 3.10%, respectively. The results demonstrate that age-dependent wear-out of IGBTs and DC-link capacitors should be considered in the adequacy assessment of converter-dominated power systems.

Keywords: age-dependent reliability, DC-link capacitor, IGBT, sequential Monte Carlo simulation, system adequacy

Introduction

Wind and photovoltaic (PV) generation reach the grid through power electronic converters, so the effective availability of renewable generation depends on converter reliability as well as on the weather (Peyghami et al., 2021; Zhang et al., 2021). A converter failure disconnects a generating unit even when the resource is available, so treating converters as perfectly reliable, or by a fixed availability, can overstate the contribution of renewables to adequacy.

Converter failures arise from random-chance events and from progressive wear-out. Insulated-gate bipolar transistor (IGBT) modules and DC-link capacitors are the most ageing-sensitive components: IGBTs suffer thermo-mechanical fatigue under junction-temperature cycling (Bayerer et al., 2008; Wang et al., 2013), whereas capacitor life depends on hotspot temperature, ripple current and voltage (Wang & Blaabjerg, 2014). Because loading follows the solar or wind

resource, mission-profile-based assessment (environment → electrical and thermal stress → damage → lifetime) quantifies wear-out (Peyghami et al., 2020; Zhou et al., 2019), and chronological failures, repairs, load and renewable output call for sequential Monte Carlo simulation (SMCS) (Billinton & Allan, 1996; Huang et al., 2025).

The chain from mission profile through component ageing to chronological adequacy is seldom treated for PV and wind together. This paper contributes (i) mission-profile-based lifetime and Weibull models of IGBTs and DC-link capacitors for a 500 kW PV inverter (Jumla) and a 500 kW wind converter (Kagbeni); (ii) a semi-Markov model that combines wear-out with random-chance failures into age-dependent availability and expected energy not produced (EENP); and (iii) an SMCS of a modified IEEE RTS-24 system quantifying the effect of converter ageing on loss of load expectation (LOLE) and expected energy not supplied (EENS).

Literature Review / Related Work

Zhang et al. (2021) proposed a hierarchical framework linking device- and converter-level reliability with power-system reliability and evaluated a converter-integrated RTS-24 system with non-sequential Monte Carlo sampling. Peyghami et al. (2021) developed a device-to-system approach that treats random-chance and wear-out failures of converters separately. Both works show that representing converters by a fixed availability gives an incomplete picture of renewable-generation availability.

Random-chance failures are conventionally modelled with a constant failure rate and an exponential distribution, whereas wear-out failures depend on accumulated stress and age and follow the rising part of the bathtub curve (Peyghami et al., 2021). Physics-of-failure methods capture wear-out by passing the mission profile through electrical and thermal models to damage and lifetime (Peyghami et al., 2020). For IGBTs, power-cycling tests show that lifetime falls with the junction-temperature swing and rises with lower mean temperature (Bayerer et al., 2008); a modified Coffin–Manson–Arrhenius model with Miner’s rule has been applied to PV inverters under different power-tracking strategies (Batunlu et al., 2016). For DC-link capacitors, lifetime depends on hotspot temperature and voltage (Wang & Blaabjerg, 2014), and mission-profile-based evaluation of capacitor banks in wind converters shows that varying operating conditions change lifetime consumption (Zhou et al., 2019).

Parameter uncertainty is commonly propagated by Monte Carlo sampling, and the resulting lifetime population is described by a Weibull distribution whose shape parameter indicates the wear-out behaviour (Peyghami et al., 2020). Availability additionally requires repair data; field studies of wind-turbine converters report failure rates and repair times (Carroll et al., 2016). At system level, LOLE and EENS are standard adequacy indices (Billinton & Allan, 1996), and SMCS preserves the chronology of failures, repairs, load and renewable output; Huang et al. (2025) applied it with both ageing and random failure modes. The IEEE Reliability Test System remains the usual benchmark (Grigg et al., 1999).

The reviewed studies treat converter reliability at device or system level, use constant failure rates or non-sequential sampling, or do not cover PV and wind converters together. The present work combines mission-profile lifetime modelling, semi-Markov availability and chronological SMCS for both technologies.

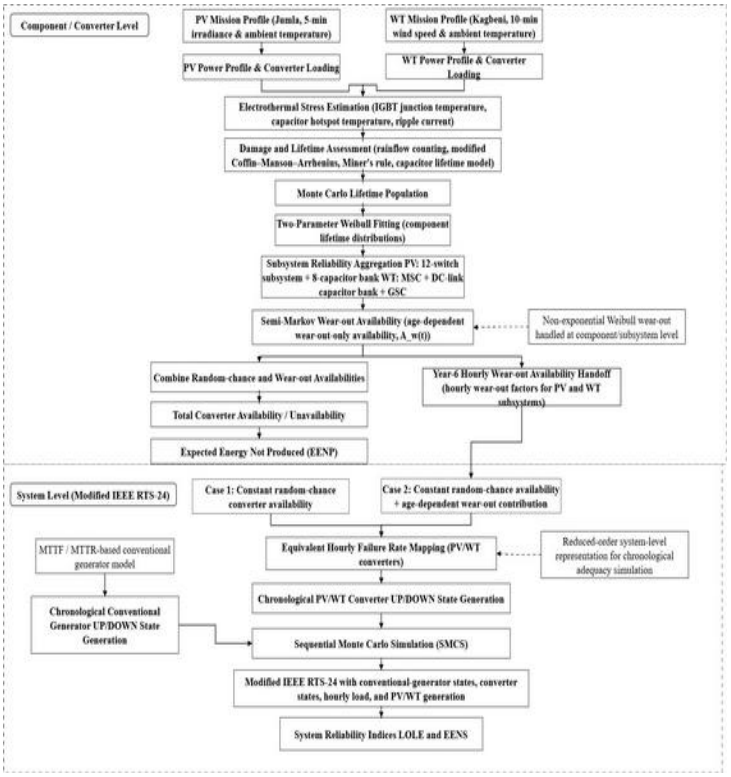
Materials and Methods

Overall Framework

The study follows the chain mission profile → electrical stress → thermal stress → damage → lifetime → converter availability → system adequacy, as shown in Figure 1. IGBTs and DC-link capacitors of a 500 kW PV inverter and a 500 kW wind-turbine converter are modelled for wear-out (Peyghami et al., 2021); all other converter components use constant random-chance failure and repair rates. The resulting availabilities enter an SMCS of a modified IEEE RTS-24 system. All component-level reliability calculations, Monte Carlo lifetime simulations, Weibull fitting, semi-Markov availability modelling, and system-level sequential Monte Carlo simulations were implemented in MATLAB.

Figure 1

Component-to-system reliability assessment framework



Mission Profiles and Converter Models

The PV model uses one year of 5-minute global horizontal irradiance (G) and ambient temperature (T_a) measured at Jumla (World Bank Group, 2018). The array has 912 CS6W-550MS modules (501.6 kWp; Canadian Solar Inc., n.d.) and its output follows Eq. (1), with γ_P = −0.0034 °C^{-1}, nominal operating cell temperature (NOCT) of 41 °C, G_{STC} = 1,000 W/m² and T_{STC} = 25 °C at standard test conditions (STC), and maximum power point tracking (MPPT) and DC-side efficiencies of 0.985 each. The inverter is a two-level three-phase converter (unity power factor; Jia et al., 2020; Liu & Molinas, 2021) with twelve IGBT positions (two parallel Infineon FF650R17IE4P [Infineon Technologies AG, n.d.] half-bridge modules per phase leg) and eight parallel film capacitors on the DC link.

(1)

The wind model uses one year of 10-minute wind speed at 80 m for Kagbeni (World Bank Group, 2019) and ERA5-Land temperature (Copernicus Climate Change Service, 2025). The EWT DW52-500 turbine (500 kW; cut-in, rated and cut-out speeds 2.5, 10 and 25 m/s; EWT, 2018) follows the cubic power curve of Eq. (2). Its full-scale back-to-back converter has a machine-side converter (MSC), a three-capacitor DC link and a grid-side converter (GSC), each with six IGBT positions (power factor 0.95). Table 1 summarises the inputs.

(2)

Table 1

Main Converter Modelling Parameters

Parameter	PV converter	Wind converter
Mission profile	Jumla, 5 min, 105,120 samples	Kagbeni, 10 min, 52,560 samples
Rating	501.6 kWp array; 500 kW inverter	EWT DW52-500, 500 kW
AC / DC-link voltage; switching	315 V / 800 V; 2.5 kHz	690 V / 1,200 V; 3 kHz
IGBT module	FF650R17IE4P (1,700 V, 650 A), 12 positions	FF650R17IE4P, 6 per MSC/GSC stage
DC-link capacitors	8 × 1,100 µF, 1,100 V, KEMET C44U (KEMET/YAGEO, n.d.)	3 × 1.5 mF, 1,500 V, TDK B25680 (TDK Electronics, n.d.)
Capacitor life model	L_B = 60,000 h at 85 °C, ΔT = 10 °C, n_V = 8	L_B = 100,000 h at 70 °C, ΔT = 10 °C, n_V = 5
Random-chance λ_c / μ (year^{-1})	Switch 0.15/150; capacitor 0.20/150; other 0.15/185	MSC and GSC 0.15/150 each; capacitor 0.20/150; other 0.15/185
Lifetime Monte Carlo samples	5,000	5,000

Note. Random-chance rates follow Peyghami et al. (2021). Capacitor parameters n_V are selected modelling values.

Electrothermal Stress and Lifetime Models

IGBT average and root-mean-square (RMS) currents follow from the converter current and a sinusoidal pulse-width modulation (PWM) relation, and loss is given by Eq. (3) with V_{CE0} = 0.95 V, r_{CE} = 2.25 mΩ and datasheet switching energy scaled with current and voltage. For PV, a four-term Foster network, Eq. (4) with $a_i = \exp(-\Delta t/\tau_i)$, converts loss into junction temperature T_j, with heatsink temperature approximated by ambient temperature; the wind converter uses a steady-state thermal resistance because of the 10-minute sampling.

(3)

(4)

Rainflow counting of $T_j(t)$ yields cycle ranges $\Delta T_{j,i}$, mean temperatures $T_{j,m,i}$ (K) and counts n_i; cycles to failure follow the modified Coffin–Manson–Arrhenius model (Batunlu et al., 2016), Eq. (5), with A = 610, α = −5 (here α is the Coffin–Manson exponent, not the Weibull scale), $E_a = 1.3 \times 10^{-19}$ J and Boltzmann constant k_B; annual damage and lifetime follow Miner's rule, Eq. (6). Lifetime L is in years of repeated annual loading.

(5)

(6)

Capacitor ripple current follows the analytical PWM relation of Kolar and Round (2006) for PV and a PWM-state lookup, combined root-sum-square over MSC and GSC, for wind. With N_C parallel cans, equivalent series resistance (ESR) loss and core temperature follow Eq. (7), and lifetime follows the temperature- and voltage-stress law of Eq. (8) (Wang & Blaabjerg, 2014), with parameters in Table 1 and V_{op}/V_{rated} = 800/1,100 V (PV) or 1,200/1,500 V (wind). Annual damage and lifetime follow Eq. (9).

(7)

(8)

(9)

Monte Carlo Lifetime Simulation and Weibull Fitting

Parameter uncertainty is represented by 5,000 Monte Carlo realisations of the thermal-resistance, loss, lifetime-model, ESR and ripple-current parameters (lognormal, except a normal Coffin–Manson exponent), giving lifetime populations for one representative IGBT position (separately for MSC and GSC in the wind converter) and one capacitor can. Two-parameter Weibull distributions, Eq. (10), are fitted by median-rank regression (Peyghami et al., 2020), where α is the scale and β the shape parameter. For N identical, independent devices that are all required (12 IGBTs and 8 capacitors for PV; 6 IGBTs per stage and 3 capacitors for wind), subsystem parameters follow Eq. (11).

(10)

(11)

Converter Availability and Expected Energy Not Produced

Random-chance failures use constant failure rates $\lambda_{c,i}$ and repair rates μ_i (Table 1), giving $A_{c,i} = \mu_i/(\lambda_{c,i} + \mu_i)$ for each subsystem. Because Weibull wear-out times are non-exponential, the repairable wear-out availability is obtained from a two-state semi-Markov alternating-renewal process, Eq. (12): up-time follows the subsystem Weibull law with survival function $R_{w,i}$ and density $f_{w,i}$, repair time is exponential with density g_i, and the subsystem is as good as new after repair. Equation (12) is solved on a daily age grid over ten years. Assuming independent mechanisms, subsystem availability is $A_i(t) = A_{c,i}A_{w,i}(t)$, and the series-critical blocks (switching subsystem SW or MSC/GSC, capacitor bank Cap, other components OC) give the converter availability in Eq. (13), with unavailability $U = 1 - A$. The no-age reference retains only A_c. Expected energy not produced in operating year y is Eq. (14), where P_{conv} is converter power and $t_{y,k}$ the operating age of sample k; the annual profile is repeated, so changes in EENP reflect ageing only.

(12)

(13)

(14)

System-Level Sequential Monte Carlo Simulation

Adequacy is assessed on the IEEE RTS-24 system (Grigg et al., 1999), expanded to 32 conventional units (3,405 MW) with RTS-96 failure and repair data and the 52-week, 8,736-hour RTS-96 hourly load profile. PV (690 units, 345 MW) and wind (110 units, 55 MW), each unit

rated 0.5 MW with its own converter, are connected at buses 2, 7, 13, 15 (PV) and 13, 18, 22 (wind), and conventional capacity is displaced at the same buses on a 1:1 nameplate basis. Three cases are simulated: Case 0, the original system; Case 1, the renewable-integrated system with constant random-chance converter availability; and Case 2, the same system with hourly wear-out availabilities from the semi-Markov models for the sixth operating year (age 5–6 years) multiplied by the random-chance availability.

Figure 2 shows the test system before and after renewable integration. The original IEEE RTS-24 system (Figure 2a), used in Case 0, has 24 buses at 138 kV and 230 kV, conventional generating units at buses 1, 2, 7, 13, 15, 16, 18, 21, 22 and 23, and 17 load buses. In the modified system (Figure 2b), used in Cases 1 and 2, PV units are connected at buses 2, 7, 13 and 15 and wind turbines at buses 13, 18 and 22, each through its own power converter, and the conventional capacity at these buses is reduced by the installed renewable capacity; the network topology and loads are unchanged. Cases 1 and 2 therefore use the same modified system and differ only in the converter availability model: constant random-chance availability in Case 1 and age-dependent availability at operating ages of 5–6 years in Case 2.

Each converter is a two-state UP/DOWN unit, and its target availability $A(t)$ is converted into an hourly failure intensity by Eq. (15), with a converter mean time to repair $MTTR_{conv}$ = 12 h derived from Carroll et al. (2016) and applied to PV by assumption. A DOWN converter delivers no output until repaired, and conventional units use exponential up and down times. Renewable output is dispatched first, a DC load flow with approximate branch losses gives the net supply, and the hourly deficit $P_{def}(t)$ defines LOLE and EENS in Eqs. (16) and (17), averaged over N_{MC} = 5,000 trials of 8,736 h each (Billinton & Allan, 1996; Huang et al., 2025). In Eq. (16), the indicator function equals 1 when a deficit occurs and 0 otherwise. Cases 1 and 2 share common random numbers to reduce sampling variability in their comparison.

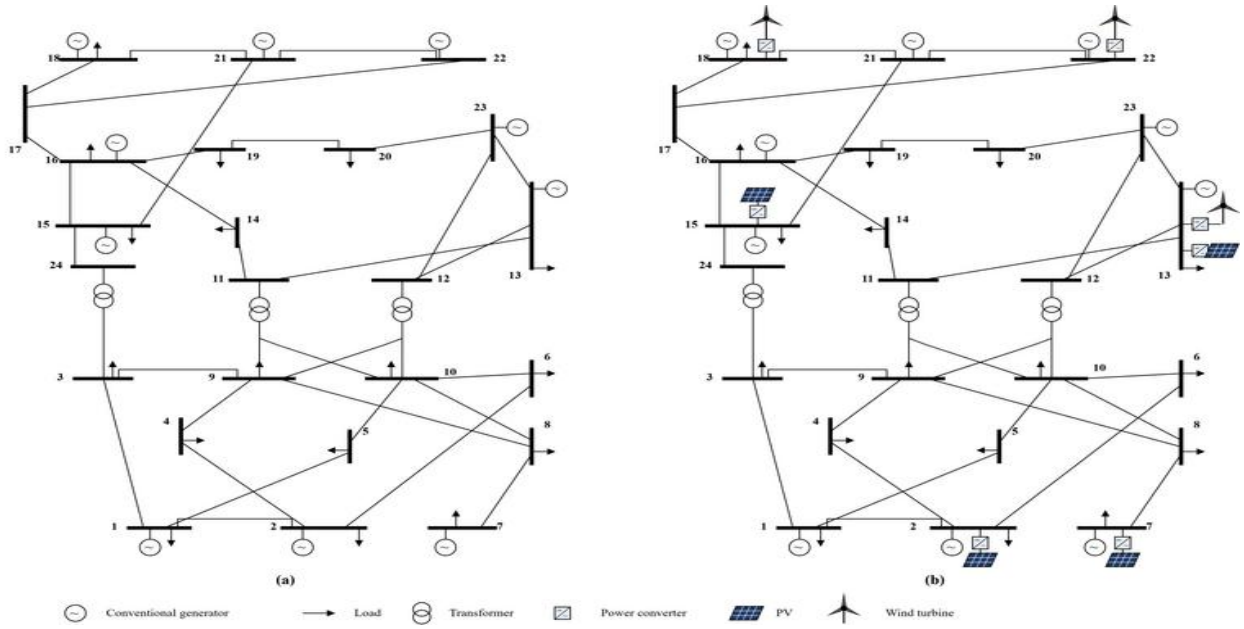
(15)

(16)

(17)

Figure 2

IEEE RTS-24 system: (a) original conventional system (Case 0); (b) modified system with PV and wind generation connected through power converters (Cases 1 and 2)



Note. Network topology based on the IEEE Reliability Test System (Grigg et al., 1999); renewable-generation placement and converter interfaces from the present study.

Results

Mission Profiles and Electrothermal Stress

The Jumla profile has a mean irradiance of 218.3 W/m² (maximum 1,398 W/m²) and a mean temperature of 11.6 °C, giving a mean inverter output of 100.6 kW and 881.0 MWh/year of PV energy. The Kagbeni profile has a mean wind speed of 6.64 m/s (maximum 23.0 m/s) and mean temperature of 9.6 °C, giving a mean turbine output of 180.8 kW and 1,584.1 MWh/year. Table 2 summarises the stresses. Absolute temperatures stay moderate, so ageing is driven by thermal cycling rather than overheating. The mean rainflow swing is about four times larger for the wind converter (11.1 °C) than for the PV inverter (2.8 °C), because irregular wind power cycles the devices more severely than the regular diurnal solar cycle.

Table 2

Mission-Profile and Electrothermal Stress Results

Quantity	PV converter	Wind converter
Mean converter output power (kW)	100.6	180.8
Annual energy (MWh/year)	881.0	1,584.1
Mean AC line current (A)	184.3	159.3
Mean / maximum IGBT T_j (°C)	19.1 / 67.7	30.6 / 79.2
Mean rainflow ΔT_j (°C)	2.80	11.13
Mean / maximum capacitor hotspot (°C)	13.6 / 43.1	14.5 / 35.5

Note. Wind-converter values apply to both the MSC and GSC, which are loaded identically in the reduced-order model.

Lifetime and Weibull Analysis

All fitted shape parameters exceed unity (Table 3), confirming an increasing wear-out hazard with age. For PV, the IGBT has the smaller scale parameter (17.67 years against 18.67 years for

the capacitor), whereas the capacitor has the steeper hazard (β = 3.92). For wind, the MSC and GSC IGBTs (α = 15.16 and 15.47 years; mean Monte Carlo lifetimes 13.6 and 13.9 years) reach their characteristic life well before the capacitor (α = 22.60 years; mean 20.5 years), so the IGBT stages limit the wind converter. Aggregation by Eq. (11) moves subsystem characteristic lives far earlier, to about 7.9 years for the PV switching stage and 8.1 years for each wind stage, which explains the decline in availability within a decade.

Table 3

Fitted Weibull Parameters of Representative Components and Equivalent Subsystems

Component	α (years)	β	Subsystem α (years)
PV IGBT (12 positions)	17.666	3.069	7.86
PV DC-link capacitor (8 cans)	18.672	3.920	10.98
Wind MSC IGBT (6 positions)	15.158	2.843	8.07
Wind GSC IGBT (6 positions)	15.474	2.782	8.13
Wind DC-link capacitor (3 cans)	22.600	3.818	16.95

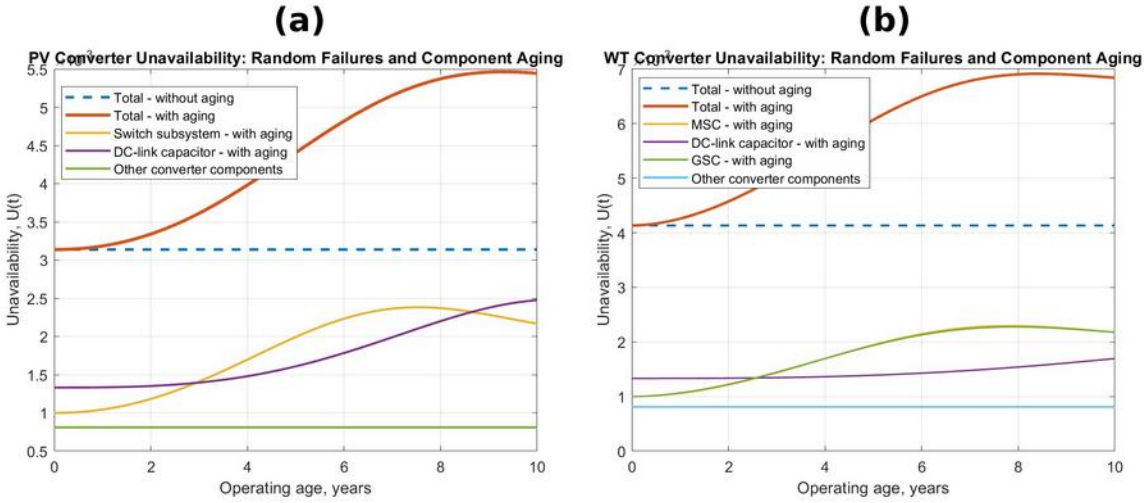
Note. Subsystem α is obtained from Eq. (11) with $\beta_{sub} = \beta$.

Converter Availability and Expected Energy Not Produced

With random-chance failures only, the PV and wind converters have availabilities of 0.996863 and 0.995867 (unavailability 0.003138 and 0.004133). Wear-out has little effect early in life (PV unavailability 0.003184 at the end of the first year), but at an operating age of five years unavailability reaches 0.004405 for PV and 0.006069 for wind, which is 40% and 47% above the random-only values (Figure 3 and Table 4). The MSC and GSC dominate the wind-converter ageing contribution.

Figure 3

Converter unavailability with operating age: (a) PV converter; (b) wind converter



Annual EENP of the PV unit rises from 2.764 MWh/year without ageing to 2.776 MWh/year in Year 1 and 4.062 MWh/year in Year 6, an additional 1.298 MWh/year (0.15% of annual PV energy). For the wind turbine, EENP rises from 6.548 to 6.623 and 9.995 MWh/year, an additional 3.447 MWh/year (0.22% of annual wind energy). The larger wind loss reflects its higher annual energy and shorter equivalent lives (Figure 4).

Table 4

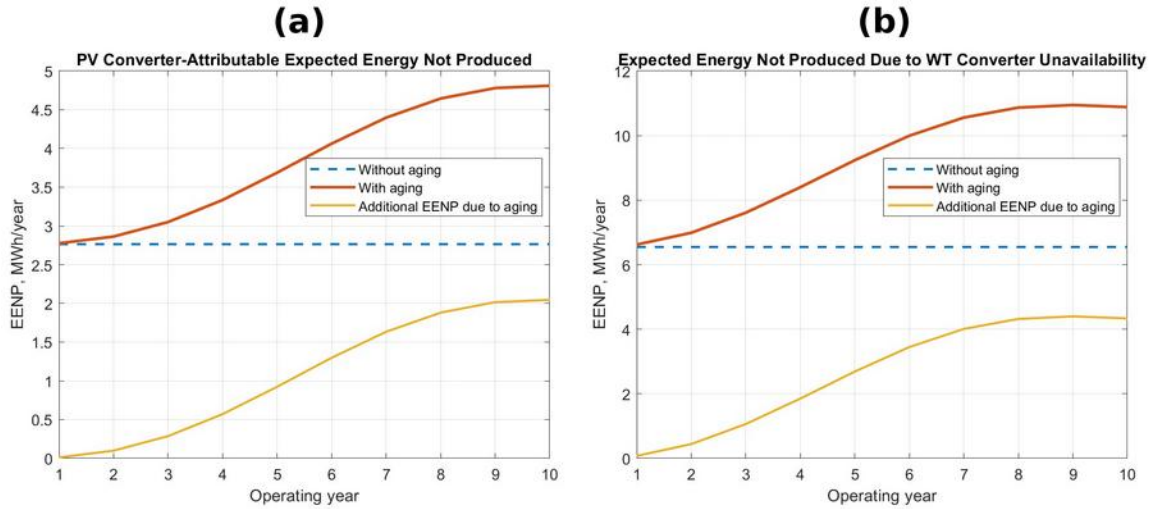
Converter Unavailability and Expected Energy Not Produced

Converter	Condition	Unavailability	EENP (MWh/year)	Additional EENP (MWh/year)
PV	No ageing	0.003138	2.764	–
PV	Year 6 (age 5 years)	0.004405	4.062	1.298
Wind	No ageing	0.004133	6.548	–
Wind	Year 6 (age 5 years)	0.006069	9.995	3.447

Note. EENP is the converter-attributable energy loss of one 500 kW unit; Year 1 values are given in the text.

Figure 4

Converter-attributable EENP with and without ageing: (a) PV unit; (b) wind turbine



System-Level Adequacy

Table 5 and Figure 5 give the SMCS results. The original system (Case 0) has an EENS of 2,170 MWh/year and an LOLE of 15.46 h/year. Renewable integration with baseline converter reliability (Case 1) raises these to 12,445 MWh/year and 78.52 h/year. Adding age-dependent wear-out (Case 2) raises them further to 12,831.1 MWh/year and 80.95 h/year, i.e., by 386.1 MWh/year (3.10%) in EENS and 2.43 h/year (3.09%) in LOLE relative to Case 1. Deficits accumulate mainly in the winter weeks, most steeply near the end of the horizon where the weekly peak load is highest.

Table 5

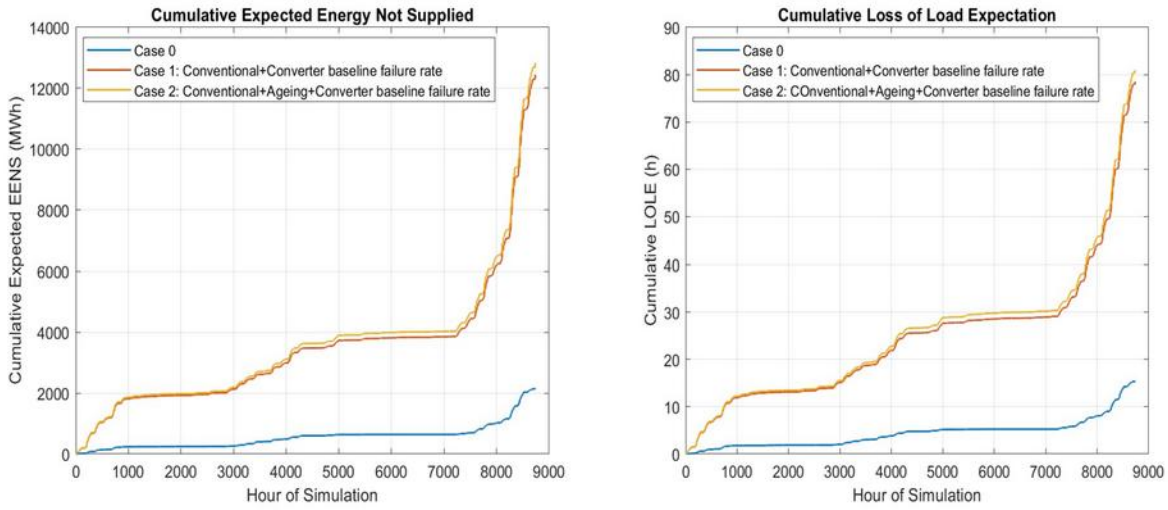
System-Level Adequacy Indices of the Modified IEEE RTS-24 System

Case	EENS (MWh/year)	LOLE (h/year)	ΔEENS vs. Case 1	ΔLOLE vs. Case 1
Case 0: conventional system	2,170	15.46	–	–
Case 1: renewables, constant converter availability	12,445	78.52	–	–
Case 2: renewables, age-dependent converter availability	12,831.1	80.95	+386.1 (+3.10%)	+2.43 (+3.09%)

Note. Means of 5,000 sequential Monte Carlo trials; Case 2 uses converter ages of 5–6 years.

Figure 5

Cumulative mean EENS and LOLE over the simulated year for Cases 0, 1 and 2



Discussion

The component results explain the system outcome. Mission-profile loading produces junction-temperature cycling and capacitor heating, and the resulting lifetime populations have increasing Weibull hazards ($\beta > 1$), so converter unavailability grows with age and more renewable output is lost to converter outages. The wind converter ages faster because its IGBTs experience larger temperature swings, consistent with power-cycling evidence that swing magnitude, not steady temperature, limits IGBT life (Batunlu et al., 2016; Bayerer et al., 2008). In the sequential simulation, outages remove otherwise available generation during high demand, enlarging the size and duration of deficits.

The Case 0–Case 1 comparison mixes the replacement of 400 MW of conventional nameplate capacity by intermittent PV and wind, resource variability and baseline converter unavailability; it does not show that renewable integration inherently reduces reliability, only that this result holds for the capacities, 1:1 substitution and profiles used here. The Case 1–Case 2 comparison is the relevant one for converter ageing, since both cases share the same configuration, profiles and random numbers. Its 3.10% increase in EENS and 3.09% increase in LOLE show that a fixed converter availability underestimates long-term inadequacy, in line with the earlier conclusion that converter reliability affects system reliability (Peyghami et al., 2021; Zhang et al., 2021) and extending it to wear-out with chronological simulation (Huang et al., 2025). At converter level, the effect is delayed, being small in year one and substantial by year six, which suggests that inspection or replacement before the wear-out region could limit the loss. Unit-level EENP should not be equated with system-level EENS, which also depends on the number and location of renewable units and the remaining conventional generation.

Limitations

The models are reduced-order and intended for long-term reliability assessment. Only IGBTs and DC-link capacitors are given a wear-out model, whereas gate drivers, cooling and control circuits are represented by constant rates, and MPPT and switching dynamics are excluded. One measured annual profile per site is repeated, and several parameters (uncertainty factors, voltage exponents, and the MSC voltage) are modelling assumptions. Case 2 is an age-conditioned snapshot at year six rather than a continuous multi-year simulation. The network uses a DC load flow without branch limits or line outages, so the indices describe generation adequacy with approximate losses rather than composite reliability.

Conclusion

A component-to-system framework was developed to quantify how age-dependent wear-out of IGBTs and DC-link capacitors in PV and wind converters affects power-system adequacy. All fitted Weibull shape parameters (2.8–3.9) indicate increasing wear-out, with IGBTs limiting the wind converter. At five years of operation, converter unavailability rises by 40% (PV) and 47% (wind) relative to random failures alone, and the converter-attributable energy loss per unit increases by 1.30 and 3.45 MWh/year. In the modified IEEE RTS-24 system, ageing raises EENS by 3.10% and LOLE by 3.09% compared with constant converter availability. Treating converters with fixed reliability parameters therefore underestimates long-term inadequacy. Future work should include further converter components, AC power flow with line outages, reserves and storage, and an economic assessment of maintenance and replacement.

Funding

The authors received no financial support for the research, authorship, or publication of this paper.

Conflict of Interest

The authors declare no conflict of interest.

Data Availability

The solar mission-profile data are from the World Bank/ESMAP Nepal – *Solar Radiation Measurement Data* (World Bank Group, 2018), while the Kagbeni wind-speed data are from the World Bank/ESMAP Nepal – *Wind Measurement Data* (World Bank Group, 2019). The ambient-temperature data are from ERA5-Land (Copernicus Climate Change Service, 2025), and the reliability test system data are from the IEEE RTS-96 report (Grigg et al., 1999). The simulation codes are available from the authors on reasonable request.

References

Batunlu, C., Alrweq, M., & Albarbar, A. (2016). Effects of power tracking algorithms on lifetime of power electronic devices used in solar systems. *Energies, 9*(11), Article 884. https://doi.org/10.3390/en9110884

Bayerer, R., Herrmann, T., Licht, T., Lutz, J., & Feller, M. (2008). Model for power cycling lifetime of IGBT modules—Various factors influencing lifetime. In *Proceedings of the*

5th International Conference on Integrated Power Systems (CIPS) (pp. 1–6). VDE Verlag.

Billinton, R., & Allan, R. N. (1996). *Reliability evaluation of power systems* (2nd ed.). Plenum Press.

Canadian Solar Inc. (n.d.). *HiKu6 CS6W-MS (CS6W-550MS)* [Photovoltaic module datasheet].

Carroll, J., McDonald, A., & McMillan, D. (2016). Failure rate, repair time and unscheduled O&M cost analysis of offshore wind turbines. *Wind Energy, 19*(6), 1107–1119. https://doi.org/10.1002/we.1887

Copernicus Climate Change Service. (2025). *ERA5-Land hourly time-series data from 1950 to present* [Data set]. Copernicus Climate Data Store. https://doi.org/10.24381/ee82e357

EWT. (2018). *DW52-500 kW direct-drive wind turbine* [Product flyer].

Grigg, C., Wong, P., Albrecht, P., Allan, R., Bhavaraju, M., Billinton, R., Chen, Q., Fong, C., Haddad, S., Kuruganty, S., Li, W., Mukerji, R., Patton, D., Rau, N., Reppen, D., Schneider, A., Shahidehpour, M., & Singh, C. (1999). The IEEE Reliability Test System-1996: A report prepared by the Reliability Test System Task Force of the Application of Probability Methods Subcommittee. *IEEE Transactions on Power Systems, 14*(3), 1010–1020. https://doi.org/10.1109/59.780914

Huang, W., Hu, B., Shao, C., Li, W., Wang, X., Xie, K., & Chung, C. Y. (2025). Power system reliability evaluation based on sequential Monte Carlo simulation considering multiple failure modes of components. *Journal of Modern Power Systems and Clean Energy, 13*(1), 202–214. https://doi.org/10.35833/MPCE.2023.000939

Infineon Technologies AG. (n.d.). *FF650R17IE4P: 1700 V, 650 A PrimePACK 2 half-bridge IGBT module* [Datasheet].

Jia, J., Yan, X., Wang, Y., Aslam, W., & Liu, W. (2020). Parameter identification and modelling of photovoltaic power generation systems based on LVRT tests. *IET Generation, Transmission & Distribution, 14*(15), 3089–3098. https://doi.org/10.1049/iet-gtd.2019.1730

KEMET/YAGEO. (n.d.). *C44U-T metallized polypropylene DC-link capacitors (C44UQGT7110T53K)* [Datasheet].

Kolar, J. W., & Round, S. D. (2006). Analytical calculation of the RMS current stress on the DC-link capacitor of voltage-PWM converter systems. *IEE Proceedings—Electric Power Applications, 153*(4), 535–543. https://doi.org/10.1049/ip-epa:20050458

Liu, J., & Molinas, M. (2021). Impact of digital time delay on the stable grid-hosting capacity of large-scale centralised PV plant. *IET Renewable Power Generation, 15*(7), 1422–1435. https://doi.org/10.1049/rpg2.12097

Peyghami, S., Blaabjerg, F., & Palensky, P. (2021). Incorporating power electronic converters reliability into modern power system reliability analysis. *IEEE Journal of Emerging and Selected Topics in Power Electronics, 9*(2), 1668–1681. https://doi.org/10.1109/JESTPE.2020.2967216

Peyghami, S., Wang, Z., & Blaabjerg, F. (2020). A guideline for reliability prediction in power electronic converters. *IEEE Transactions on Power Electronics, 35*(10), 10958–10968. https://doi.org/10.1109/TPEL.2020.2981933

TDK Electronics. (n.d.). *Film capacitors – Power electronic capacitors – MKP DC B25680 (B25680B1158K503)* [Datasheet].

Wang, H., & Blaabjerg, F. (2014). Reliability of capacitors for DC-link applications in power electronic converters—An overview. *IEEE Transactions on Industry Applications, 50*(5), 3569–3578. https://doi.org/10.1109/TIA.2014.2308357

Wang, H., Liserre, M., & Blaabjerg, F. (2013). Toward reliable power electronics: Challenges, design tools, and opportunities. *IEEE Industrial Electronics Magazine*, *7*(2), 17–26. https://doi.org/10.1109/MIE.2013.2252958

World Bank Group. (2018). *Nepal – Solar radiation measurement data* [Data set]. Energy Sector Management Assistance Program (ESMAP), ENERGYDATA.info. https://energydata.info/dataset/nepal-solar-radiation-measurement-data

World Bank Group. (2019). *Nepal – Wind measurement data* [Data set]. Energy Sector Management Assistance Program (ESMAP), ENERGYDATA.info. https://energydata.info/dataset/nepal-wind-measurement-data

Zhang, B., Wang, M., & Su, W. (2021). Reliability analysis of power systems integrated with high-penetration of power converters. *IEEE Transactions on Power Systems, 36*(3), 1998–2009. https://doi.org/10.1109/TPWRS.2020.3032579

Zhou, D., Song, Y., Liu, Y., & Blaabjerg, F. (2019). Mission profile based reliability evaluation of capacitor banks in wind power converters. *IEEE Transactions on Power Electronics, 34*(5), 4665–4677. https://doi.org/10.1109/TPEL.2018.2865710

Thermal Behaviour of Underground Cable Under the Influence of Harmonics

Krishna Raj Majhi[1], Bishal Silwal[1*]

[1] Department of Electrical Engineering, Pulchowk Campus, Institute of Engineering, Tribhuvan University, Lalitpur, Nepal
080mspse011.krishna@pcampus.edu.np
[*]Corresponding author: bishal.silwal@pcampus.edu.np

Abstract

Non-linear loads have increased harmonic distortion, yet the International Electrotechnical Commission (IEC) standard 60287 still rates underground cables for sinusoidal current, ignoring the heating effect of individual harmonics. Harmonics, soil drying and close cable spacing raise temperatures, accelerating insulation ageing. This study examines a 300 mm² three-core aluminium, cross-linked polyethylene (XLPE)-insulated 11 kV cable buried 1 m deep with a 45 °C ground surface temperature, using a two-dimensional coupled electromagnetic–thermal finite element method (FEM) model in COMSOL Multiphysics. Six harmonic orders (h = 1, 3, 5, 7, 11, 13; total harmonic distortion (THD) = 40.5%) were solved individually and superimposed. The third harmonic, injected by non-linear loads through star-earthed (YNyn) transformers, returns via the cable screens, armour and earth. At the rated current of 304 A peak (215 A root-mean-square, RMS), the third harmonic, despite carrying only 30% of this current, raised the conductor temperature by 64.1 °C, 1.4 times the fundamental's contribution, because its zero-sequence fields reinforce rather than cancel in the metallic screens and armour. The hot-spot temperature reached 162 °C, requiring derating to 198 A peak (140 A RMS) to maintain the 90 °C limit. Reducing soil thermal conductivity from 0.35 to 0.30 W/(m·K) added 8 °C, and the trefoil formation ran 3.8 °C hotter than the flat formation. Even 10% THD added 4 °C, reducing insulation life by 27% according to an Arrhenius assessment. Sinusoidal ratings therefore overestimate ampacity; safe rating must jointly consider harmonics, formation and soil conditions.

Keywords: Underground cable, Harmonics, Cross-linked polyethylene (XLPE) insulation, Finite element method, Ampacity derating

Introduction

Underground cross-linked polyethylene (XLPE) cables are the backbone of urban medium-voltage (MV) distribution, and their current rating (ampacity) is limited by a maximum continuous conductor temperature of 90 °C (International Electrotechnical Commission [IEC], 2014b). Ratings are normally calculated with IEC 60287 (IEC, 2014a, 2015), which is based on the thermal-circuit approach of Neher and McGrath (1957) and assumes sinusoidal current at the fundamental frequency.

Power-electronic loads such as variable-speed drives, rectifiers, switch-mode power supplies and LED lighting increasingly inject harmonic currents into distribution networks (Arrillaga & Watson, 2003; Institute of Electrical and Electronics Engineers [IEEE], 2022). Besides raising conductor losses through skin and proximity effects, the zero-sequence triplen harmonics (3rd, 9th, …) add in phase instead of cancelling. In a three-core cable without a neutral conductor, their net current can return only through the metallic screens, armour and earth, causing substantial additional heating (Demoulias et al., 2007; Gouda et al., 2023).

Existing harmonic derating methods are limited to correction factors for low-voltage four- and five-core cables (IEC, 2009) or to AC-resistance corrections of the conductor loss, and their adequacy for screened and armoured MV cables, where zero-sequence losses arise in the metallic layers, is not established. This paper therefore develops a coupled electromagnetic–thermal finite element model of an 11 kV three-core XLPE cable to (i) validate it against IEC 60287 under fundamental loading, (ii) quantify the conductor, screen and armour losses for each harmonic order, (iii) determine the harmonic derating factor as a function of total harmonic distortion (THD), (iv) evaluate the effects of soil thermal conductivity and cable formation, and (v) estimate the consequence for XLPE insulation life.

Literature Review / Related Work

Underground XLPE cables are widely used in medium-voltage networks for their reliability and insulation performance. However, harmonic currents raise the effective AC resistance through skin and proximity effects, concentrating current near the conductor surface and increasing losses and heat generation (Arrillaga & Watson, 2003; Demoulias et al., 2007).

Cable rating is normally based on the Neher–McGrath (1957) thermal-circuit method, formalised in IEC 60287 (IEC, 2014a, 2015). This method expresses screen and armour losses as fixed fractions of conductor loss (λ_1, λ_2). Those fractions are derived for balanced sinusoidal currents, so the method does not account for harmonics. The only standardised harmonic correction, in IEC 60364-5-52 (IEC, 2009), applies to low-voltage multi-core cables carrying triplen harmonics. It does not cover screened and armoured MV cables.

Gouda et al. (2023) experimentally showed that harmonics raise cable core temperature at rated current, and they identified the third and fifth harmonics as the main drivers of hot-spot and dry-zone formation. The present results agree on both points. The combined-harmonic hot-spot temperatures are 161.7 °C at rated current and 90.4 °C at derated current, and the third harmonic dominates the added heating despite carrying only 30% of rated current.

Rasoulpoor et al. (2017) derived a derating factor that includes bonded-sheath and armour circulating-current losses, showing these losses to be a significant contributor to heating in solidly-bonded cables. The present study traces this loss in the harmonic case to the third harmonic. Because the third harmonic is zero-sequence, its magnetic fields add across the three cores instead of cancelling, which concentrates loss in the armour.

Shazly et al. (2017) showed that the thermal impact of harmonics grows with harmonic order, so the full spectrum must be considered. This study therefore superposes six harmonic orders (h = 1, 3, 5, 7, 11, 13), since no single order reproduces the combined result. Shazly et al. also found that trefoil cables run hotter than flat formations and need greater derating. The present simulations confirm this for a different cable design, both with and without harmonics.

Alwan et al. (2024) reported that harmonics combined with high ambient temperature can push cables beyond their thermal limit. This is relevant here, since the assumed ground surface temperature of 45 °C leaves only a small thermal margin.

Demoulias et al. (2007) experimentally validated a coupled electromagnetic-thermal finite element method for ampacity reduction under non-sinusoidal current. The present study uses the same modelling approach, relying on that prior validation rather than repeating the measurements.

Taken together, these studies show that harmonics, metallic-layer losses, cable formation and installation conditions all affect cable temperature. However, each study addresses these factors separately: harmonic temperature rise (Gouda et al., 2023; Alwan et al., 2024), metallic-layer losses (Rasoulpoor et al., 2017) and formation (Shazly et al., 2017). None of them quantifies the effect on insulation life. This study applies the validated finite element approach of Demoulias et al. (2007) to a screened and armoured three-core MV cable. Each harmonic order is solved with its own phase sequence and the results are superposed. This separates conductor, screen and armour losses by order and isolates the role of the zero-sequence third harmonic. The same model is then compared with IEC 60287 and used to assess soil thermal conductivity, cable formation and insulation ageing within one framework.

Materials and Methods

Study Design

A two-dimensional (2D) coupled electromagnetic–thermal finite element method (FEM) model was developed in COMSOL Multiphysics 6.2 (COMSOL AB, 2023), assuming an infinitely long cable so that its cross-section represents the whole cable. Each harmonic order is solved as a separate frequency-domain problem and the results are superposed. The model is first validated against IEC 60287 under fundamental loading and then used for the five objectives stated in the Introduction.

Cable and Model Geometry

The study cable is an 11 kV (U_0 = 6.35 kV) three-core cable with 300 mm² aluminium conductors, XLPE insulation, copper-tape screens, polyvinyl chloride (PVC) fillers and inner sheath, galvanised steel flat-strip armour and a high-density polyethylene (HDPE) outer sheath (overall diameter 80.1 mm). Its centre is buried 1.0 m deep in soil of thermal conductivity k = 0.35 W/(m·K) (ρ = 2.86 K·m/W). Table 1 lists the material properties and Figure 1 shows the model geometry and mesh; the layer dimensions and soil domain are given in Appendix A (Tables A1 and A2).

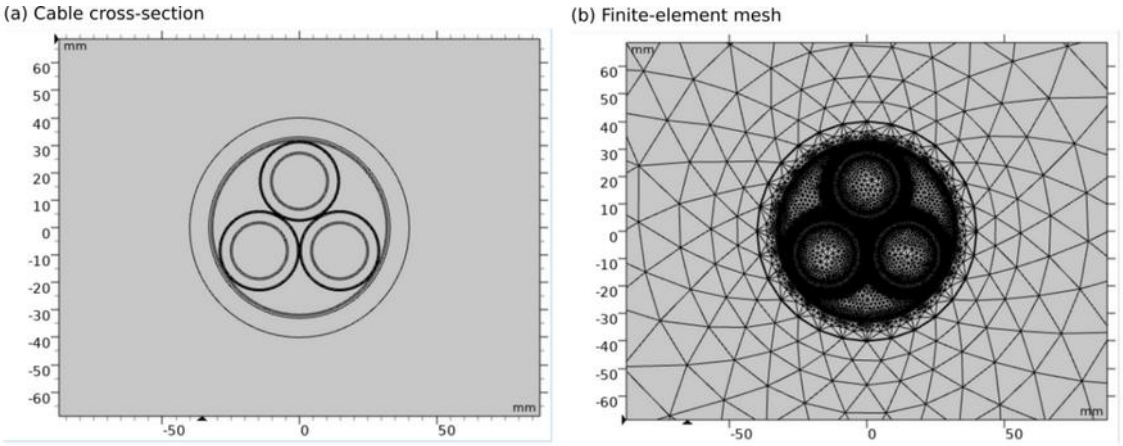
Table 1

Material Properties Used in the Model

Material	k (W/m·K)	Density (kg/m³)	C_p (J/kg·K)	ε_r	μ_r	ρ_0 (Ω·m)	α (1/K)
Aluminium conductor	238	2700	900	1	1	2.8264×10^{-8}	0.00403
Conductor screen	0.30	1150	2200	–	–	–	–
XLPE insulation	0.286	930	2000	$2.5(1 - j0.004)$	1	$\sigma = 10^{-12}$ S/m	–
Insulation screen	0.30	1100	2000	–	–	–	–
Water-swellable tape	0.20	1000	2000	–	–	–	–
Copper tape screen	400	8960	385	1	1	1.7241×10^{-8}	0.00393
PVC filler	0.17	1400	1000	–	–	–	–
PVC inner sheath	0.167	1400	1000	–	–	–	–
Galvanised steel armour	50	7800	490	1	300	2.20×10^{-7}	0.0045
HDPE outer sheath	0.38	960	1900	–	–	–	–
Soil	0.35	1800	840	–	–	–	–

Note. All materials are isotropic. Resistivities are referred to T_{ref} = 293.15 K and vary as $\rho = \rho_0[1 + \alpha(T - T_{ref})]$. Density and heat capacity do not affect the stationary solution.

Figure 1



(a) Model Geometry of the Three-Core Cable and (b) Finite-Element Mesh

Electromagnetic Formulation

The Magnetic Fields (mf) interface solves Ampère's law for the fundamental and harmonic currents, with the magnetic flux density expressed through the magnetic vector potential A:

(1)

Each harmonic order *h* is solved in the frequency domain at the angular frequency

(2)

where f_1 = 50 Hz. In the passive copper screens and steel armour, the induced electric field and current density are

(3)

The screens and armour form continuous metallic paths, which corresponds to bonding at both ends.

Electromagnetic Heating and Heat Transfer

The Electromagnetic Heating coupling passes the time-averaged electromagnetic loss density to the Heat Transfer in Solids (ht) interface:

(4)

where the first term is the resistive loss and the second is the magnetic (hysteresis) loss in the armour. The temperature follows from the steady-state heat conduction equation

(5)

The ground surface is held at 45 °C (318.15 K), the lateral and bottom soil boundaries (Table A2) are thermally insulated, and A = 0 on the outer boundary. The conductor, screen and armour resistivities are temperature-dependent, so the electromagnetic and thermal solutions are fully coupled.

Harmonic Current Excitation

Each core is modelled as a single-conductor coil. For harmonic order *h*, the current phasor in core *k* is

(6)

The fundamental amplitude is I_1 = 304 A peak (215 A root-mean-square, RMS), as COMSOL frequency-domain coil inputs are peak values. The phase angles follow the sequence of each order (Table 2): positive for h = 1, 7 and 13, negative for h = 5 and 11, and zero for the third harmonic, whose three in-phase currents add rather than cancel. The 5th to 13th harmonic fractions follow an approximate 1/h characteristic, and the 30% third harmonic represents an assumed contribution from single-phase non-linear loads, since a six-pulse load generates no triplen harmonics. The total harmonic distortion is

(7)

which is 40.5% for the base spectrum. Lower THD levels were obtained by scaling all harmonic fractions by k_{THD} = THD/40.5%, preserving the shape of the spectrum.

Only six harmonic orders (*h* = 1, 3, 5, 7, 11 and 13) were modelled in this study. Each represents a distinct heating mechanism, and together they carry almost all the harmonic current of typical non-linear loads (Arrillaga & Watson, 2003; IEEE, 2022):

Fundamental (*h* = 1, 50 Hz): carries the load current and gives the main conductor I^2R loss, the reference for each harmonic.

Third harmonic (*h* = 3, 150 Hz): zero-sequence harmonic from single-phase non-linear loads; its in-phase currents return through the screens and armour, causing neutral-path heating.

Fifth harmonic (*h* = 5, 250 Hz): largest six-pulse harmonic ($h = 6n \pm 1$); the skin effect raises the conductor AC resistance and loss.

Seventh harmonic (*h* = 7, 350 Hz): next six-pulse harmonic; the proximity effect between the cores adds to the skin effect.

Eleventh and thirteenth harmonics (*h* = 11 and 13; 550 and 650 Hz): six- and twelve-pulse harmonics ($h = 12n \pm 1$); small amplitudes (about $1/h$) but a measurable heating contribution.

All other orders were excluded. Even harmonics are negligible because converter currents have half-wave symmetry, and orders above the 13th are below about 8% of the fundamental; since the 11th and 13th harmonics together add only about 2 K to the conductor temperature (Table 3), higher orders would contribute even less. The 9th harmonic, also a zero-sequence order, was not modelled; because its losses would add to those of the third harmonic in the screens and armour, the results may slightly underestimate the heating where a significant 9th harmonic is present. The selected orders and their sequences are summarised in Table 2.

The zero-sequence third harmonic reaches the 11 kV cable only where a zero-sequence path exists, such as multi-earthed four-wire feeders with YNyn transformers, delta systems earthed through zig-zag transformers, or star-earthed capacitor banks; in conventional delta-fed Dyn11 networks, triplen currents circulate in the delta winding and do not enter the MV cable (Arrillaga & Watson, 2003; Dugan et al., 2012). The assumed 30% third harmonic therefore represents feeders with such a zero-sequence path.

Table 2

Harmonic Spectrum and Phase Sequence

Order h	Frequency (Hz)	I_h/I_1	Sequence	Phase angles A, B, C
1	50	1.00	Positive	0°, −120°, +120°
3	150	0.30	Zero	0°, 0°, 0°
5	250	0.20	Negative	0°, +120°, −120°
7	350	0.14	Positive	0°, −120°, +120°
11	550	0.09	Negative	0°, +120°, −120°
13	650	0.08	Positive	0°, −120°, +120°

Because the harmonic losses add, the total conductor temperature is obtained by superposing the temperature rise of each harmonic solution:

(8)

Rating, Loss and Ageing Evaluation

Current ratings were found by solving each case at two currents bracketing the 90 °C limit, interpolating in I^2 and confirming with a final run (90.0 ± 0.03 °C). Derated currents at intermediate THD levels were obtained by scaling the FEM temperature rises with a resistance–temperature correction calibrated to the full FEM results at 0% and 40.5% THD. Losses were obtained by integrating Q over the conductors, screens and armour for each harmonic. Dielectric loss ($W_d = \omega C U_0^2 \tan\delta = 0.076$ kW/km) is below 0.5% of the total and was neglected (IEC, 2014a). The IEC 60287 reference rating used the same cable data and current.

The harmonic derating factor is the ratio of the fundamental current that keeps the conductor at 90 °C under harmonic loading to the rated current under sinusoidal loading:

(9)

The relative thermal life of the XLPE insulation was estimated from the Arrhenius relation

(10)

with an activation energy $E_a = 0.9$ eV and Boltzmann constant $k_B = 8.617\times10^{-5}$ eV/K.

Results

Temperature Rise per Harmonic Order

At the rated fundamental current of 304 A peak (215 A RMS), with k = 0.35 W/(m·K) and the 40.5% THD spectrum of Table 2, the fundamental alone raised the conductor to 90.35 °C (Table 3), confirming 304 A peak as the rating under sinusoidal loading. The third harmonic gave the largest temperature contribution, about 1.4 times that of the fundamental, although its current is only 30% of the fundamental current. The 5th to 13th harmonics together contributed only 7.26 K. Figure 2 compares the temperature fields of the fundamental and the third harmonic. This third-harmonic heating requires a zero-sequence path to the cable (see Harmonic Current Excitation) and would be largely absent in a delta-fed Dyn11 feeder.

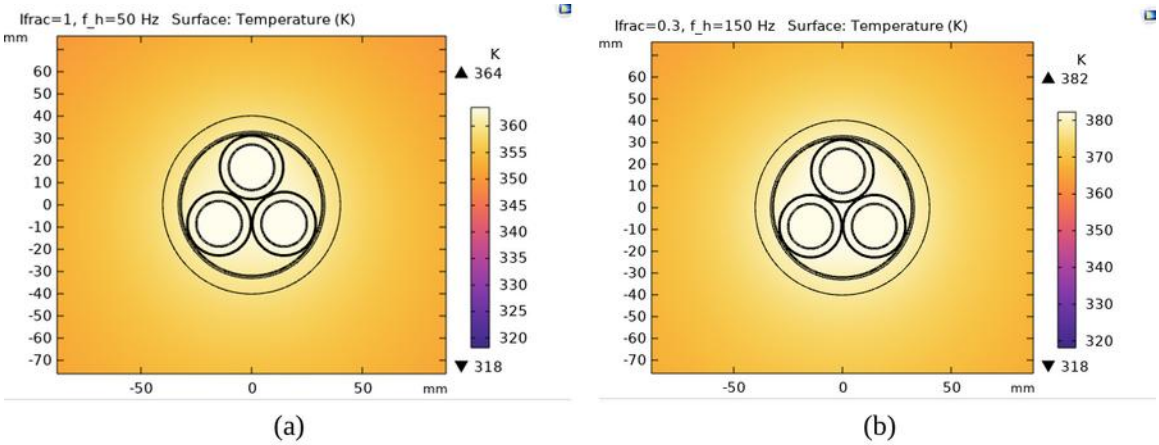
Table 3

Maximum Conductor Temperature and Temperature Contribution per Harmonic Order (k = 0.35 W/(m·K), 40.5% THD)

h	**f_h (Hz)**	**I_{frac}**	**T at 304 A peak (K)**	**ΔT at 304 A peak (K)**	**T at 198 A peak (K)**	**ΔT at 198 A peak (K)**
1	50	1.00	363.50	45.35	335.93	17.78
3	150	0.30	382.24	64.09	342.72	24.57
5	250	0.20	321.30	3.15	319.48	1.33
7	350	0.14	320.09	1.94	318.97	0.82
11	550	0.09	319.29	1.14	318.63	0.48
13	650	0.08	319.18	1.03	318.59	0.44
Total				**116.70**		**45.42**
T_{total} (°C)				**161.70**		**90.42**

Note. ΔT is the rise of the maximum conductor temperature above the 318.15 K (45 °C) ambient for each harmonic solution; T_{total} is obtained with Equation 8. 304 A peak = 215 A RMS; 198 A peak = 140 A RMS.

Figure 2



Temperature Distribution at 304 A Peak: (a) Fundamental (h = 1, 50 Hz) and (b) Third Harmonic (h = 3, 150 Hz)

Magnetic Flux Density

At 304 A peak, the third harmonic produced a maximum flux density about 47% higher than that of the fundamental (Table 4), concentrated in the steel armour (Figure 3), whereas the 5th to 13th harmonics produced only 0.012–0.024 T. At 198 A peak the flux densities fell approximately in proportion to the current, and the third harmonic remained dominant.

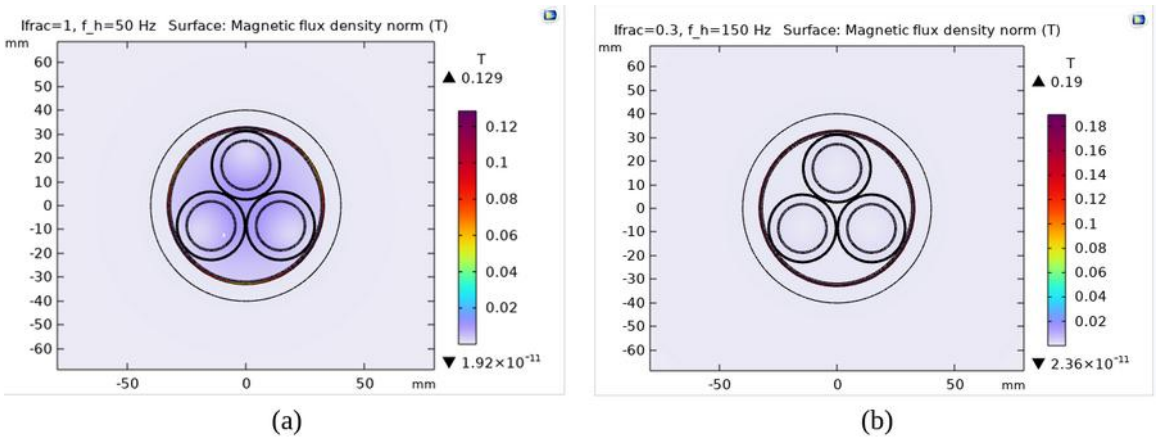
Table 4

Maximum Magnetic Flux Density per Harmonic Order (k = 0.35 W/(m·K), 40.5% THD)

h	f_h (Hz)	I_{frac}	B_{max} at 304 A peak (T)	B_{max} at 198 A peak (T)
1	50	1.00	0.1286	0.0837
3	150	0.30	0.1897	0.1147
5	250	0.20	0.0242	0.0158
7	350	0.14	0.0175	0.0114
11	550	0.09	0.0125	0.0081
13	650	0.08	0.0116	0.0076

Note. B_{max} *is the maximum of the magnetic flux density norm over the model cross-section.*

Figure 3



Magnetic Flux Density Norm at 304 A Peak: (a) Fundamental (h = 1, 50 Hz) and (b) Third Harmonic (h = 3, 150 Hz)

Power Losses per Harmonic Order

Table 5 and Figure 4 give the losses per unit length in the conductors, screens and armour for each harmonic order. Under the fundamental alone, 97% of the 17.27 kW/km total loss occurred in the conductors. The third harmonic produced a larger total loss (25.06 kW/km) than the fundamental.

Only 1.64 kW/km of this third-harmonic loss occurred in the conductors. With the full 40.5% THD spectrum, the conductor loss increased by 21%, whereas the total cable loss increased by 161%. Of the 27.85 kW/km of additional harmonic loss, 24.37 kW/km (88%) occurred in the armour and copper-tape screens.

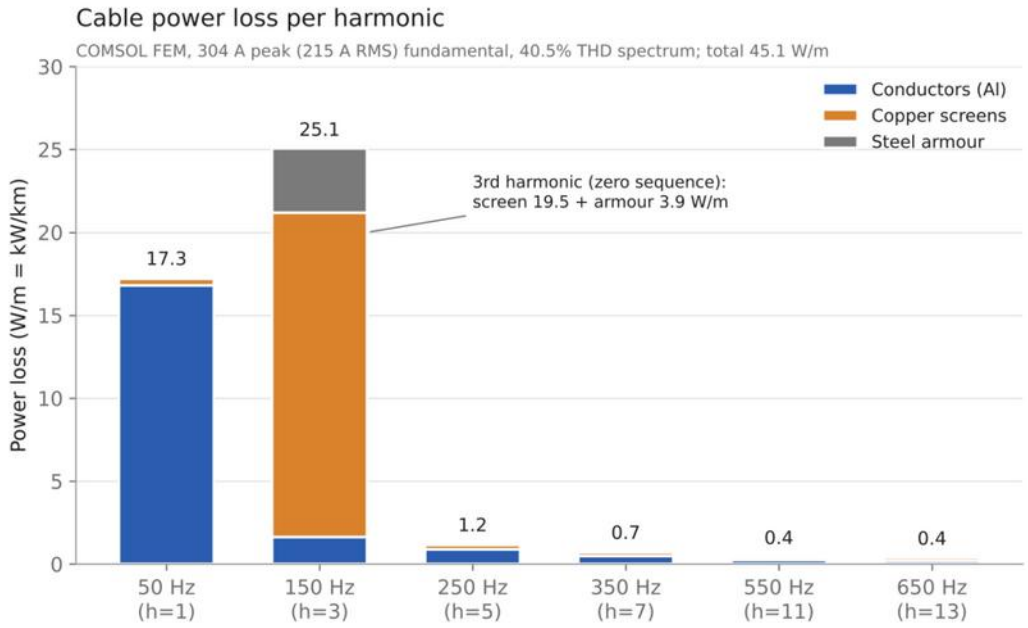
Table 5

Power Loss per Harmonic Order at 304 A Peak (k = 0.35 W/(m·K), 40.5% THD, 45 °C Ground)

h	f_h (Hz)	I_{frac}	Conductors (kW/km)	Total (kW/km)
1	50	1.00	16.814	17.271
3	150	0.30	1.638	25.056
5	250	0.20	0.896	1.209
7	350	0.14	0.499	0.748
11	550	0.09	0.245	0.439
13	650	0.08	0.206	0.398
Total			**20.297**	**45.121**

Note. Losses are the surface integrals of the electromagnetic loss density Q_e over the three conductors, the three copper-tape screens and the armour (1 W/m = 1 kW/km).

Figure 4



Cable Power Loss per Harmonic Order, Separated into Conductor, Screen and Armour Losses

Under fundamental loading, the FEM conductor and total losses agree with IEC 60287 (IEC, 2014a) within 2.7% and 3.4%, respectively (Table 6), which validates the electromagnetic model. In both methods, the screen and armour losses are about 3% of the total.

Table 6

Comparison of FEM Losses With IEC 60287 Under Fundamental Loading (304 A Peak, 0% THD, k = 0.35 W/(m·K), 45 °C Ground)

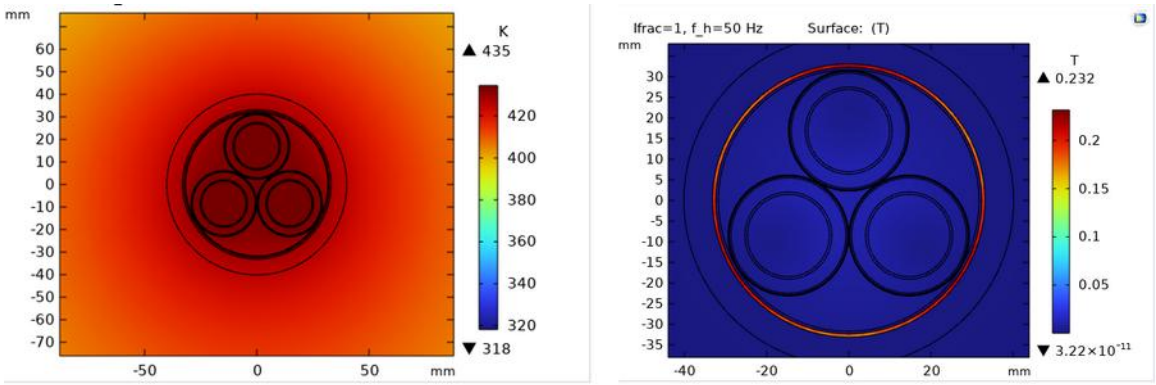
Loss component	IEC 60287 (kW/km)	FEM (COMSOL) (kW/km)	Difference
Conductor loss (three cores)	16.38	16.81	+0.43 (+2.7%)
Screen loss (three copper tapes)	0.17	0.38	–
Armour loss	0.16	0.08	–
Total loss	**16.71**	**17.27**	**+0.56 (+3.4%)**

Note. IEC 60287 screen and armour losses are calculated with the loss factors $\lambda_1 = 0.0105$ and $\lambda_2 = 0.0098$ ($W_s = \lambda_1 W_c$, $W_a = \lambda_2 W_c$). Dielectric loss is excluded from both methods.

Combined Temperature and Derated Current

Superposing the six harmonic solutions (Equation 8) gives a maximum conductor temperature of 161.7 °C at 304 A peak and 40.5% THD, 71.7 K above the 90 °C limit of XLPE (Figure 5a). The combined flux density in the armour reaches 0.232 T (Figure 5b). Reducing the fundamental current to 198 A peak (140 A RMS) brings the conductor back to 90.4 °C (Table 3), a harmonic derating factor of DF = 0.65 (Equation 9). For comparison, an IEC 60287-based correction that only increases the conductor AC resistance gives DF = 0.91 for the same spectrum. At the derated current, the third harmonic still contributes more to the temperature rise than the fundamental. Because the zero-sequence third harmonic causes most of this temperature rise, the derating factor of 0.65 applies to feeders with a zero-sequence path; where the third harmonic is blocked, as in delta-fed Dyn11 networks, much less derating would be required.

Figure 5



Combined Results at 304 A Peak and 40.5% THD: (a) Total Temperature Distribution and (b) Combined Magnetic Flux Density Norm

Effect of Total Harmonic Distortion

Table 7 gives the conductor temperature at the rated current, the derated current and the relative insulation life as functions of THD. Up to 5% THD, the typical IEEE 519 limit (IEEE, 2022), the temperature rise is below 1 K and the derating below 1%. Above about 10% THD the temperature rises steeply, and the derating factor falls to 0.87 at 20% and 0.65 at 40.5% THD.

These values assume that the third harmonic scales with the rest of the spectrum and reaches the cable through a zero-sequence path.

Table 7

Conductor Temperature, Derated Current and Relative Insulation Life Versus THD

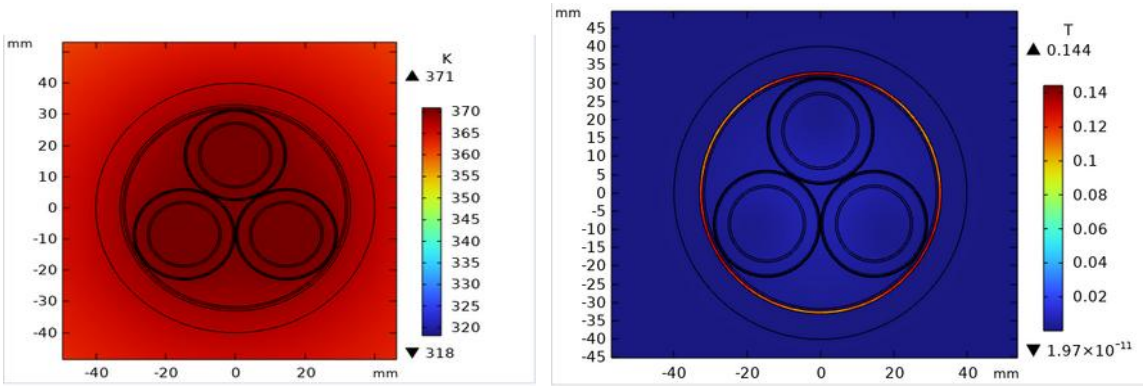
THD (%)	T at 215 A RMS (°C)	Derated current, peak / RMS (A)	Derating factor	Relative life at 215 A
0	90.2	304 / 215	1.000	1.00
5	91.2	301 / 213	0.990	0.93
10	94.0	293 / 207	0.963	0.73
15	98.8	280 / 198	0.922	0.52
20	105.7	265 / 187	0.872	0.31
30	126.6	232 / 164	0.762	–
40.5	161.7	198 / 140	0.651	–

Note. Temperatures are full FEM results. Derated currents at 0% and 40.5% THD are FEM results; intermediate values are calibrated estimates. Relative life is evaluated with Equation 10 relative to 0% THD and is not reported above about 110 °C.

Effect of Soil Thermal Conductivity

Reducing the soil thermal conductivity by 14.3%, from 0.35 to 0.30 W/(m·K) to represent drier soil, raised the maximum temperature of the derated case (198 A peak, 40.5% THD) from about 90 °C (363 K) to 98 °C (371 K) (Figure 6). The maximum flux density was unchanged (0.144 T), so this 8 K rise is due entirely to reduced heat dissipation in the soil. Soil drying alone therefore pushed the cable above its 90 °C limit without any change in current.

Figure 6



Results at 198 A Peak, 40.5% THD and Soil Thermal Conductivity of 0.30 W/(m·K): (a) Total Temperature Distribution and (b) Magnetic Flux Density Norm

Under sinusoidal loading, the FEM rating at 90 °C, verified by direct simulation, increases from 210 A to 381 A RMS (+82%) across the IEC soil range (ρ = 3.0–0.7 K·m/W) (Table 8).

Table 8

Current Rating at 90 °C Versus Soil Thermal Conductivity (0% THD)

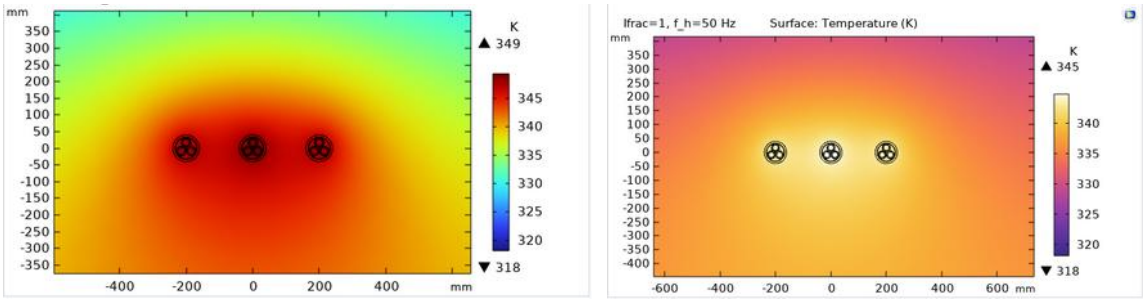
k (W/(m·K))	ρ (K·m/W)	FEM rating, RMS (A)
0.333	3.0	209.7
0.50	2.0	251.2
0.667	1.5	284.1
0.833	1.2	311.1
1.00	1.0	334.2
1.43	0.7	381.1

Flat and Trefoil Formations

Flat Formation

Three cables in flat formation at 0.2 m centre-to-centre spacing, each carrying 160 A peak, were simulated with and without 28% THD (Figure 7 and Table 9). The harmonics raised the maximum temperature of the central cable by 4.53 K, to 76.2 °C (349.35 K).

Figure 7



Temperature Distribution for Three Cables in Flat Formation at 160 A Peak Each: (a) With Harmonics (28% THD) and (b) Without Harmonics

Table 9

Cable Temperature at 160 A Peak With and Without Harmonics (THD = 28%), Flat Formation

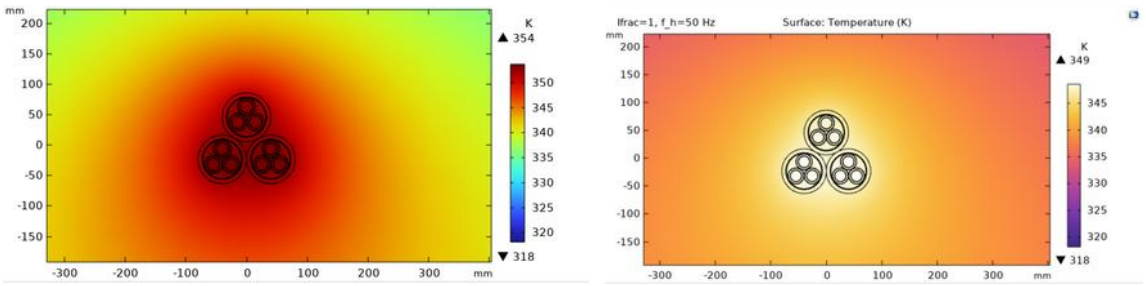
Load (A)	Cable Position	Cable Temperature Without Harmonics (K)	Cable Temperature With Harmonics (K)
160 A peak	Cable (1) (L)	343.60	347.96
	Cable (2) (M)	344.82	349.35
	Cable (3) (R)	343.60	347.96

Note. L, M and R denote the left, middle and right cables.

Trefoil Formation

In trefoil formation (Figure 8 and Table 10), the harmonics raised the maximum temperature of the central cable by 4.58 K, to 80.0 °C (353.18 K).

Figure 8



Temperature Distribution for Three Cables in Trefoil Formation at 160 A Peak Each: (a) With Harmonics (28% THD) and (b) Without Harmonics

Table 10

Cable Temperature at 160 A Peak With and Without Harmonics (THD = 28%), Trefoil Formation

Load (A)	Cable Position	Cable Temperature Without Harmonics (K)	Cable Temperature With Harmonics (K)
160 A peak	Cable (1) (L)	348.55	353.14
	Cable (2) (M)	348.60	353.18
	Cable (3) (R)	348.55	353.14

Note. L, M and R denote the left, middle and right cables.

Under the same load and harmonic spectrum, the trefoil formation therefore ran about 3.8 K hotter than the flat formation. The tighter thermal and magnetic coupling in trefoil raises the baseline temperature, and the harmonic contribution is slightly larger (4.58 K compared with 4.53 K) because of the additional mutual heating and metallic-layer losses.

Effect of Cable Spacing in Flat Formation

The flat formation (160 A peak per cable, 0% THD, k = 0.35 W/(m·K), 45 °C ground) was also simulated at centre-to-centre spacings from 80.1 mm (touching) to 600 mm (Table 11).

Table 11

Conductor Temperature Versus Cable Spacing, Flat Formation, 160 A Peak, 0% THD

Spacing (mm)	L (K)	M (K)	R (K)	M − L/R (K)
80.1	347.40	348.15	347.40	0.75
100	346.48	347.46	346.48	0.98
200	343.60	344.82	343.60	1.22
300	342.05	343.19	342.05	1.14
400	341.12	342.09	341.12	0.97
600	340.41	340.74	340.41	0.33

Note. L, M and R denote the left, middle and right cables; M − L/R is the temperature difference between the middle and outer cables.

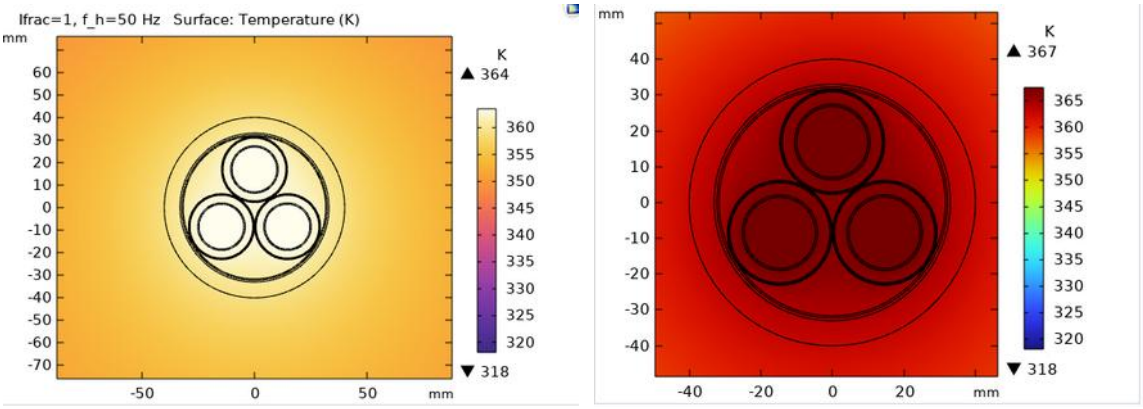
The conductor temperature decreased with spacing as mutual heating was reduced: between 80.1 and 600 mm, the central cable cooled by 7.41 K and the outer cables by 6.99 K. The reduction is non-linear, with 45% of it achieved by 200 mm, 82% by 400 mm and only 1.35 K gained between 400 and 600 mm. Spacing beyond about 400 mm therefore offers little thermal benefit relative to the additional trench width.

The central cable was the hottest at all spacings, being heated from both sides, while the outer cables had equal temperatures by symmetry. The middle-to-outer temperature difference peaked at 1.22 K at 200 mm: at touching spacing the thin soil layer between the cables equalises their temperatures, while at large spacings mutual heating diminishes. All cables remained below the 90 °C limit, with a maximum of 75.0 °C (348.15 K).

Effect on Insulation Life

Figure 9 compares the temperature distribution at 304 A peak for fundamental-only loading and with 10% THD. The 10% THD raises the maximum conductor temperature by about 4 K, from T_1 = 90 °C (363.15 K) to T_2 = 94 °C (367.15 K) (Table 7). Applying the Arrhenius relation (Equation 10) with E_a = 0.9 eV gives L_2/L_1 = 0.731 (Appendix A), so this rise of only 4 °C reduces the expected thermal life of the XLPE insulation by about 27%.

Figure 9



Temperature Distribution at the Rated Current of 304 A Peak: (a) Fundamental Only (h = 1, 50 Hz) and (b) Total With 10% THD

Discussion

The results show that harmonic heating in a screened and armoured three-core MV cable is governed by the phase sequence of each harmonic order rather than by its magnitude. Positive- and negative-sequence currents are balanced, so their fields largely cancel outside the cores, and under fundamental loading the metallic layers carry only about 3% of the total loss. The zero-sequence third harmonic behaves differently: its three in-phase currents produce additive fields that induce large circulating currents in the copper screens and steel armour. This explains why a third harmonic of only 30% of the fundamental produced a larger temperature rise than the fundamental itself (64.1 K vs. 45.4 K), and why 88% of the additional harmonic loss occurred in the metallic layers rather than the conductors. These findings agree with the dominant role of triplen harmonics reported by Demoulias et al. (2007) for low-voltage cables and with the circulating-current losses identified by Rasoulpoor et al. (2017), and extend them by attributing the losses to individual harmonic orders and cable components.

This has direct consequences for rating practice. The IEC 60287 loss factors λ_1 and λ_2 assume balanced sinusoidal currents, and a correction that only increases the conductor AC resistance gives a derating factor of 0.91 for the 40.5% THD spectrum, compared with 0.65 from the coupled FEM model. A conductor-only correction would therefore overestimate the permissible current by about 40%. Conversely, harmonics are negligible (below 1 K) at the 5% THD

typically permitted by IEEE 519 (IEEE, 2022), so the risk is concentrated in networks above about 10% THD, particularly where single-phase non-linear loads introduce a significant third harmonic.

Installation conditions compound the harmonic effect. Drier soil (0.30 instead of 0.35 W/(m·K)) added 8 K at the derated current, and the sinusoidal rating varied by 82% across the IEC soil range. The trefoil formation ran about 3.8 K hotter than the flat formation, in agreement with Shazly et al. (2017), while flat spacing beyond about 400 mm gave little further benefit. Consistent with Gouda et al. (2023) and Alwan et al. (2024), who reported that harmonics combined with high soil resistivity or ambient temperature can push MV cables beyond their thermal limit, the 45 °C ground surface assumed here leaves only a small margin. Harmonics, soil drying and formation must therefore be assessed together rather than as independent correction factors.

Limitations

The model is two-dimensional and steady-state. It omits the helical lay of the cores and armour wires, whose induced fields partly cancel along a real cable, so it probably overestimates the metallic-layer losses, particularly in the armour. End effects and cyclic or transient loading are not represented. The screens and armour are treated as bonded at both ends; single-point or cross-bonded systems would carry much smaller circulating currents, particularly at the third harmonic. The soil is homogeneous with constant thermal conductivity and a 45 °C surface temperature, and moisture migration and dry-zone formation are represented only through the reduced-conductivity case.

Only one cable (11 kV, 300 mm², three-core XLPE) and one harmonic spectrum were studied. The spectrum, including the 30% third harmonic, is assumed rather than measured, so the numerical results (e.g., DF = 0.65) apply to this case, although the zero-sequence mechanism is general. For conventional delta-fed Dyn11 networks, where triplen currents are blocked from the MV cable, the third-harmonic results represent an upper bound.

The model was validated against IEC 60287 under fundamental loading only, not against measurements under harmonic loading, so the harmonic results rely on the validation of the same approach by Demoulias et al. (2007). The IEC-based derating factor of 0.91 is a conductor-only AC-resistance correction, because IEC 60287 has no harmonic procedure for screened and armoured MV cables. Finally, the life estimate covers thermal ageing only and depends on the assumed activation energy; over the typical range of 0.8–1.0 eV, the life reduction at 10% THD is about 24–29%.

Conclusion

A coupled electromagnetic–thermal finite element model, validated against IEC 60287, shows that the zero-sequence third harmonic is the dominant cause of harmonic heating in screened and armoured three-core MV cables. Its additive fields shift the loss from the conductors to the copper screens and steel armour, so that a 40.5% THD spectrum raises the conductor loss by only 21% but the total cable loss by 161%. As a result, the required derating factor (0.65) is far lower than that given by a conductor-only IEC 60287 AC-resistance correction (0.91).

Ratings based on sinusoidal current therefore overestimate the ampacity of MV cables supplying non-linear loads. The margin is further reduced by drier soil, trefoil formation and close spacing,

and even 10% THD shortens the expected insulation life by about 27%. Ratings for such cables should account for metallic-layer losses for each harmonic order together with formation and soil conditions, particularly where THD exceeds about 10% or single-phase non-linear loads are significant. Future work should include transient and cyclic loading, other bonding arrangements, soil moisture migration and experimental validation with measured harmonic spectra.

Acknowledgments

The authors thank the Department of Electrical Engineering, Pulchowk Campus, Institute of Engineering, Tribhuvan University, for providing the facilities and academic support for this study. The authors also thank the faculty members and colleagues of the department for their valuable suggestions and encouragement during this work.

Funding

The author(s) received no financial support for the research, authorship, or publication of this paper.

Conflict of Interest

The author(s) declare no conflict of interest.

Author Contributions

Krishna Raj Majhi: conceptualization, methodology, software, formal analysis, investigation, visualization and writing – original draft. Bishal Silwal: supervision, validation and writing – review and editing.

Data Availability

The data and simulation models supporting the findings of this study are available from the corresponding author upon reasonable request.

References

Alwan, S. H., Jasim, A. K., & Hassan, Y. F. (2024). Thermal behavior of insulated cables under the influence of harmonics in hot countries. *International Journal on Energy Conversion, 12*(1), 24–31. https://doi.org/10.15866/irecon.v12i1.24374

Arrillaga, J., & Watson, N. R. (2003). *Power system harmonics* (2nd ed.). John Wiley & Sons.

COMSOL AB. (2023). *COMSOL Multiphysics* (Version 6.2) [Computer software]. https://www.comsol.com

Demoulias, C., Labridis, D. P., Dokopoulos, P. S., & Gouramanis, K. (2007). Ampacity of low-voltage power cables under nonsinusoidal currents. *IEEE Transactions on Power Delivery, 22*(1), 584–594. https://doi.org/10.1109/TPWRD.2006.881445

Dugan, R. C., McGranaghan, M. F., Santoso, S., & Beaty, H. W. (2012). *Electrical power systems quality* (3rd ed.). McGraw-Hill.

Gouda, O. E., El Dein, A. Z., Tag-Eldin, E., Lehtonen, M., & Darwish, M. M. F. (2023). Thermal analysis of the influence of harmonics on the current capacity of medium-voltage underground power cables. *Energy Science & Engineering, 11*(10), 3471–3485. https://doi.org/10.1002/ese3.1534

Institute of Electrical and Electronics Engineers. (2022). *IEEE standard for harmonic control in electric power systems* (IEEE Std 519-2022).

International Electrotechnical Commission. (2009). *Low-voltage electrical installations – Part 5-52: Selection and erection of electrical equipment – Wiring systems* (IEC 60364-5-52:2009).

International Electrotechnical Commission. (2014a). *Electric cables – Calculation of the current rating – Part 1-1: Current rating equations (100% load factor) and calculation of losses – General* (IEC 60287-1-1:2006+AMD1:2014).

International Electrotechnical Commission. (2014b). *Power cables with extruded insulation and their accessories for rated voltages from 1 kV (U_m = 1.2 kV) up to 30 kV (U_m = 36 kV) – Part 2: Cables for rated voltages from 6 kV (U_m = 7.2 kV) up to 30 kV (U_m = 36 kV)* (IEC 60502-2:2014).

International Electrotechnical Commission. (2015). *Electric cables – Calculation of the current rating – Part 2-1: Thermal resistance – Calculation of the thermal resistance* (IEC 60287-2-1:2015).

Neher, J. H., & McGrath, M. H. (1957). The calculation of the temperature rise and load capability of cable systems. *Transactions of the American Institute of Electrical Engineers. Part III: Power Apparatus and Systems, 76*(3), 752–764. https://doi.org/10.1109/AIEEPAS.1957.4499653

Rasoulpoor, M., Mirzaie, M., & Mirimani, S. M. (2017). Thermal assessment of sheathed medium voltage power cables under non-sinusoidal current and daily load cycle. *Applied Thermal Engineering, 123*, 353–364. https://doi.org/10.1016/j.applthermaleng.2017.05.070

Shazly, J. H., Mostafa, M. A., Ibrahim, D. K., & Abo El Zahab, E. E. (2017). Thermal analysis of high-voltage cables with several types of insulation for different configurations in the presence of harmonics. *IET Generation, Transmission & Distribution, 11*(14), 3439–3448. https://doi.org/10.1049/iet-gtd.2016.0862

Appendix A

Model Input Data

Tables A1 and A2 give the cable layer dimensions and the soil domain used in the finite element model.

Table A1

Cable Layer Dimensions

S.N.	Layer	Material	Outer radius (mm)	Inner radius (mm)	Thickness (mm)
1	Outer sheath	HDPE	40.05	33.05	7.00
2	Armour	Galvanised steel flat strip	33.05	32.25	0.80
3	Inner sheath	PVC	32.25	31.65	0.60
4	Filler (interstice region)	PVC	31.65	Bounded by the three cores	Irregular
5	Metallic screen	Copper tape	14.65	14.55	0.10
6	Water-blocking layer	Water-swellable tape	14.55	14.35	0.20
7	Insulation screen	Semiconductive	14.35	13.95	0.40
8	Insulation	XLPE	13.95	10.55	3.40
9	Conductor screen	Semiconductive	10.55	9.95	0.60
10	Conductor	Aluminium	9.95	–	–

Note. Layers 1–4 are measured from the cable centre; layers 5–10 are measured from the centre of each core and are identical for the three cores.

Table A2

Surrounding Soil Domain

Parameter	Value
Shape	Rectangle with circular cable cut-out
Width × height	2000 mm × 2000 mm
Reference corner	(−1000, −1000) mm
Extents	x: −1000 to 1000 mm; y: −1000 to 1000 mm
Embedded cut-out	Cable outer boundary, Ø 80.1 mm, centre (0, 0)
Burial depth	1000 mm below the soil surface (top boundary at y = 1000 mm)
Soil surface boundary	Fixed temperature, 318.15 K (45 °C)

Note. The cable centre is at the origin. The same 2000 mm × 2000 mm soil domain is used for the flat-formation models, with the three cables centred at x = −200, 0 and 200 mm (y = 0).

Arrhenius Insulation-Life Calculation

For 10% THD at the rated current of 304 A peak, T_1 = 363.15 K, T_2 = 367.15 K, E_a = 0.9 eV and $k_B = 8.617 \times 10^{-5}$ eV/K. Equation 10 then gives:

The relative thermal life is therefore 73.1% of the life at 90 °C, a reduction of about 27%.

Physics-Informed Machine Learning Framework for Detection and Quantification of Bearing Faults in Induction Machine Using Electrical Signature Analysis

Nikil Gautam[1], Dr Bishal Silwal[2*]

[1] Department of Electrical Engineering, Pulchowk Campus, IOE, TU
Pulchowk, Lalitpur, Nepal
080mspse013.nikil@pcampus.edu.np
[*] bishal.silwal@pcampus.edu.np

Abstract

Conventional data-driven models learn fault patterns without explicitly considering the physical relationships associated with bearing faults, while physics-based approaches can involve detailed modelling and computational requirements. These limitations motivate integrating data-driven learning with analytical physical information. An induction motor model in MATLAB is used for data generation and introduces bearing faults as a periodically varying mutual inductance. The framework utilizes the Fast Fourier Transform to extract sub-band spectra from stator current signals as the input to a one-dimensional Convolutional Neural Network (CNN), which extracts hierarchical features from the spectral representation. An analytical bearing model provides the characteristic frequencies based on bearing geometry and rotor speed. A combined loss function integrates the data-driven and physics-based components by constraining the CNN predictions with the physical reference. The framework was evaluated using healthy and faulty operating conditions, including independent test signals. The model achieved an F1-score of 1.00 for fault classification on the independent test set, while providing severity estimates.

Keywords: Induction Machine; Bearing Faults, Electrical Signature Analysis (ESA), Physics-Informed Machine Learning (PIML), Convolutional Neural Network (CNN)

Introduction

In modern industrial applications, induction machines are often operating under variable loading conditions and harsh environments like temperature, humidity, and dust. Due to these unfavorable conditions, the machines are continuously subjected to both electrical and mechanical stress that leads to various faults in the machine. Despite the robustness of the machine, gradual degradation of the machine over time deteriorates overall performance and efficiency if the faults are not detected in earlier stages. Therefore, unplanned motor failure that results in downtime causes a huge amount of time, manpower, and financial loss. Various technological advancements provide opportunities to utilize signal analysis, modeling techniques, and intelligent algorithms for advanced condition monitoring of induction machines. Induction machines may be subjected to different types of faults such as stator faults, broken rotor bar faults, bearing faults, and so on. The most common mode of failure in machines is bearing faults, which account for 30% to 40% of machine failures according to the study of IEEE and JEMA surveys (Zhang et al. 2020).

The bearing of the machine is composed of four primary components, namely, cage, inner race, outer race, and rolling element (ball). The bearing mechanism provides smooth rotation of the rotor, minimizing friction through the dynamic interaction of these components. Any defect in these components of the bearing is termed a bearing fault.

Electrical signature analysis is a non-invasive condition monitoring approach where the electrical signal, particularly stator current, is measured using various current sensors, and various features of that current are analyzed to explain the health condition of the system. For an induction motor, the electrical signal can be measured directly from the supply, unlike mechanical monitoring that requires additional sensors for analysis.

When faults occur in the machine, they disturb its electromagnetic behavior, which is reflected in the electrical signals. Any faults, including bearing faults, disturb the air-gap magnetic field and modulate the stator current of an induction motor, resulting in additional frequency components in the stator current. Moreover, different types of faults disturb the electromagnetic behavior differently, so the modulation in the current spectrum is also distinguishable.

The characteristic frequency associated with the different types of faults can be expressed by the equation below:

Where; Nb = Number of balls; fr = rotor frequency; d = rolling element diameter; D = pitch diameter; = contact angle.

Motor current signature analysis performs a Fast Fourier Transform to convert the time-domain data into the frequency domain, allowing the additional frequency components associated with the faults to be analyzed clearly.

Conventional approaches such as vibration, spectrum, and acoustic analysis are well established and physically interpretable, but they have limitations in early detection and noisy environments. Data-driven artificial intelligence approaches have shown promising results in fault diagnosis, but they may require large datasets and often have limitations in physical constraints. Physics-based methods such as finite element analysis can provide accurate results, but their computation is complex and time-consuming. Furthermore, most existing approaches focus mainly on fault detection, while severity quantification remains a significant gap.

The main objective of this study is to develop a framework for detection and quantification of bearing faults in induction machines using electrical signatures, where physical laws and equations are used to constrain the machine learning process.

Literature Review / Related Work

Zhang et al. (2020), in *IEEE Transactions on Industry Applications*, proposed a method for quantifying bearing fault severity in induction machines using electrical measurements and sought to bridge the gap between radial vibrations and stator current spectral components.

C. Vinothraj et al. (2018) in the International Journal of Engineering and Technology consider the finite element method superior, as it includes non-linear effects in modeling and analyzing the electromagnetic field of an induction machine.

According to S. Zhang, S. Zhang, B. Wang, and T. G. Habetler, CNN is able to autonomously learn useful features for bearing fault detection from the raw data pre-processed by a scaled

discrete Fourier transform. The result demonstrates that the feature learning-based approach significantly outperforms the feature engineering-based approach of conventional ML.

Ji, Dai Yan et al. (2025) in IEEE International Electric Machines and Drives Conference present that motor current signature analysis conducts detailed analysis and aligns specific frequency components in the stator current signatures with the related fault.

According to the study made by S shen on “A physics-based deep learning approach for bearing fault detection”, existing deep learning algorithms can detect bearing faults but do not incorporate physical knowledge into learning and predicting data.

Methodology

The overall methodology is divided into four phases. These phases can be named as data generation, data preprocessing and sub-band extraction, PIML architecture, and optimization with severity quantification. The flowchart in Figure 1 shows the sequential development of the work from input raw data to output severity metrics.

Figure 1

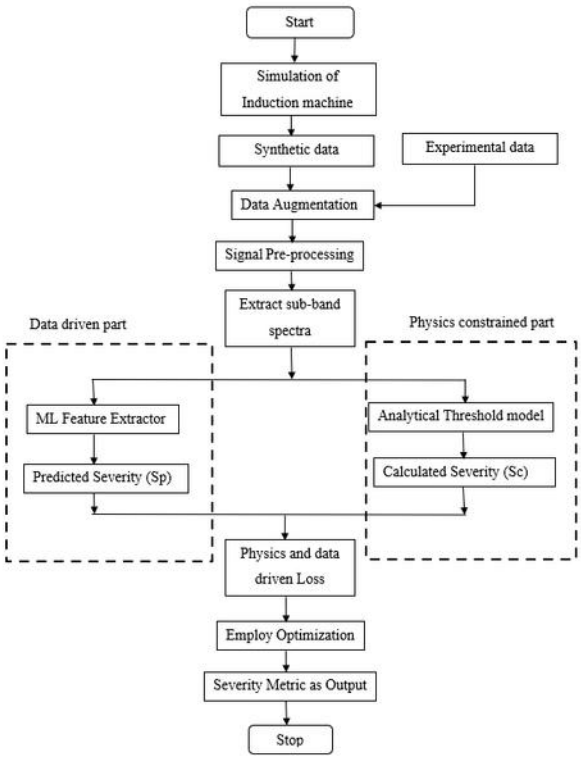


Figure 1
Flowchart of overall methodology

Data Generation and Bearing Fault Modeling

An induction motor model was developed using standard voltage and flux linkage equations in the synchronous dq frame. It generated datasets that represent healthy and faulty conditions in the machine. A three-phase induction motor rated at 7.5 kW, 50 Hz, and 400 V was used for the simulation study. The bearing considered was a 6208-2Z/C3 type with 9 rolling elements, a

rolling-element diameter of 12 mm, a pitch diameter of 58 mm, and a contact angle of 0°. The motor was operated at a rotor speed of 1460 rpm. These motor and bearing parameters were kept constant for the healthy and faulty operating conditions. The bearing geometric parameters and rotor speed were used to determine the characteristic frequencies associated with the different bearing fault conditions.

Under healthy conditions, the machine was configured to showcase the electromagnetic behavior of the machine, which serves as the baseline for the further faulted conditions analysis. Bearing faults were simulated by introducing periodic modulation of the mutual inductance Lm(t) in the machine's dynamic model. This model represented the physical effect of radial airgap eccentricity caused by bearing defects. The mutual inductance is expressed as

$$Lm(t) = Lmo\ (\ 1 + 2\ h1\ \cos(2\pi fct) + 2h2(4\ \pi fct) + \dots\ )$$

where h1, h2 represent harmonic amplitudes proportional to fault severity, and fc is the characteristic fault frequency (Zhang et al. 2020).

Signal Processing and Sub-band Extraction

The simulated stator current signals were sampled at 20 kHz for 6 s. To avoid the transient portion of the simulation, the initial 1 s of the signal was discarded, and the remaining steady-state signal was used for analysis. Fast Fourier Transform (FFT) was then applied to convert the stator current from the time domain to the frequency domain. The fundamental supply-frequency component was removed to emphasize the frequency components associated with bearing faults.

135 datasets of stator current were extracted from MATLAB, where 110 datasets were used to train the ML, 25 datasets for validation, and 5 datasets were used for testing the ML.

For each bearing fault condition, the characteristic fault frequency was calculated from the bearing geometry and rotor speed. The corresponding frequency components and their sidebands were then identified in the current spectrum. The fault-related components were extracted within predefined frequency sub-bands and used as the input representation for the CNN model. The bearing-related frequency components were expressed as

|

where (Fs) is the supply frequency, (Fc) is the characteristic bearing fault frequency, and (m) represents the harmonic order. This processing converts the raw stator current into a frequency-domain representation in which the changes caused by different bearing faults can be identified and used for fault classification and severity estimation.

PIML Architecture

The features extracted from the frequency domain analysis of stator current were fed to the machine learning feature extractor. Here, 1 dimension CNN filters can learn local patterns, such as groups of sidebands, spectral peaks, and changes in spectral location. The classification head of the ML model predicted the condition of the machine in binary, either healthy or faulty. The regression head estimated the fault severity as a continuous value, expressed as a percentage when the training labels are defined in percentage units. The regression output was constrained to a physically meaningful range such as 0–100%. Physics components utilized the bearing dimension and rotor speed to provide the analytical reference. The implementation summarized the relative spectral energy or prominence near theoretically predicted sidebands and transformed this quantity into a bounded physics-reference severity score.

The 1D CNN was implemented and trained in Python using the PyTorch framework. The extracted frequency-domain features were used as inputs to the CNN for fault classification and severity estimation. The network parameters were optimized using the Adam optimizer by minimizing the combined data-driven and physics-informed loss function. The trained model was subsequently evaluated using an independent test set.

Physics-Informed Loss and Optimization

Now, the loss function was used to compare the results of physics-driven analysis and machine learning results. The loss function needed to be minimized to generate accurate results. The loss function here was customized based on the ML results and analytical method results. Physics reference was derived from normalized FFT spectral evidence around the analytically calculated bearing characteristic frequencies (FTF, BPFO, BPFI, and BSF) and their sidebands, then converted into a bounded physics-reference severity score.

$L_{total} = L_{data} + \lambda L_{physics}$.

$L_{physics} = (Sp - Sc)^2$,

where Sp is the CNN-predicted severity, and Sc is the physics reference.

Results

Preliminary Analysis

As a preliminary analysis, the simulated stator-current signals were examined in both the time and frequency domains to verify the presence of distinguishable characteristics associated with the bearing conditions. The three-phase stator currents were first observed in the time domain, where the waveform characteristics of the healthy and faulty conditions were compared. The corresponding frequency-domain representations were obtained using FFT analysis after removing the 50 Hz fundamental component. The frequency-domain analysis was particularly used to examine the spectral components associated with the characteristic bearing frequencies.

The time-domain signals provide an initial view of the current waveform variation under different bearing conditions, while the frequency-domain spectra provide more direct information about the frequency components associated with bearing faults. The observed spectral characteristics were subsequently used as the basis for the sub-band spectral representation supplied to the proposed 1D CNN.

Figure 2

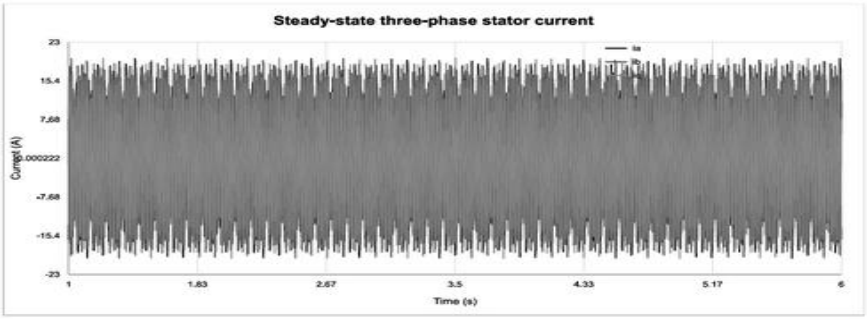


Figure 2
Time-domain plot of stator current for a 30% change in Lm that represents a cage fault

Figure 3

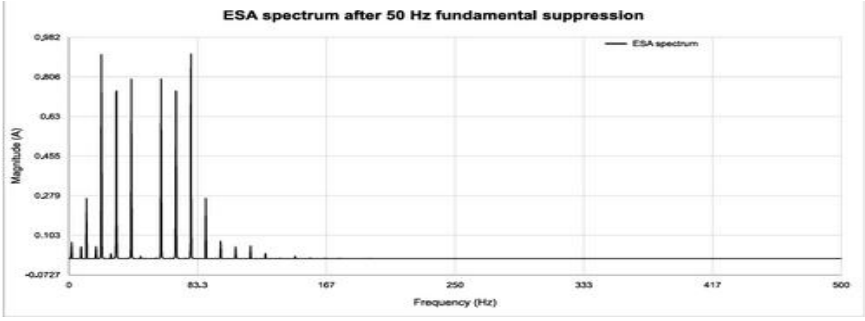


Figure 3

Frequency domain plot of stator current for a 30% change in Lm that represents a cage fault

These preliminary results demonstrate that the electrical current signals contain condition-dependent information that can be further processed for bearing-fault classification.

Classification Performance

The physics-informed machine learning framework was evaluated using an independent test set containing five signals, comprising one healthy signal and one signal from each of the four bearing-fault classes: cage, outer-race, inner-race, and ball faults. The model correctly classified all five test signals. The overall accuracy, macro-precision, macro-recall, and macro-F1 score were all 1.0.

Figure 4

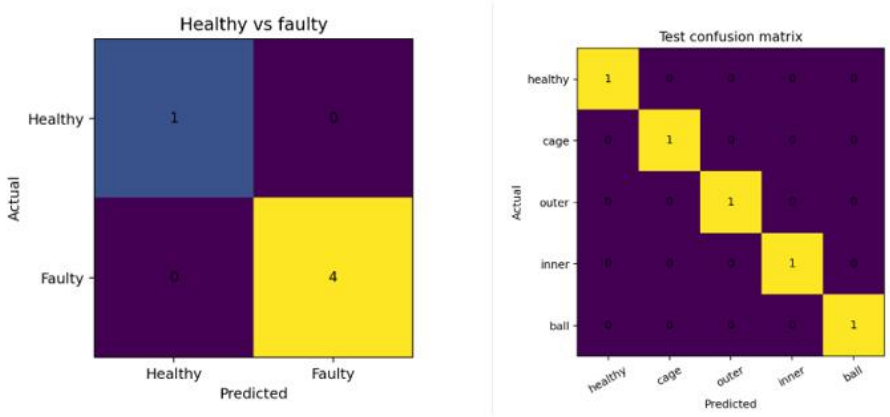


Figure 4

Test confusion matrix showing the classification of independent test signals

The results show that the model distinguished the healthy condition from the faulty conditions and correctly identified the four individual bearing-fault classes in the independent test set. Both healthy and faulty recall were 1.000, while the faulty-condition F1 score was also 1.000.

Severity Quantification

The model also provided severity estimates for the tested conditions. For the four faulty signals, the actual severity was 9%, while the predicted severities were 7.17% for the outer-race fault,

6.07% for the cage fault, 6.74% for the inner-race fault, and 5.43% for the ball fault. For the healthy signal, the actual severity was 0%, with a predicted value of 1.20%.

Figure 5

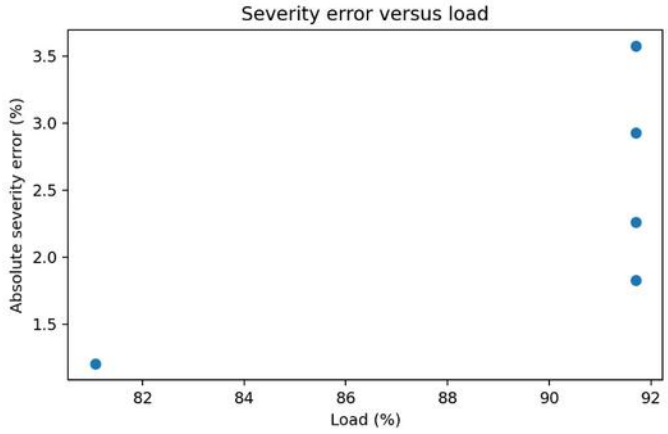


Figure 5
Absolute severity error for 5 different cases

The resulting severity mean absolute error (MAE) was 2.358%, while the root mean square error (RMSE) was 2.499 percentage points. These results indicate that the model provided severity estimates with relatively small deviations from the corresponding reference values in the available test set.

The proposed framework correctly classified all five signals in the independent test set. However, because the test set contains only one sample per class, these results should be interpreted as preliminary evidence of feasibility rather than conclusive evidence of generalization.

Discussion

The signal analysis shows that stator-current responses contain condition-dependent information in both the time and frequency domains. The frequency-domain representation is more suitable for bearing-fault analysis because fault-related spectral components can be examined around the characteristic frequencies determined by bearing geometry and shaft speed. Removing the 50 Hz fundamental further reduces the dominance of the supply component and improves the visibility of fault-related spectral information.

The proposed physics-informed 1D CNN correctly classified all five signals in the independent test set, achieving an accuracy and macro-F1 score of 1.000. The model also provided quantitative severity estimates, with an MAE of 2.358% and an RMSE of 2.499 percentage points. The difference between predicted and reference severities indicates that fault classification and severity estimation remain distinct tasks. Overall, the results support the feasibility of integrating electrical spectral information with bearing-related physical constraints for the investigated conditions.

Limitation

The independent test set contains only five signals, with one sample representing each class. Therefore, the classification results cannot be considered sufficient evidence of generalization to larger datasets. The evaluation also covers a limited range of operating conditions and does not establish performance across different speeds, loads, bearing geometries, or fault severities. Further evaluation using larger datasets with multiple severity levels and wider operating conditions is required to assess the robustness and generalization of the framework.

Conclusion

This study presented a physics-informed machine learning framework for bearing-fault detection and severity estimation in an induction machine using electrical signature analysis. FFT-based stator-current spectral information was used as the input representation for a 1D CNN, while bearing-related physical information was incorporated through a physics-informed loss formulation. The proposed framework demonstrated its ability to identify different bearing conditions and provide quantitative severity estimates under the investigated test conditions. The study therefore indicates the potential of combining electrical signal analysis, deep learning, and physical bearing characteristics for bearing-fault diagnosis. Further validation with larger and more diverse datasets is necessary to establish the robustness and generalization of the framework.

Funding

This research was supported by Tribhuvan University, Institute of Engineering, for research purposes.

Conflict of Interest

The authors declare that they have no conflict of interest.

Author Contributions

Nikil Gautam: Methodology, software, data analysis, and manuscript preparation.

Dr. Bishal Silwal: Supervision, guidance, and manuscript review.

Data Availability

The data generated and used in this study are available from the author upon reasonable request. For data access, you can contact the author at 080mspse013.nikil@pcampus.edu.np.

References

Ajit, A., Acharya, K., & Samanta, A. (2020). A review of convolutional neural networks. In *2020 International Conference on Emerging Trends in Information Technology and Engineering (ic-ETITE)* (pp. 1–5). IEEE. https://doi.org/10.1109/ic-ETITE47903.2020.049

Ji, D.-Y., Wang, B., Inoue, H., & Kanemaru, M. (2025). Motor fault detection with a hybrid physics-based and data-driven method. In *2025 IEEE International Electric Machines & Drives Conference (IEMDC)* (pp. 1178–1183). IEEE. https://doi.org/10.1109/IEMDC60492.2025.11061000

Shen, Z., Zhang, S., Wang, B., & Habetler, T. G. (2020). Deep learning algorithms for bearing fault diagnostics—A comprehensive review. *IEEE Access, 8*, 29857–29881. https://doi.org/10.1109/ACCESS.2020.2972859

Shen, S., et al. (2021). *A physics-informed deep learning approach for bearing fault detection*. Engineering Applications of Artificial Intelligence, 103, 104295.

Vehviläinen, M., Tahkola, M., Keränen, J., El Bouharrouti, N., Rahkola, P., Halme, J., Pippuri-Mäkeläinen, J., & Belahcen, A. (2024). 3D multibody simulation of realistic rolling bearing defects for fault classifier development. In *2024 International Conference on Electrical Machines (ICEM)*. IEEE. https://doi.org/10.1109/ICEM60801.2024.10700332

Vinothraj, C., Praveen Kumar, N., & Isha, T. B. (2018). Bearing fault analysis in induction motor drives using the finite element method. *International Journal of Engineering & Technology, 7*(3.6), 30–34. https://doi.org/10.14419/ijet.v7i3.6.14928

Zhang, S., Wang, B., Kanemaru, M., Lin, C., Liu, D., & Habetler, T. G. (2020). Model-based analysis and quantification of bearing faults in induction machines. *IEEE Transactions on Industry Applications, 56*(3), 2158–2170. https://doi.org/10.1109/TIA.2020.2979383

Impact of Residential Electric Vehicle Charging on an Urban Distribution Feeder and Its Mitigation through Tariff-Based Demand Response: A Case Study of the New Road Feeder, Pokhara

Sandesh Belbase[1], Menaka Karki[1*]

[1]Department of Electrical Engineering, Pashchimanchal Campus, Institute of Engineering, Tribhuvan University
Pokhara, Nepal
sandeshbelbase2026@gmail.com
[*]Corresponding author: menaka@wrc.edu.np

Abstract

Rapid growth in residential electric vehicle (EV) ownership under Nepal's Third Nationally Determined Contribution (NDC 3.0) is expected to add a substantial, temporally concentrated load to distribution feeders designed for conventional demand alone. This study evaluates the impact of residential EV charging on the 11 kV New Road distribution feeder in Pokhara and the extent to which tariff-based demand response can mitigate it. Conventional load was forecast using linear regression, and EV ownership was projected using a policy-constrained logistic adoption model combined with a stock–flow relationship. A Monte Carlo model of individual EV travel and charging behaviour, developed in Python, generated representative 24-hour fleet charging profiles for 2025–2045. Uncontrolled charging, Time-of-Use (ToU) pricing, and dynamic pricing were evaluated through time-series load flow in OpenDSS to assess bus voltage, line loading, and transformer loading. By 2045, the minimum feeder voltage falls to 0.8423 p.u. under uncontrolled charging and improves only to 0.8427 p.u. and 0.8472 p.u. under ToU and dynamic pricing, respectively, all below the 0.95 p.u. limit. Maximum line loading reaches 164.56%, 162.17%, and 157.62%, and the most critical transformer reaches 188.51%, 188.04%, and 182.68% under uncontrolled, ToU, and dynamic pricing, respectively. Dynamic pricing consistently outperforms the other strategies, but neither tariff keeps the network within its rated thermal limits beyond 2030. Tariff-based demand response is therefore a useful but partial solution, and network reinforcement or distributed support measures will be required to accommodate the projected EV penetration.

Keywords: electric vehicle charging, distribution network, Monte Carlo simulation, OpenDSS, tariff-based demand response

Introduction

Road transport remains one of the largest contributors to energy-related carbon dioxide emissions, and electrification of the vehicle fleet is widely regarded as one of the most effective near-term measures for reducing this footprint (International Energy Agency [IEA], 2024). Global EV sales have risen sharply in recent years; electric cars accounted for close to one in five new car sales in 2023, a more than six-fold increase over five years (IEA, 2024). Nepal, which has announced a net-zero target for 2045, has similarly committed to an ambitious electrification pathway: under its NDC 3.0, submitted to the United Nations Framework Convention on Climate Change (UNFCCC) in 2025, battery electric vehicles are targeted to reach 90% of new private passenger vehicle sales by 2030 and 95% by 2035 (Ministry of Forests and Environment [MoFE], 2025). Consistent with this policy direction, EV imports have grown

rapidly, from a few hundred units in fiscal year 2020/21 to more than 11,000 four-wheelers in 2023/24 (Kafle, 2024).

This pace of adoption, while beneficial from a climate perspective, places new and largely unplanned stress on the low- and medium-voltage distribution networks that will supply the resulting charging load. Because most private EVs in Nepal are expected to be charged at home, the additional demand tends to coincide with the existing residential evening peak, a pattern that can produce voltage drops, accelerated conductor and transformer ageing, and reduced hosting capacity if left unmanaged (Rahman et al., 2022). Distribution feeders in urban and semi-urban Nepal are frequently radial, have high resistance-to-reactance (R/X) ratios, and were sized for historical rather than future demand, making them particularly susceptible to these effects.

Although previous studies have established the feasibility of Monte Carlo-based EV fleet modelling and tariff-based mitigation, relatively few have combined multi-decade EV adoption forecasting under an explicit national policy target with a full 24-hour time-series comparison of charging strategies on an actual, data-verified Nepali distribution feeder. The objective of this paper is to address that gap by developing an integrated forecasting–simulation framework for the 11 kV New Road feeder in Pokhara and using it to (a) project residential EV charging demand for 2025–2045 under Nepal's NDC 3.0 scenario, (b) evaluate the resulting bus voltage, line loading, and transformer loading under uncontrolled charging, and (c) quantify the extent to which ToU and dynamic pricing can mitigate the identified network impacts.

Literature Review

A number of studies have examined the network-level consequences of EV charging using stochastic and simulation-based approaches. Kongjeen and Bhumkittipich (2018) analysed the influence of plug-in EVs on static voltage stability using a voltage-dependent load-flow method on the IEEE 33-bus system and found that the effect of EV loading became significant mainly at higher penetration levels. Bhandari et al. (2021) modelled the Bageshwori feeder in DIgSILENT and used Monte Carlo simulation in Python to aggregate individual EV charging profiles, reporting line loading in excess of 100% at high penetration even though voltages remained within acceptable limits. Abid et al. (2021) applied a probabilistic load-flow approach to a residential feeder in Dhaka to identify the EV penetration level beyond which voltage security could not be maintained.

On the mitigation side, Dubey and Santoso (2015) reviewed the impacts of residential EV charging on distribution circuits in North America and highlighted the importance of combining system-level analysis with mitigation strategies such as time-differentiated tariffs. A field evaluation of ToU pricing for EV customers found that most participants shifted charging to off-peak hours in response to price signals, confirming the practical viability of tariff-based load shifting (Cook et al., 2014).

Taken together, these studies differ in scope and in the questions they answer. Analyses on standard test systems such as the IEEE 33-bus network (Kongjeen & Bhumkittipich, 2018) provide general insight but do not capture the topology and loading of a specific feeder, whereas the feeder-specific studies (Abid et al., 2021; Bhandari et al., 2021) focus primarily on quantifying the impact of EV charging. Conversely, the evidence on tariff-based demand response (Cook et al., 2014) concerns customer charging behaviour and does not directly quantify the resulting relief on distribution assets. The present study builds on these approaches

by linking a policy-constrained, multi-decade EV adoption forecast with Monte Carlo fleet modelling and a 24-hour time-series comparison of uncontrolled charging, ToU pricing, and dynamic pricing on a real Nepali feeder.

Materials and Methods

The overall methodology, summarised in Figure 1, integrates conventional load forecasting, EV population and charging-demand forecasting, probabilistic fleet modelling, and time-series distribution load-flow analysis. Feeder and transformer data were obtained from the Nepal Electricity Authority (NEA), Pokhara Distribution and Consumer Service, and the feeder was modelled in OpenDSS, an open-source distribution-system solver developed by the Electric Power Research Institute (EPRI) that supports unbalanced, time-series analysis of radial networks with a high R/X ratio (EPRI, n.d.). Conventional and EV loads were forecast independently for the study years 2025, 2030, 2035, 2040, and 2045, combined into hourly feeder-load profiles under three charging conditions, and evaluated through time-series load flow to obtain bus voltage, line loading, and transformer loading.

Figure 1

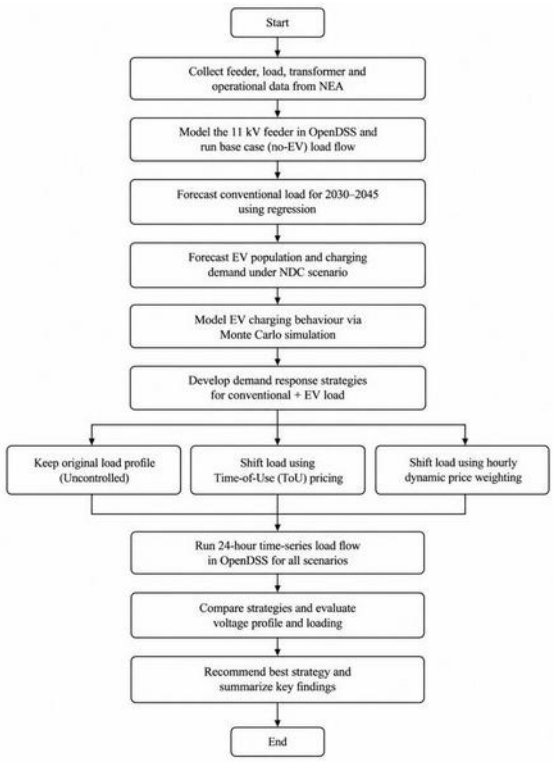


Figure 1
Overall Methodology Adopted for the Study

Study Feeder

The 11 kV New Road feeder originates from the 132/11 kV Kudahar Grid Substation and supplies part of Pokhara Metropolitan City Wards 8–11, serving approximately 4,200 consumers with a recorded peak demand of 4,040 kW and 2,390 kVAR. The feeder comprises 39 buses and 41 line sections, and its 42 distribution transformers range from 25 kVA to 630 kVA. A base

voltage of 11.0565 kV (1 p.u.) and a base power of 10 MVA were used throughout the OpenDSS model. The feeder layout, mapped using geographic information system (GIS) data, is shown in Figure 2.

Figure 2

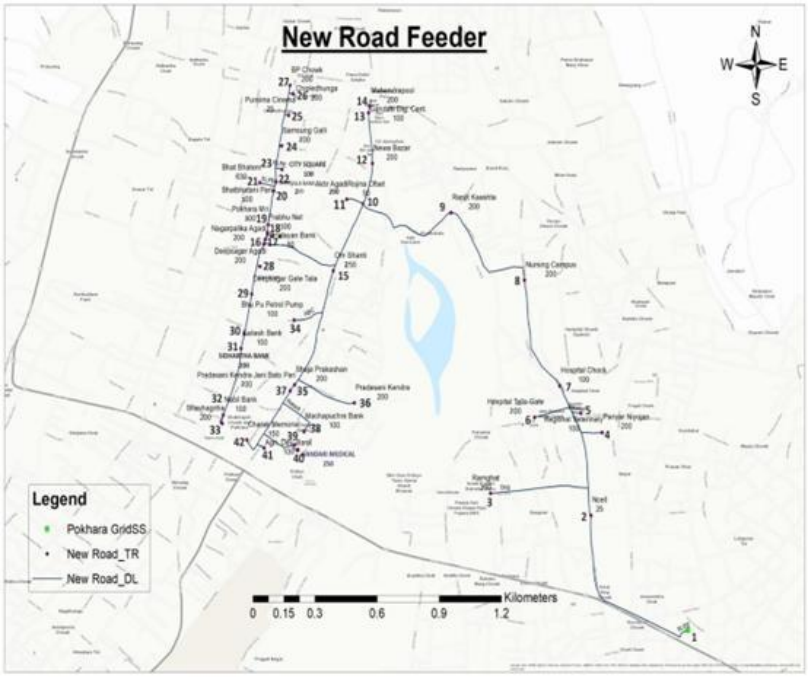


Figure 2
GIS Layout of the 11 kV New Road Feeder

Conventional Load Forecasting

Historical annual peak-load records for the study area were fitted with the linear regression model given in Equation 1:

(1)

where $\hat{P}_t$ is the forecast conventional load in year t, and β_0 and β_1 are the regression intercept and slope obtained by least-squares fitting to historical data. The fitted model was extrapolated to obtain the conventional demand for each study year, and the existing 24-hour load shape was scaled to this forecast level.

EV Population Forecast Under the NDC 3.0 Scenario

The EV share of total vehicle sales was modelled with the logistic (S-curve) diffusion function given in Equation 2:

(2)

where S_{max} is the saturation sales share, k is the growth rate, and t_0 is the inflection year. The function was calibrated so that the projected EV sales share reached the NDC 3.0 milestones of 90% by 2030 and 95% by 2035, with saturation assumed thereafter. Annual EV sales were obtained by applying this share to the forecast vehicle-sales volume, and the resulting sales were accumulated into EV stock using a simplified stock–flow relationship that neglects vehicle

retirement over the planning horizon, since feeder-level retirement data were not available and the focus of the study is network impact rather than fleet survival. The resulting EV population is summarised in Table 1.

Table 1

Projected EV Population Under the NDC 3.0 Scenario

Study year	2022	2025	2030	2035	2040	2045
No. of EVs	26	174	440	666	814	905

Note. EV = electric vehicle; NDC 3.0 = Nepal's Third Nationally Determined Contribution.

Probabilistic EV Charging Model

A representative residential EV, the BYD Dolphin, with a 40.5 kWh battery, a specific energy consumption of 0.09 kWh/km, and a 3.3 kW, 88%-efficient alternating-current home charger, was modelled in Python. For each vehicle i, the daily travel distance D_i and the initial state of charge $SOC_{i,0}$ were drawn from normal distributions, $D_i \sim N(35, 4^2)$ km and $SOC_{i,0} \sim N(70, 10^2)$ %, while the plug-in time was drawn from $T_{plug,i} \sim N(19{:}00\text{ h}, 3.3^2\text{ h})$, reflecting typical evening return patterns. The state of charge (SOC) on arrival was obtained after subtracting the travel-related energy consumption, bounded between the minimum and maximum allowable SOC of 20% and 100%, and the corresponding charging energy and duration were computed from the charger rating and efficiency and discretised into 15-minute intervals.

Monte Carlo Fleet Aggregation

Because the charging behaviour of a single EV cannot represent aggregate feeder-level demand, the individual profiles of the full projected EV fleet for each study year were aggregated using Monte Carlo simulation (MCS). Each of 20 independent realisations sampled a complete set of stochastic EV parameters and produced one possible 24-hour fleet charging profile; the representative profile was then obtained as the average given in Equation 3:

(3)

where N_{MC} is the number of Monte Carlo realisations, taken as 20 in this study, and $P_{fleet,j}(t)$ is the fleet charging profile obtained from the jth realisation.

Tariff-Based Demand Response Strategies

Two demand response strategies were evaluated in addition to uncontrolled charging, in which the raw simulated profile is applied without modification. Under ToU pricing, NEA's two-tier low-voltage tariff was applied (NRs. 7.25/kWh from 17:00 to 22:00 and NRs. 5.75/kWh for the remaining hours), and 30% of the demand occurring during the peak window, for both conventional and EV load, was treated as responsive and redistributed equally across the off-peak hours, conserving total daily energy.

Under dynamic pricing, an hourly price signal was derived directly from the normalised conventional load shape, varying linearly between the same minimum and maximum tariff values, so that the peak hours were determined by the load profile itself rather than by a fixed schedule. As with ToU pricing, 30% of the peak-period demand was shifted, but the redistribution among off-peak hours followed an inverse-price weighting so that lower-priced hours absorbed proportionally more of the shifted load.

Load-Flow Simulation and Assessment Criteria

The resulting 24-hour profiles for all three strategies and all study years were incorporated into the OpenDSS feeder model, and time-series load-flow analysis was carried out to obtain hourly bus voltages, line loadings, and transformer loadings. A lower voltage limit of 0.95 p.u. and a thermal limit of 100% of rated ampacity or capacity were used as the assessment criteria.

Results

Voltage Profile

Table 2 summarises the minimum feeder voltage obtained over the 24-hour simulation for each study year and charging strategy (a graphical comparison is provided in Appendix A). Under uncontrolled charging, the minimum voltage falls steadily from 0.9176 p.u. in 2025 to 0.8423 p.u. in 2045, a reduction of about 0.075 p.u. Bus 27, the electrically farthest bus on the feeder, remains the critical bus in every case examined.

Table 2

Minimum Feeder Voltage Under the Three Charging Strategies

Study year	Uncontrolled (p.u.)	ToU (p.u.)	Dynamic (p.u.)
2025	0.9176	0.9177	0.9197
2030	0.8925	0.8927	0.8956
2035	0.8695	0.8699	0.8735
2040	0.8491	0.8494	0.8535
2045	0.8423	0.8427	0.8472

Note. p.u. = per unit; ToU = Time-of-Use pricing. Values are the lowest bus voltage recorded over the 24-hour simulation; the lower voltage limit is 0.95 p.u.

Dynamic pricing produces the highest minimum voltage in every study year, but the improvement over uncontrolled charging is modest, only about 0.005 p.u. in 2045. At the original uncontrolled critical hour (19:00) in 2045, ToU pricing raises the voltage from 0.842 p.u. to 0.883 p.u., an improvement of over 0.04 p.u.; however, its own 24-hour minimum shifts to 16:00. The critical hour under dynamic pricing similarly shifts to 22:00. Neither strategy keeps the worst-case feeder voltage above the 0.95 p.u. criterion in any study year.

Line Loading

The maximum line loading recorded across the 41 feeder sections increases from 83.7% in 2025 to 164.6% in 2045 under uncontrolled charging (Figure 3). Line L1, the section closest to the substation that carries the full downstream load, remains the most heavily loaded conductor throughout the study. Overloading first appears in 2030, when three lines exceed their rated ampacity under uncontrolled operation; this grows to seven lines by 2035 and to eight lines by 2040, a number that persists through 2045 under all three strategies.

Figure 3

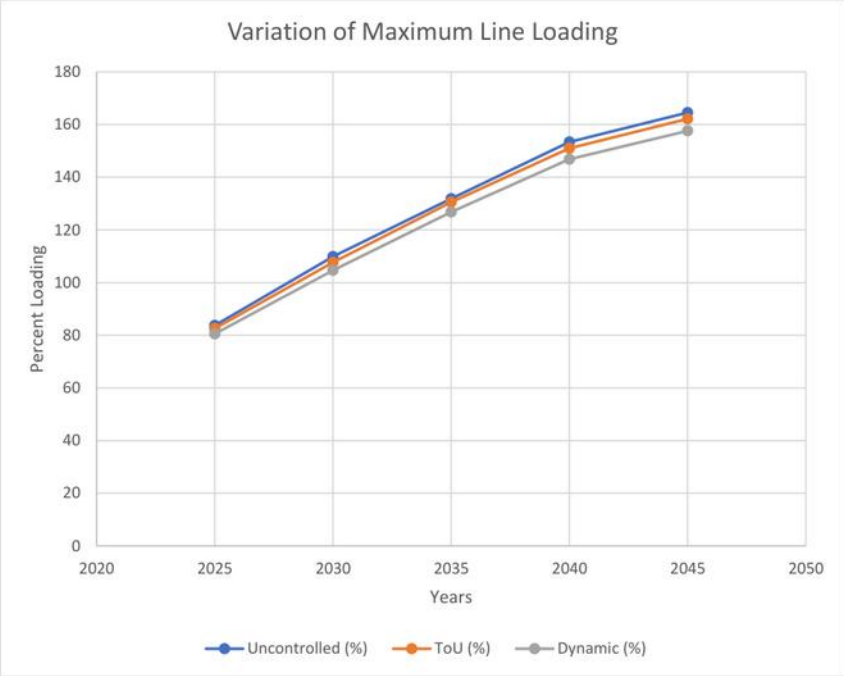


Figure 3
Maximum Line Loading Versus Study Year

Dynamic pricing consistently achieves the lowest maximum loading, reducing the 2045 value from 164.6% to 157.6% (a 4.9 percentage-point reduction), compared with a reduction of only 1.5 percentage points under ToU pricing. The 24-hour loading profile of the critical line L1 in 2045 is shown in Figure 4. Both tariff strategies relieve loading during the original uncontrolled peak at 13:00 by over 40 percentage points; however, ToU pricing produces a new maximum at 16:00 that is almost identical to the original peak, whereas dynamic pricing distributes the shifted demand more evenly and achieves a comparatively lower, though still severely overloaded, daily maximum.

Figure 4

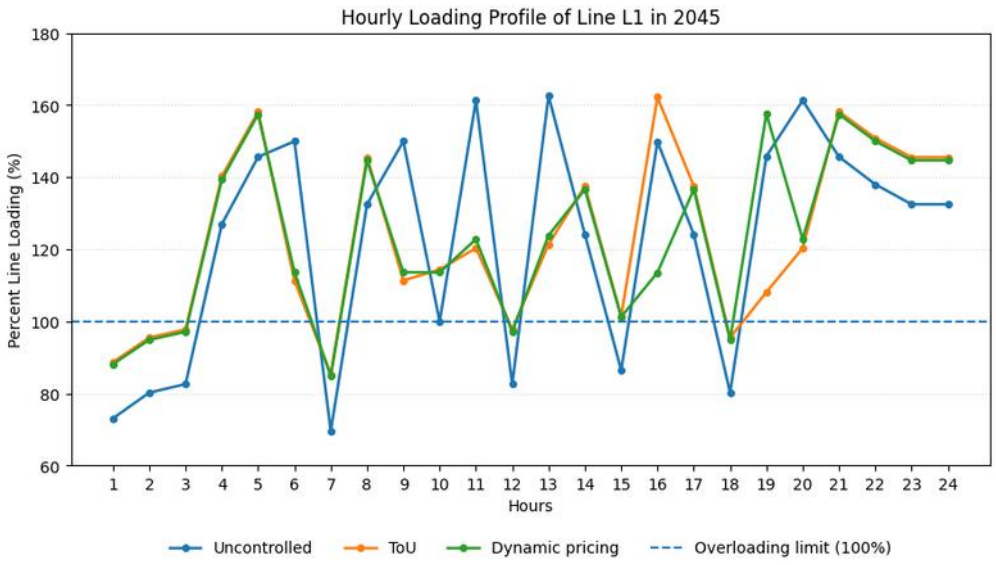


Figure 4
24-Hour Loading Profile of the Critical Line (L1) in 2045

Transformer Loading

Transformer loading follows a similar but more severe trend. The most heavily loaded unit, the Nursing transformer, reaches 97.6% loading in 2025 and 188.5% by 2045 under uncontrolled charging (Figure 5), and it remains the critical transformer regardless of charging strategy. The number of overloaded transformers on the feeder rises from zero in 2025 to 18 in 2030, 35 in 2035, and 39–40 of the 42 transformers by 2040–2045 under all three strategies.

Figure 5

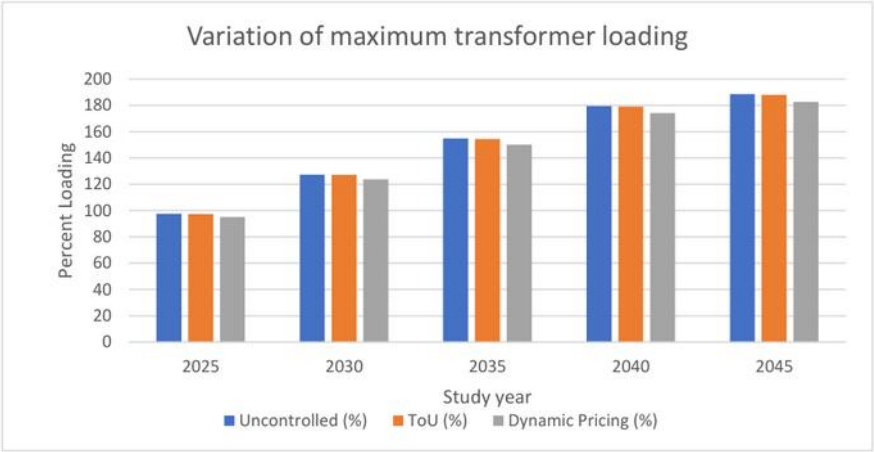


Figure 5
Maximum Transformer Loading Versus Study Year

The 24-hour loading profile of the Nursing transformer in 2045 (Figure 6) shows that the unit remains above its rated capacity for 17 of 24 hours under uncontrolled charging and for 23 of 24 hours under both ToU and dynamic pricing. Dynamic pricing achieves the largest reduction in the maximum value, 5.8 percentage points relative to uncontrolled charging in 2045 compared

with 0.5 percentage points for ToU pricing, against an increase of roughly 91 percentage points in maximum loading between 2025 and 2045.

Figure 6

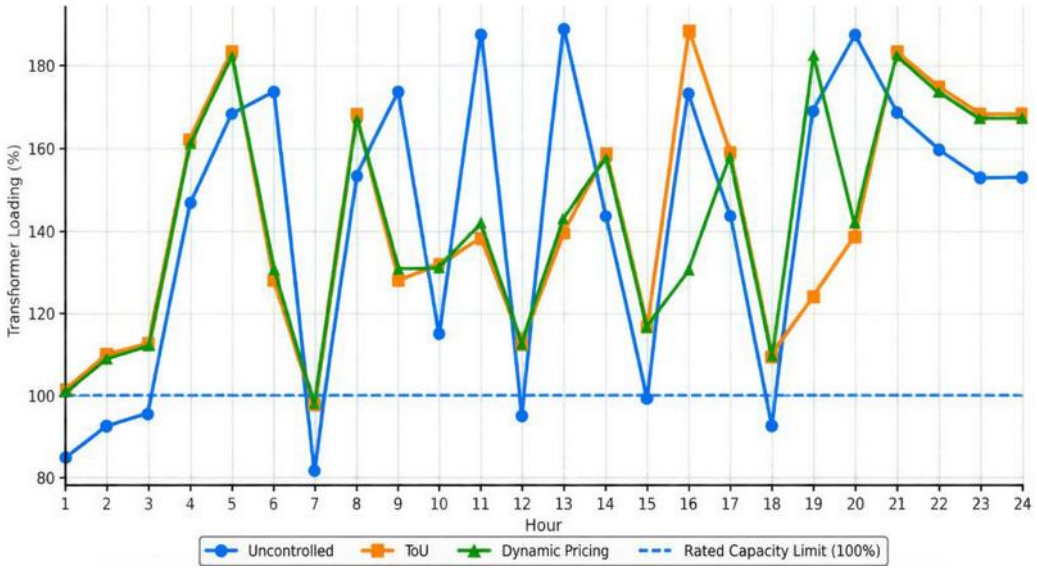


Figure 6
24-Hour Loading Profile of the Critical (Nursing) Transformer in 2045

Discussion

Across all three network indicators, the results show a consistent pattern: dynamic pricing outperforms ToU pricing, and both outperform uncontrolled charging, but the magnitude of improvement is small relative to the scale of demand growth projected under Nepal's NDC 3.0 EV adoption pathway. The persistence of Bus 27 as the critical bus under every strategy indicates that the weak point of the network is governed by feeder topology rather than by the charging strategy in use. Notably, the minimum voltage is already below 0.95 p.u. in 2025, which suggests that the feeder has limited voltage headroom even before large-scale EV adoption.

The limited benefit of the tariff strategies follows from their mechanism. Because both strategies redistribute rather than reduce total energy, they relieve the original peak period at the cost of creating a secondary, less severe but still significant, stressed period elsewhere in the day. This was evident in the shift of the critical hour from 19:00 to 16:00 under ToU pricing and to 22:00 under dynamic pricing, and in the extension of transformer overloading from 17 to 23 hours per day. Cook et al. (2014) showed that EV customers do respond to ToU price signals; the present results indicate that, at the feeder level, a fixed peak window can simply relocate the stress to the shoulder hours when a large share of demand responds. A load-following price signal, as in the dynamic pricing case, spreads the shifted demand more evenly, which explains its consistently better performance. These findings underline the importance of evaluating demand response over a complete 24-hour cycle rather than at a single nominal peak hour.

The results are broadly consistent with earlier studies while extending them in two respects. Bhandari et al. (2021) reported line loading above 100% at high EV penetration while voltages remained acceptable; on the New Road feeder, both thermal and voltage limits are violated,

reflecting the combined effect of conventional load growth, policy-driven EV adoption, and the length of the feeder to Bus 27. In line with Kongjeen and Bhumkittipich (2018), who found that EV impacts became significant mainly at higher penetration, thermal violations in this study emerge from 2030 onwards and escalate as the projected fleet grows from 440 to 905 vehicles. Thermal overloading also becomes a feeder-wide constraint rather than an isolated single-line problem well before the end of the planning horizon, and transformer capacity emerges as the most widespread constraint, affecting nearly all units by 2045.

In practical terms, and consistent with the recommendation of Dubey and Santoso (2015) to pair impact assessment with mitigation, tariff-based demand response is best viewed as a first-stage measure. Once several sections and most transformers are simultaneously near or above their rated capacity, load shifting alone cannot compensate for the underlying growth in demand. The New Road feeder is therefore likely to require network reinforcement, distributed generation, battery energy storage, or reactive power support, particularly around Bus 27 and the Nursing transformer, to accommodate the projected EV penetration beyond approximately 2030.

Limitations

Several limitations should be considered when interpreting these findings. First, the EV fleet was represented by a single vehicle model (BYD Dolphin) and a single 3.3 kW home charger, and only residential home charging was considered; a more diverse fleet, higher-rated chargers, or public and fast charging could alter both the magnitude and timing of the charging load. Second, travel distance, initial SOC, and plug-in time were represented by normal distributions with fixed parameters, and the fleet profile was averaged over 20 Monte Carlo realisations, so the results represent an expected rather than a worst-case daily profile.

Third, conventional load was forecast with a linear regression model, and EV stock was estimated using a stock–flow relationship that neglects vehicle retirement and assumes that the NDC 3.0 targets are met; slower adoption or different load growth would change the timing of the identified violations. Fourth, the demand response strategies assumed a fixed 30% responsive share of peak-period demand and the current NEA tariff levels throughout the planning horizon. Finally, the study examined a single feeder under its existing configuration without reinforcement, so the quantitative results are specific to the New Road feeder, although the methodology is transferable to other feeders.

Conclusion

This paper presented an integrated forecasting and simulation framework to evaluate the impact of residential EV charging on the 11 kV New Road distribution feeder in Pokhara under Nepal’s NDC 3.0 adoption pathway, and to assess the effectiveness of ToU and dynamic pricing as mitigation measures. Uncontrolled EV charging, superimposed on forecast conventional load growth, lowers the minimum feeder voltage from 0.9176 p.u. in 2025 to 0.8423 p.u. in 2045 and pushes conductor and transformer loading beyond rated capacity from 2030 onwards, with transformer overloading becoming an almost feeder-wide problem by 2045. Dynamic pricing consistently provides the greatest relief among the strategies tested, but neither it nor ToU pricing keeps the feeder within its technical limits in the later study years, since load shifting relocates rather than removes network stress.

These findings support adopting tariff-based demand response as a first-stage mitigation measure, complemented in the longer term by targeted network reinforcement or distributed

energy resources at the identified critical locations. Future research could evaluate coordinated smart charging combined with battery energy storage or reactive power support, incorporate locally surveyed travel and charging data, and extend the analysis to other feeders in the Pokhara distribution network.

Acknowledgments

The authors gratefully acknowledge the Nepal Electricity Authority, Pokhara Distribution and Consumer Service, for providing the feeder, transformer, and load data used in this study, and the Department of Electrical Engineering, Pashchimanchal Campus, Institute of Engineering, Tribhuvan University, for institutional support.

Funding

The authors received no financial support for the research, authorship, or publication of this paper.

Conflict of Interest

The authors declare no conflict of interest.

Author Contributions

Sandesh Belbase: conceptualization, methodology, software, data curation, formal analysis, investigation, visualization, and writing – original draft. Menaka Karki: conceptualization, methodology validation, supervision and review.

Data Availability

The feeder, transformer, and load data were provided by the Nepal Electricity Authority and are not publicly available; they may be requested from the Nepal Electricity Authority, subject to its permission. The Python simulation code and OpenDSS model developed in this study are available from the corresponding author upon reasonable request.

References

Abid, M. S., Apon, H. J., Morshed, K. A., & Abid, F. (2021). Impact assessment of charging of electric vehicle on residential distribution network of Bangladesh. In *Proceedings of the 56th International Universities Power Engineering Conference (UPEC)* (pp. 1–6). IEEE.

Bhandari, G., Paudel, N., Maharjan, S., & Gurung, S. (2021). Impact assessment of plug-in electric vehicles on distribution system through home charging. In *Proceedings of the 10th IOE Graduate Conference*. Institute of Engineering, Tribhuvan University.

Cook, J., Churchwell, C., & George, S. (2014). *Final evaluation for San Diego Gas & Electric's plug-in electric vehicle TOU pricing and technology study*. San Diego Gas & Electric.

Dubey, A., & Santoso, S. (2015). Electric vehicle charging on residential distribution systems: Impacts and mitigations. *IEEE Access*, *3*, 1871–1893. https://doi.org/10.1109/ACCESS.2015.2476996

Electric Power Research Institute. (n.d.). *OpenDSS* [Computer software]. https://www.epri.com/pages/sa/opendss

International Energy Agency. (2024). *Global EV outlook 2024*. IEA.

Kafle, L. (2024). Nepal's EV journey for cost and clean air mileage. *The Rising Nepal*.

Kongjeen, Y., & Bhumkittipich, K. (2018). Impact of plug-in electric vehicles integrated into power distribution system based on voltage-dependent power flow analysis. *Energies*, *11*(6), Article 1571. https://doi.org/10.3390/en11061571

Ministry of Forests and Environment. (2025). *Nepal's third nationally determined contribution (NDC 3.0)*. Government of Nepal.

Rahman, S., Khan, I. A., Khan, A. A., Mallik, A., & Nadeem, M. F. (2022). Comprehensive review and impact analysis of integrating projected electric vehicle charging load to the existing low voltage distribution system. *Renewable and Sustainable Energy Reviews*, *153*, Article 111756. https://doi.org/10.1016/j.rser.2021.111756

Appendix A

Figure A1 presents the minimum feeder voltage values reported in Table 2 in graphical form, to aid visual comparison of the three charging strategies across the study years.

Figure A1

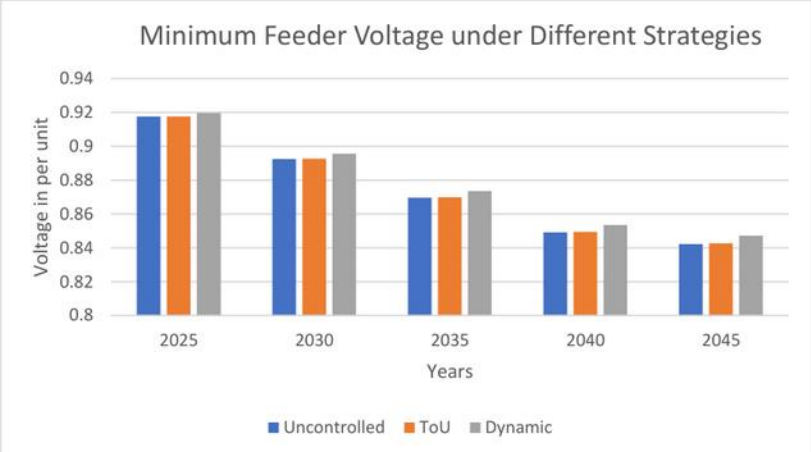


Figure A1
Minimum Feeder Voltage Across Study Years and Charging Strategies

Preliminary Thermal Performance and Condensation-Risk Screening of a 75 mm EPS Roof Insulation Retrofit for a Top-Floor RCC Residence in Kathmandu

Sandesh Adhikari[1], Sanjaya Neupane[2*]

[1]Department of Architecture, Institute of Engineering, Tribhuvan University
Pulchowk Campus, Nepal
079mseeb015.sandesh@pcampus.edu.np
[*]sanjaya@pcampus.edu.np

Abstract

Flat reinforced cement concrete (RCC) roofs in Kathmandu are commonly uninsulated, but limited studies have examined both the thermal benefits and moisture risks of adding insulation. This study evaluates a 75 mm expanded polystyrene (EPS) overlay on the 25.64 m² uninsulated roof of a top-floor residence. Thermal transmittance, January steady-state heat flow and room-side surface temperature were calculated following ISO 6946, while condensation risk was assessed using the ISO 13788 Glaser method under January typical-year and monsoon conditions. The January analysis used an outdoor temperature of 9.91 °C and 73.7% relative humidity (RH), with an assumed indoor condition of 20.0 °C and 54.9% RH. Monsoon conditions were based on a 15-day monitoring campaign in two bedrooms. The EPS overlay reduced the U-value from 3.70 to 0.41 W/m²K, representing an 88.8% reduction, and lowered January conductive heat flow from approximately 956 W to 107 W. The room-side surface temperature increased from 16.3 to 19.6 °C. No surface or interstitial condensation was indicated for the simplified assembly under either condition. However, the existing roof reached a surface RH of 80.3% in January, near the mould-risk limit, compared with 58.4% after retrofit. A vapour-tight layer at the outer face of the EPS indicated potential condensation. The results suggest that EPS insulation can substantially reduce roof heat loss, although a 12-month moisture assessment of the complete roof build-up is needed for a more comprehensive evaluation.

Keywords: roof insulation retrofit, expanded polystyrene, U-value, condensation risk

Introduction

The exposure data based on the 2011 census used by Chaulagain et al. (2016) shows that reinforced concrete frame buildings made up around 39–40% of the buildings in Kathmandu, Lalitpur and Bhaktapur. Field monitoring of one building in Dhulikhel and another in Biratnagar also found that the building in Dhulikhel experienced under-heating for more than four months in a year, which means winter thermal conditions also need to be considered in Nepal, along with overheating during summer (Chaulagain et al., 2019). Kulkarni et al. (2024) mention that the roof can be responsible for around 50–60% of the heat gained on the top floor of a building. In the household considered in this study, portable electric heaters are used from December to February, so heat loss through the roof during winter is also a concern, together with heat gain in summer. The NBC 206:2024 document that was consulted does not specify a mandatory U-value, R-value or insulation thickness for roofs of dwellings (Department of Urban Development and Building Construction [DUDBC], 2024), and the municipal bylaws have not been reviewed in this study.

When insulation is added to a roof, the temperature and vapour-pressure distribution within the roof changes, so achieving better thermal performance does not necessarily mean that the risk of condensation is acceptable. ISO 13788 provides simplified methods that can be used to screen for this risk (International Organization for Standardization [ISO], 2012). In this study, we aim to address two gaps identified in the literature reviewed. First, there appears to be limited evidence on roof insulation for the flat RCC roofs that are commonly found in the Kathmandu Valley, as discussed in the next section. Second, the thermal benefits of roof insulation are not often assessed together with a moisture-risk screening of the same roof assembly.

In our proposed model, we examine the effect of adding a fixed 75 mm EPS layer over an existing uninsulated RCC roof in Kathmandu. We aim to calculate the U-value and steady-state heat flow through both the existing roof and the insulated roof for January, and then calculate the roof surface temperature on the room side for the same month. We also screen both roof configurations for surface condensation, surface humidity related to mould risk, and interstitial condensation, and include a bounding check to consider the possible effect of vapour-resistant layers that are not included in the main calculation. The 75 mm insulation thickness is selected as a fixed case for the analysis, so it should not be understood as an optimised thickness. The study provides a documented screening calculation for an actual roof, using boundary conditions that are partly measured on site, while also explaining the limits of what can be established through this type of calculation.

Literature Review / Related Work

Most of the roof-related studies from climates similar to Kathmandu focus on reflective surface treatments, which reduce solar heat absorption but do not add any thermal resistance to the roof itself (Kulkarni et al., 2024). For insulated concrete roofs, Meddage et al. (2022) used both field experiments and simulations to study EPS-based lightweight concrete roof panels in a tropical climate, but their 75 mm system is different from placing an EPS board layer over an existing roof. Raimundo et al. (2023) also found that the most suitable EPS thickness depends on the building use, climate and what we want to achieve, such as reducing energy use, environmental impact or cost, so the results from other countries cannot be directly used for Kathmandu without considering the local conditions.

In Nepal, Subedi et al. (2026) simulated a residential building in the Kathmandu Valley and studied different wall, window and door constructions, while the floor and roof were kept as typical concrete structures. Thapa et al. (2020) studied the heating and cooling load demand of a residential building in the Valley under climate change conditions. Roof insulation has also been simulated for individual houses in Ghorepani and Dhulikhel in a master’s thesis by Borgkvist (2016). For practical information about insulation materials and overdeck roof systems, the BEEN Project manuals provide some useful guidance (BEEN Project, 2024, 2026).

ISO 13788 provides simplified calculation methods for assessing moisture-related risks, where moisture transport is assumed to happen through vapour diffusion only and monthly climate data is used for the calculations (ISO, 2012, Introduction). The method for interstitial condensation is one-dimensional and assumes steady-state conditions, and it does not consider changes in material properties due to moisture content, capillary suction or liquid moisture movement, air movement into the building component, or the ability of materials to store moisture through hygroscopic behaviour. Because of these limitations, the method is suitable only when these effects can be considered negligible (ISO, 2012, Clauses 1 and 6.2). The standard also explains

that this method is mainly intended for comparing different constructions, and it should not be treated as an accurate prediction of the actual moisture conditions during building use (Clause 6.1). It further states that the results become less reliable for structures with high thermal and moisture capacity (Introduction). Moisture design needs to consider all relevant hygrothermal loads (Künzel & Dewsbury, 2022), so in our study we use ISO 13788 as an initial screening method, and not as a way to predict the actual moisture performance of the roof. The properties of insulation materials can also change when moisture is present, because moisture increases the effective thermal conductivity of EPS (Khoukhi et al., 2019).

The literature reviewed for this study was not based on a systematic search, so the findings should be understood within that limitation. In the literature we reviewed, we did not identify a directly comparable study that combines measured conditions on the top floor with ISO 13788 condensation-risk screening for an EPS-insulated flat RCC roof in the Kathmandu Valley. For this reason, we examine the thermal performance and condensation risks associated with adding a fixed 75 mm EPS insulation layer to the roof of one top-floor RCC residence in Kathmandu.

Materials and Methods

Case-Study Building and Roof

The case study is a two and a half-storey RCC-frame house built in 2001 in Babarmahal, Kathmandu, at an elevation of about 1,330 m. In this study, we consider two occupied rooms on the top floor, which are located directly below a flat RCC roof. Room A is the primary bedroom with a plan area of 15.61 m², while Room B is the second bedroom with an area of 10.03 m², giving a total roof area of A = 25.64 m². The absolute heat flow through the roof depends on the roof area, but the percentage change in heat flow remains the same regardless of the area.

Kathmandu has a warm-summer humid subtropical to subtropical highland climate, where weather conditions are strongly influenced by the monsoon (World Bank Group, 2021). The TMYx weather file for Tribhuvan International Airport (WMO 444540, elevation 1,338 m; Lawrie & Crawley, 2022) gives a mean outdoor temperature of 9.91 °C and a relative humidity of 73.7% for January, and these values are used as the winter boundary conditions in our proposed model.

Existing and Proposed Roof Assemblies

The existing roof was surveyed in August 2026, and it consists of 12 mm cement-sand plaster, a 125 mm M20 RCC slab, and a 25 mm cement-sand screed with a damp-proofing additive. There is no thermal insulation in the roof, and no waterproofing membrane was observed above the screed during the survey. The exposed roof surface has some staining, moss and algae growth, and local areas where the screed has delaminated. For the retrofit case, we consider adding a 75 mm EPS board over the existing screed, as shown in Table 1. In the roof assembly assessed here, the EPS becomes the outermost layer and is directly exposed to outdoor conditions. For an actual installation, a weather-protective finish would be needed over the EPS, but this is not included in the present assessment.

The 75 mm thickness was selected for practical reasons, since EPS boards are available from suppliers in Nepal (Green Developers Nepal, n.d.) and they add relatively little dead load to the existing roof. The complete overdeck roof system described in the BEEN insulation manual also includes a waterproofing layer, mastic, geotextile, mesh-reinforced protective screed and a tile finish (BEEN Project, 2024). However, the available sources for this study do not provide the

thermal and vapour properties of these layers in tabulated form, so they have not been included in the assessed assembly, which makes the model a simplified version of the full roof system. The BEEN manual specifies rigid closed-cell boards made from polyurethane, polyisocyanurate or extruded polystyrene for its overdeck roof system. In our proposed model, EPS is retained because this is the insulation material being studied.

Table 1

Assessed Roof Assembly and Adopted Properties (Inside to Outside)

Layer	d (mm)	λ (W/m·K)	R (m²K/W)	μ (–)
Internal surface (R_{si}, upward flow)	n/a	n/a	0.100	n/a
Cement-sand plaster	12	0.721	0.017	12
RCC slab (M20)	125	1.580	0.079	80
Cement-sand screed (existing)	25	0.719	0.035	30
EPS board (retrofit only)	75	0.035 (0.029 to 0.041)	2.143 (1.829 to 2.586)	60 (20 to 100)
External surface (R_{se})	n/a	n/a	0.040	n/a

Note. d = thickness; λ = thermal conductivity; R = thermal resistance; μ = water-vapour resistance factor. Total resistance including surface films: R_T = 0.270 m²K/W (existing roof) and 2.413 m²K/W (with EPS). Sources: BEEN Project (2024, 2026); Bureau of Energy Efficiency (2017, 2018). R_{si} = 0.10 m²K/W for upward heat flow follows Table 2 of ISO 13788:2012 (ISO, 2012), and R_{se} = 0.04 m²K/W follows Clause 4.4.1 of ISO 13788:2012 (ISO, 2012) and Table 5 of ISO 6946:2017 (ISO, 2017). The μ values for plaster, RCC and screed are assumed working values, and the screed value is taken from a comparable material; ISO 13788:2012 Clause 4.1 calls for design values of μ from ISO 10456 or ISO 12572, which these working values do not replace. EPS values are dry-condition ranges that have not been corrected for moisture or ageing (cf. ISO 6946:2017, Clause 3.3); the base values are used throughout.

Thermal Resistance and U-Value

The thermal resistance for each layer of the roof and the overall roof U-value were calculated using the following equations:

$$R = d / \lambda \quad \text{……. (1)}$$

$$U = 1 / (Rsi + \Sigma R + Rse) \quad \text{……. (2)}$$

where d is is the thickness of the layer in metres (m), and λ is the thermal conductivity in W/m·K. For heat moving from inside the room towards the outdoors, we used

Rsi = 0.10 and Rse = 0.04 m²K/W, where the values for Rsi are given in ISO 13788:2012, Table 2, and Rse is taken from ISO 13788:2012, Clause 4.4.1, and ISO 6946:2017, Table 5. We also calculated the U-value for the EPS case using a conductivity range from 0.029 to 0.041 W/m·K, because the exact conductivity is not the same for all products and can vary depending on the product used. Thermal bridging, the fasteners, and possible effects from moisture or ageing of the EPS were not included in these calculations. The U-values are calculated following ISO 6946:2017, which is the current edition, while ISO 13788:2012 refers to the 2007 edition of ISO 6946, and this was later replaced by the 2017 edition, where the changes are described as mostly editorial (ISO, 2017, Foreword).

Heat-Loss Coefficient and Steady-State Heat Flow

The roof heat-loss coefficient and the steady-state conductive heat flow were calculated using the following equations:

$$UA = U \times A \quad \ldots\ldots\ldots\ldots (3)$$

$$Q = UA \times \Delta T \quad \ldots\ldots\ldots. (4)$$

where A is the roof area, ΔT is the difference between the indoor and outdoor air temperatures, UA represents the heat flow for each kelvin of this temperature difference, and Q is the steady-state conductive heat flow. We calculated the values using the U-values before rounding them, and then rounded the results for reporting. The heat flow was calculated for the January condition, with the indoor temperature taken as 20.0 °C and the outdoor temperature as 9.91 °C, giving a temperature difference of 10.09 K. The January indoor condition of 20.0 °C and 54.9% RH is an assumed screening condition, which we read from Figure A.1 of ISO 13788:2012 (Annex A.1, informative) using the January mean outdoor temperature of 9.91 °C (ISO, 2012). At this outdoor temperature, the indoor temperature is 20 °C, and the relative humidity for curve A, which represents normal occupancy, is 54.9%, found by linear interpolation between 35% at −10 °C and 65% at 20 °C. Annex A.1 is meant for heated dwellings and offices where the indoor conditions are not defined in another way, and Figure A.1 uses the daily mean outdoor temperature, although here we use the monthly mean temperature, similar to what is done in the worked examples in Annex B of the standard. The worked example in Table C.1 of the standard gives normal-occupancy humidity values that are 10 percentage points lower than curve B, which would give 49.9% at this temperature, so we also include this condition in the sensitivity check in Table 8. The indoor condition was not measured in our study, so the calculated heat flows depend on the assumption that the room is kept at 20 °C.

Monitoring Conditions

Three identical HTC-2 digital thermometer-hygrometers were used to record air temperature and relative humidity at three different stations, which were Room A (the main bedroom, with an area of 15.61 m², where the instrument was placed on an interior partition wall at 1.0 m height), Room B (the second bedroom, with an area of 10.03 m², placed on an interior partition wall at 0.8 m height), and the outdoor balcony, where the instrument was kept under the balcony slab in a shaded and ventilated place protected from rain. The readings were taken manually at 20 scheduled times each day over 15 days, from 21 August to 4 September 2026, with hourly readings between 06:00 and 23:00, and two additional readings at 02:00 and 05:00 during the night. Out of the 300 scheduled readings for each station, the same three readings were missed at all stations, at 22:00 and 23:00 on 27 August and at 02:00 on 28 August.

The instruments have a resolution of 0.1 °C for temperature and 1% RH for relative humidity, while their stated accuracy is ±1.0 °C and ±5 to ±10% RH, and they were not calibrated against a traceable standard. Before placing them at the monitoring locations, all three units were kept side by side and readings were taken 13 times over around 3.5 hours, with the positions of the units swapped once during this check. Their temperature readings were within 0.2 K of each other, and the RH readings were within 3 percentage points, under the conditions of about 25 °C and 71 to 76% RH. This check only showed the agreement between the instruments under one set of conditions, so it was not a calibration, and we did not apply any correction to the recorded readings.

Each room was analysed separately, where the means, standard deviations and ranges were calculated from the valid readings, and the two rooms were compared using the 297 pairs of readings taken at the same time. Since more readings were taken during the daytime compared with the longer gaps overnight, the means were also calculated again by giving each reading a weight based on the time interval it represents, using 3 h for the 02:00 reading, 2 h for the 05:00 and 23:00 readings, and 1 h for all the other readings, as an additional check. The unweighted mean for each room is used as the indoor condition during the monsoon period, while the unweighted outdoor mean is used as the monsoon outdoor condition. We did not combine the two rooms into one indoor value. The indoor–outdoor temperature differences were 0.9 K for Room A and 0.6 K for Room B, which are roughly the same size as the stated accuracy of the instruments, so we treat the monsoon condition as near-isothermal rather than considering these differences to be a measured temperature gradient. Roof-surface temperature and heat flux were not measured during the monitoring, which means the monitoring data provide the boundary conditions only and do not validate the thermal calculation.

Condensation-Risk Screening (ISO 13788/Glaser Method)

The Glaser method (ISO, 2012, Clause 6) was used for the roof assembly shown in Table 1, both for the case without EPS and the case with EPS, and the same boundary conditions were kept for both cases. The temperature at each interface is calculated based on the cumulative thermal resistance ΣRi of the layers from the room-side surface up to that interface:

$\theta i = \theta in - (\theta in - \theta out) \times (Rsi + \Sigma Ri) / RT$ …….. (5)

The vapour pressure at an interface is calculated by neglecting the surface vapour resistances and using the equivalent air-layer thickness sd = μd, as follows:

$pi = pin - (pin - pout) \times (\Sigma sd,i) / (\Sigma sd)$ …….. (6)

The saturation vapour pressure (Pa), where θ is in °C, is calculated for temperatures of θ ≥ 0°C using Formula (E.1) in ISO 13788:2012 (Annex E, informative):

$psat(\theta) = 610.5 \cdot \exp[\ 17.269\ \theta / (237.3 + \theta)\ ],\ \ \theta \geq 0\ °C$ …….. (7)

In Equations (5) and (6), θin and θout are the indoor and outdoor air temperatures, and RT is the total thermal resistance including the surface films. Similarly, p_{in} and p_{out} are the indoor and outdoor vapour pressures, while $\Sigma s_{d,i}$ and Σs_d represent the cumulative and total equivalent air-layer thicknesses. The indoor vapour pressure is calculated as $p_{in} = (RH_{in}/100) \times p_{sat}(\theta_{in})$, and the outdoor vapour pressure is calculated in the same way using the outdoor condition. Equation (5) follows the interface-temperature relation in Formula (12) of ISO 13788:2012, but it is written starting from the room side, while Equation (6) follows the straight-line vapour-pressure profile described in Clause 6.4.5. Interstitial condensation is indicated when $p_i > p_{sat}(\theta_i)$, and surface condensation is indicated when the room-side surface temperature falls below the indoor dew-point temperature. The margin that we report is $p_{sat} - p$. The critical indoor RH means the lowest indoor relative humidity, with the temperatures and outdoor vapour pressure kept fixed, at which a particular criterion is reached, and surface condensation and interstitial condensation are checked separately.

For the room-side surface, we used two different criteria. The first is a surface RH of 100%, where surface condensation occurs, and ISO 13788:2012 explicitly applies this limit to elements with low thermal inertia in Clause 5.4. The second is a surface RH of 80%, which is the critical value recommended by the standard for the monthly mean surface RH to avoid mould growth

when there is no national value available (Clauses 5.1 and 5.3). These two values are used as screening criteria for monthly mean conditions, so they should not be understood as a guarantee that condensation or mould growth will not happen. The temperature factor and the surface relative humidity are calculated as follows:

$$fRsi = (\theta si - \theta out) / (\theta in - \theta out) \text{ …….. (8)}$$

$$\varphi si = 100 \times pin / psat(\theta si) \text{ …….. (9)}$$

where θ_{si} is the room-side surface temperature. Equation (8) follows Clause 3.1.2 of ISO 13788:2012, where the temperature factor is defined using the internal operative temperature, although in our calculation the indoor air temperature is used as an approximation. For a plane element, $f_{Rsi} = 1 - R_{si}U$, as given in Clause 5.3, and this gives the same January values reported below.

We used two different internal surface resistances because ISO 13788:2012 gives different values for different types of assessment. For the surface condensation and mould checks, Rsi = 0.25 m²K/W, following Clause 4.4.1, which specifies this value for condensation or mould growth assessment on opaque surfaces when there is no national standard. This value is intended to represent the effects of corners, furniture, curtains or suspended ceilings (ISO, 2012). We did not find a Nepalese standard that specifies a different value. Since this is a conservative value, the calculated January surface temperatures of 14.0 and 19.0 °C are used only as screening values, rather than being treated as the actual roof-surface temperatures. For the interstitial condensation check and the U-value calculation, we used Rsi = 0.10 m²K/W, which is the value for upward heat flow given in Table 2 of ISO 13788:2012, and Clause 4.4.1 requires this value for assessing interstitial condensation (ISO, 2012). The external surface resistance was kept at Rse = 0.04 m²K/W throughout the calculations (ISO, 2012, Clause 4.4.1; ISO, 2017, Table 5).

Each interstitial condensation run follows the temperature and vapour-pressure profiles described in Clauses 6.4.4 and 6.4.5, for one condition at a time. However, it does not include the 12-month balance of condensation and evaporation described in Clauses 6.2 and 6.4.3, or the reporting categories given in Clause 6.5, so the results should not be taken as a finding that the roof is free from interstitial condensation according to that clause. The EPS layer has a thermal resistance of R = 2.14 m²K/W, which is higher than the 0.25 m²K/W limit above which Clause 6.4.1 recommends dividing a layer into notional sub-layers. We also checked the EPS by dividing it into nine equal sub-layers, and the smallest margin was still found at the outer face, giving the same result as the original calculation.

For the layers that were not included in the model, we carried out an additional bounding check. In this check, a vapour-tight layer, such as a waterproofing membrane, was placed at the outer face of the roof assembly. This means the vapour pressure within the assembly is kept at the indoor vapour-pressure value, so condensation is indicated if p_{in} is higher than the saturation vapour pressure at the outer-face temperature. The corresponding critical indoor RH is calculated as $p_{sat}(\theta_{outer})/p_{sat}(\theta_{in}) \times 100$. The added layer was assumed to have negligible thermal resistance. In terms of ISO 13788, this layer would create a condensation interface, and the check only shows whether condensation would start at that location, rather than estimating how much condensation would occur (Clause 6.4.6).

Results

Thermal Performance

The EPS layer adds a thermal resistance of 2.14 m²K/W to the existing roof assembly, which has a resistance of 0.27 m²K/W when the surface films are also included. After adding the EPS, the calculated U-value goes down from 3.70 to 0.41 W/m²K, which is a reduction of 88.8%. Since the thermal conductivity of EPS can vary from 0.029 to 0.041 W/m·K, we also consider this range, and the U-value is then between 0.35 and 0.48 W/m²K, giving a reduction of 87.1 to 90.5%. Under the January condition, the steady-state conductive heat flow through the roof area of 25.64 m² is reduced by about 850 W, decreasing from 956 W to 107 W, and the heat-loss coefficient also falls from 94.8 to 10.6 W/K, as presented in Table 2. These calculations only consider conductive heat flow through the roof, since thermal mass, internal heat gains and infiltration are not included in the model.

Table 2

Key Thermal and Condensation Results for the Existing Roof and the 75 mm EPS Retrofit

Parameter	Existing roof	75 mm EPS retrofit
U-value (W/m²K)	3.70	0.41
Reduction in U-value (%)	–	88.8
January steady-state heat flow, ΔT = 10.09 K, A = 25.64 m² (W)	956	107
January internal roof-surface temperature (°C)	16.3	19.6
Condensation indicated (simplified assembly), monsoon and January screening	No	No
January surface RH, R_{si} = 0.25 m²K/W (%); mould-risk limit 80%	80.3	58.4
Sensitivity: U-value across EPS λ = 0.029 to 0.041 W/m·K (W/m²K)	–	0.35 to 0.48

Note. Heat flow uses unrounded U-values (3.696 and 0.414 W/m²K); using the rounded 0.41 gives about 106 W. The roof-surface temperature uses R_{si} = 0.10 m²K/W, consistent with the U-value. Supporting values: total resistance 0.27 and 2.41 m²K/W; heat-loss coefficient UA 94.8 and 10.6 W/K (9.0 to 12.2 W/K across the conductivity range). Condensation result applies to the simplified assembly of Table 1.

Internal Roof-Surface Temperature

The calculated January temperature profile is given in Table 3 and Figure 1. The retrofit raises the room-side roof-surface temperature from 16.3 to 19.6 °C, an improvement of 3.3 K. About 89% of the indoor-outdoor temperature difference then falls across the EPS, and the plaster and slab stay close to room temperature. The difference between room air and roof surface decreases from 3.7 K to 0.4 K.

Table 3

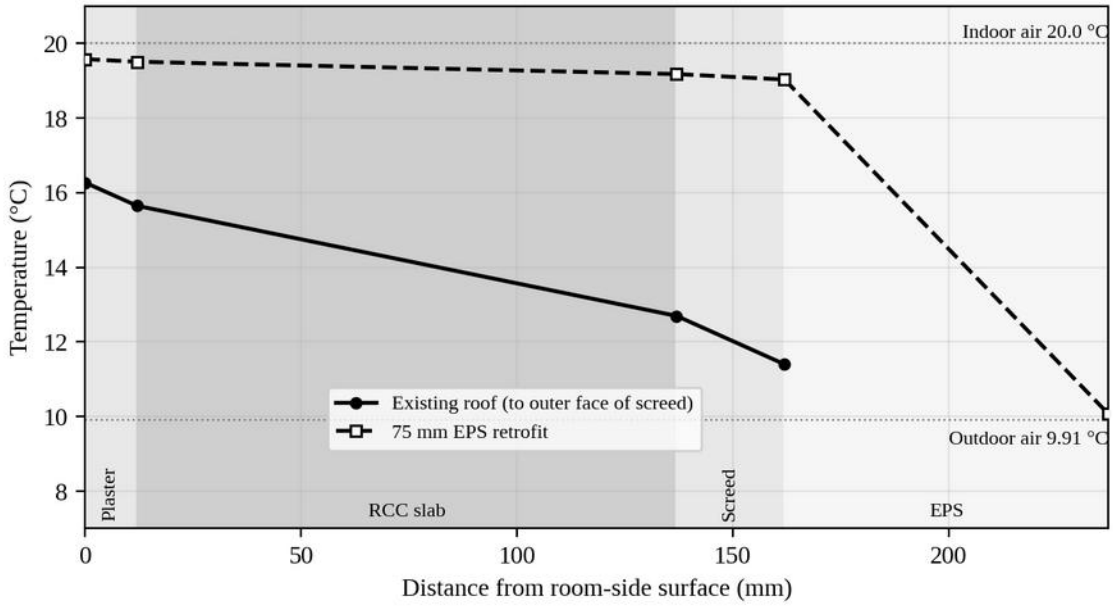
Calculated January Temperature Profile Through the Roof (°C)

Location	Existing roof	75 mm EPS retrofit
Internal surface	16.27	19.58
Plaster / RCC	15.65	19.51
RCC / screed	12.70	19.18
Screed / EPS	n/a	19.04
External face of roof build-up	11.40	10.08
Outdoor air	9.91	9.91

Note. Indoor air 20.0 °C, outdoor air 9.91 °C, R_{si} = 0.10 m²K/W.

Figure 1

January Temperature Profile Through the Existing and Retrofitted Roof



Note. Calculated from Equation (5) with the Table 1 inputs. The existing-roof line ends at the outer face of the screed.

Monitored Monsoon Conditions

The two rooms showed quite similar conditions, as presented in Table 4, where Room A had an average temperature of 27.13 °C and 67.5% RH, while Room B had 26.77 °C and 69.8% RH, compared with the outdoor conditions of 26.22 °C and 72.6% RH. From the 297 pairs of readings taken at the same time, Room A was on average 0.37 K warmer than Room B, with an SD of 0.43 K and a range from −2.6 to +1.7 K, and it was also 2.3 RH points drier, with an SD of 1.2 points. These differences are still within the stated accuracy of the instruments, and the side-by-side check also showed that the RH readings between the units could differ by up to 3 points, so we do not treat these as actual differences caused by the rooms themselves. When the readings are weighted according to their time intervals, the indoor mean values change by 0.04 K or less and by 0.3 RH points or less, which is a very small change. The outdoor mean, however,

becomes 25.73 °C and 73.9% RH, because the outdoor air was cooler during the night, at around 23 °C compared with about 28 °C during the day, and there were also fewer readings available for the night-time period. Finally, the mean values for each room were used as the respective indoor monsoon conditions for that room, as given in Table 5.

Table 4

Monitored Air Temperature and Relative Humidity, 21 August to 4 September 2026

Station	n	Temperature (°C), mean ± SD (min–max)	RH (%), mean ± SD (min–max)	Vapour pressure (Pa)
Room A (primary bedroom)	297	27.13 ± 1.12 (24.3–29.4)	67.5 ± 2.2 (61–72)	2,424
Room B (second bedroom)	297	26.77 ± 1.04 (24.4–30.3)	69.8 ± 2.4 (58–73)	2,454
Outdoor balcony	297	26.22 ± 2.75 (21.7–32.7)	72.6 ± 8.2 (54–86)	2,471
Room A − Room B (paired)	297	+0.37 ± 0.43 (−2.6 to +1.7)	−2.3 ± 1.2 (−5 to +5)	–

Note. Unweighted means of valid readings; SD = sample standard deviation; n = valid readings (paired readings in the last row). Vapour pressure is calculated from the mean temperature and mean RH, as used in the screening. Stated instrument accuracy: ±1.0 °C and ±5 to ±10% RH; the instruments were not calibrated against a traceable standard.

Condensation-Risk Screening

Neither roof shows surface or interstitial condensation under either screening condition for the simplified assembly, and this is the same for both monitored rooms, as shown in Tables 5 to 7. Under the monsoon condition, the indoor and outdoor air temperatures are different by less than 1 K, while the indoor vapour pressure, which is 2,424 Pa in Room A and 2,454 Pa in Room B, is slightly lower compared with the outdoor value of 2,471 Pa, and the indoor dew point is around 20.6 to 20.8 °C. The full interface tables are provided for Room A in Tables 6 and 7 and Appendix A, while the results for Room B are shown in Table 5 and are a little less favourable, for example, the surface RH is 71.2% compared with 69.7%, and the smallest interstitial margin for the existing roof is 949 Pa instead of 960 Pa. In January, the situation is different because the indoor vapour pressure is higher than outdoors, with 1,283 Pa indoors and 899 Pa outdoors, and the room-side margin increases from 315 Pa for the existing roof to 915 Pa after the retrofit is applied. The January surface RH for the existing roof also reaches the 80% mould-risk limit, as shown in Table 6.

Table 5

Monsoon Screening Results for Each Monitored Room

Indicator	Room A, existing	Room A, retrofit	Room B, existing	Room B, retrofit
Surface temperature (°C)	26.59	27.04	26.44	26.72
Surface margin, $p_{sat} - p$ (Pa)	1,055	1,148	995	1,051
Surface RH (%)	69.7	67.9	71.2	70.0
Critical indoor RH, surface RH = 100% (%)	96.9	99.5	98.1	99.7
Critical indoor RH, surface RH = 80% (%)	77.5	79.6	78.5	79.7
Smallest interstitial margin (Pa)	960	936	949	934
Margin with vapour-tight layer at outer face (Pa)	1,007	983	966	951

Note. Indoor condition from each room's monitored means (Room A: 27.13 °C, 67.5% RH; Room B: 26.77 °C, 69.8% RH); outdoor 26.22 °C, 72.6% RH. Surface rows use R_{si} = 0.25 m²K/W; interstitial rows use R_{si} = 0.10 m²K/W. Indoor dew points are 20.6 °C (Room A) and 20.8 °C (Room B). Using time-weighted outdoor and indoor means, all monsoon margins stay above about 850 Pa.

Table 6

Surface-Condensation and Mould-Risk Screening Indicators for the Existing and Retrofitted Roof

Indicator	Monsoon (Room A), existing	Monsoon (Room A), retrofit	January, existing	January, retrofit
Surface temperature (°C)	26.59	27.04	14.00	19.02
Surface margin, $p_{sat} - p$ (Pa)	1,055	1,148	315	915
Surface RH (%)	69.7	67.9	80.3	58.4
Temperature factor f_{Rsi} (–)	n/a	n/a	0.41	0.90
Critical indoor RH, surface RH = 100% (%)	96.9	99.5	68.4	94.1
Critical indoor RH, surface RH = 80% (%)	77.5	79.6	54.7	75.3

Note. R_{si} = 0.25 m²K/W; same boundary conditions for both roofs (monsoon: monitored means for Room A; January: assumed screening values of 20.0 °C and 54.9% RH from ISO 13788 Annex A.1, Figure A.1, curve A). f_{Rsi} is not reported for the monsoon because the indoor–outdoor temperature difference (0.9 K) is too small for a meaningful ratio. Surface RH is given to one decimal because the existing roof is close to the 80% limit.

Against the 80% mould-risk limit, the January surface RH of the existing roof (80.3%) is at the limit: it exceeds 80% by 0.3 points, and the limit is reached at 54.7% indoor RH, 0.2 points below the assumed 54.9%. The temperature factor required to meet the limit at this condition is $f_{Rsi,min}$ = 0.411 (Clause 5.3 of ISO 13788:2012), against 0.406 for the existing roof, so the existing roof should be read as at the screening limit and not clearly on either side of it. With the retrofit the surface RH is 58.4% and the limit is reached at 75.3% indoor RH. The temperature factor f_{Rsi} rises from 0.41 to 0.90.

Interstitial Margins and Bounding Check for Omitted Layers

For the simplified assembly, the smallest interstitial margin for the retrofitted roof is found at the outer face of the build-up, with 936 Pa in the monsoon condition for Room A (and 934 Pa in Room B), while in January it is 335 Pa. For the existing roof, these margins are 960 Pa for Room A and 949 Pa for Room B in the monsoon, and 448 Pa in January, as given in Table 7. If a vapour-tight layer was present at the outer face, the vapour pressure at this location would become the same as the indoor value, which is 1,283 Pa in January. The saturation pressure at the outer face is 1,347 Pa for the existing roof at 11.4 °C, while for the retrofit it is 1,234 Pa at 10.1 °C, so the margin left is 64 Pa for the existing roof but becomes negative at −49 Pa for the retrofit, meaning condensation would be indicated in the retrofit case. The corresponding critical indoor RH values are 57.7% and 52.8%, and when compared with the assumed January indoor RH of 54.9%, it is 2.8 points below the threshold for the existing roof but 2.1 points above the threshold for the retrofit. Under the monsoon condition, however, the bounding margins remain above 950 Pa in both rooms, as shown in Table 5.

Table 7

Smallest Interstitial Margins (Pa) and Bounding Check for an Omitted Vapour-Tight Layer

Roof	Monsoon (Room A), simplified	January, simplified	January, vapour-tight layer at outer face	Critical indoor RH with vapour-tight layer (%)
Existing	960	448	64	57.7
75 mm EPS retrofit	936	335	−49	52.8

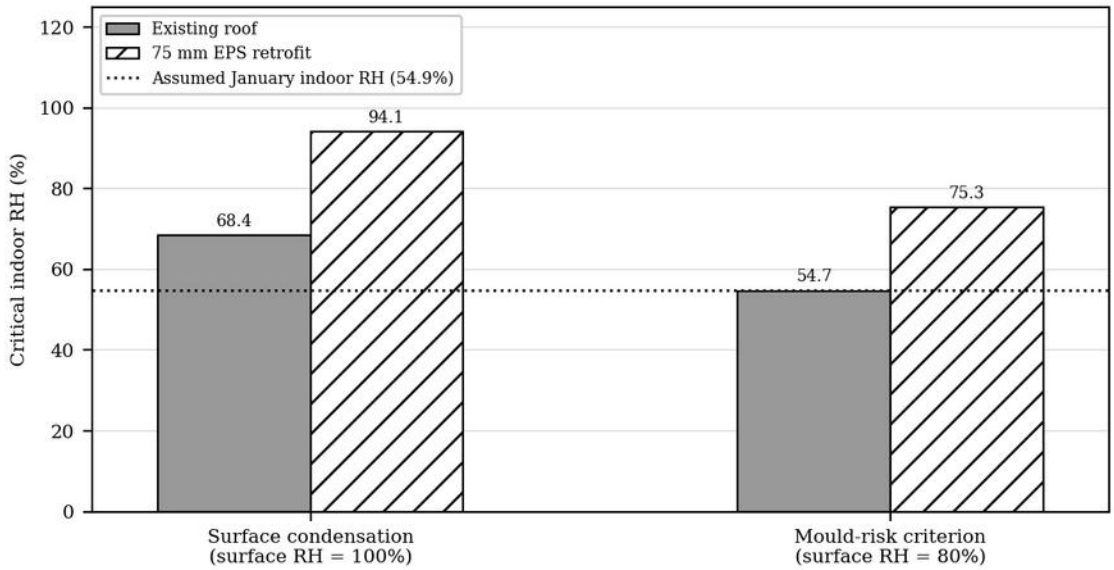
Note. Margin = $p_{sat} - p$ at the outer face of the build-up, R_{si} = 0.10 m²K/W. The vapour-tight layer is a bounding assumption with no thermal resistance, not a modelled product. For Room A, the monsoon margins with a vapour-tight layer are 1,007 Pa (existing) and 983 Pa (retrofit); Room B values are in Table 5. Full interface values are in Appendix A.

Indoor RH Sensitivity

In January, the indoor RH level where surface condensation first starts to be indicated increases from around 68.4% for the existing roof to about 94.1% when 75 mm EPS is added, which is an increase of about 26 percentage points, as shown in Figure 2. These values are calculated screening thresholds and are not actual measurements, and they are based on the screening surface temperatures of 14.0 °C for the existing roof and 19.0 °C for the retrofit, using Rsi = 0.25 m²K/W. In both roof cases, the room-side surface is the one that controls the result, because the interstitial thresholds for the simplified assembly are higher, at around 76.5% and 97.6%, and these are calculated using Rsi = 0.10 m²K/W, both at the plaster/RCC interface. For the existing roof, the interstitial threshold stays roughly between 76% and 79% even when the assumed μ values are changed, with plaster from 5 to 20, RCC from 20 to 130, and screed from 15 to 35, so this threshold still remains higher than the surface threshold. The surface thresholds, meanwhile, depend only on the surface temperature and are not affected by the assumed vapour resistance factors.

Figure 2

Critical Indoor Relative Humidity for Surface Criteria in January



Note. Indoor air at 20.0 °C; R_{si} = 0.25 m²K/W. Data from Table 6. The dotted line marks the assumed indoor RH (54.9%, from ISO 13788 Annex A.1, Figure A.1, curve A) used as the January screening condition.

Sensitivity to January Indoor Temperature and RH

Since the January indoor condition is an assumed value, in Table 8 we change one factor at a time, where the indoor temperature is varied from 16 to 20 °C while keeping the base RH at 54.9%, and the indoor RH is changed from 45 to 59.9% at 20 °C. The 49.9% case comes from taking normal occupancy as 10 points below curve B, as given in Table C.1 of the standard, while 59.9% represents curve B for high occupancy at 9.91 °C. The percentage reduction in heat flow remains at 88.8% in all these cases, because the area and ΔT are the same for both roofs, and the heat flow changes according to the temperature difference, decreasing within a range of 577 to 956 W for the existing roof and 65 to 107 W for the retrofit. The surface RH for the retrofit stays around 57 to 58% when the temperature goes from 16 to 20 °C, but for the existing roof the surface RH increases from 69.4% at 16 °C to 80.3% at 20 °C, and the vapour-tight margin for the retrofit changes from positive to negative between 19 °C, where it is 27 Pa, and 20 °C, where it becomes −49 Pa. The humidity cases show a more important change, because at 49.9% RH the existing roof has a surface RH of 73.0%, which is below the 80% limit, and the vapour-tight margin for the retrofit is small but still positive at 68 Pa. At 59.9% RH, the existing roof surface RH reaches 87.6% and clearly goes above the limit, while the vapour-tight margin becomes negative for both roofs, at −52 and −166 Pa. So, the conclusions about U-value, heat flow and surface condensation remain the same across the tested range, but the mould-risk result for the existing roof and the vapour-tight bounding check are dependent on the indoor humidity that has been assumed.

Table 8

January Sensitivity to Indoor Temperature and Relative Humidity (One Factor at a Time)

Indoor condition	Heat flow, existing / retrofit (W)	Surface RH, existing / retrofit (%)	Vapour-tight margin, existing / retrofit (Pa)
16 °C, 54.9% RH	577 / 65	69.4 / 57.0	298 / 231
17 °C, 54.9% RH	672 / 75	72.0 / 57.4	245 / 166
18 °C, 54.9% RH	767 / 86	74.7 / 57.7	189 / 98
19 °C, 54.9% RH	862 / 97	77.5 / 58.0	129 / 27
20 °C, 54.9% RH (base)	956 / 107	80.3 / 58.4	64 / −49
20 °C, 45% RH	956 / 107	65.8 / 47.8	296 / 182
20 °C, 49.9% RH	956 / 107	73.0 / 53.0	181 / 68
20 °C, 59.9% RH	956 / 107	87.6 / 63.7	−52 / −166

Note. Outdoor 9.91 °C, 73.7% RH; Table 1 assembly. Surface RH uses R_{si} = 0.25 m²K/W; the vapour-tight margin is p_{sat} at the outer face minus the indoor vapour pressure (R_{si} = 0.10 m²K/W). At fixed RH, a lower indoor temperature also lowers the indoor vapour pressure, which is an assumption; the RH in a less-heated room could be higher. The 54.9% RH rows use curve A of ISO 13788:2012 Figure A.1 (base case). The 49.9% row corresponds to normal occupancy taken as 10 points below curve B (Table C.1 of the standard), and the 59.9% row to curve B (high occupancy).

Discussion

Thermal Performance

For the residence we studied, the retrofit reduces the conductive heat loss through the roof in winter by around nine-tenths under the January condition. Since the area and ΔT are the same for both roofs, the percentage reduction in heat flow is also the same as the reduction in U-value. The main uncertainty in this calculation comes from the EPS conductivity, but even when the dry-condition range is considered, the overall conclusion does not change. The baseline U-value of 3.70 W/m²K is quite close to the BEEN reference value of 3.564 W/m²K for a Kathmandu roof made with 125 mm RCC, screed and tile (BEEN Project, 2026). This gives some indication that the input values are reasonable, although both values use similar design assumptions, so it cannot be treated as an independent validation. The calculated heat flows are also not estimates of heating demand or actual energy savings, and they assume that the room is kept at 20 °C. Another point is that the dry-condition conductivity values may be too optimistic if moisture is absorbed by the EPS (Khoukhi et al., 2019).

Room-Side Surface

When the room-side roof surface is raised to within 0.4 K of the room air temperature, this indicates that the cold-surface effect for occupants below the roof becomes smaller, although thermal comfort itself was not assessed in this study. Without insulation, the room-side surface of the slab moves closer to the outdoor temperature, whereas adding EPS helps to keep the surface temperature close to the room temperature.

Condensation Screening

The monsoon condition is a relatively mild test for condensation. The indoor dew points, which are around 20.6 °C in Room A and 20.8 °C in Room B, remain well below all the interface temperatures, so condensation is not indicated in either roof assembly or in either room, and this

result should not be considered as evidence that the retrofit provides a benefit. The January condition gives more useful information for comparison. In both roofs, the room-side surface is the main controlling location, and the retrofit increases the indoor RH threshold for condensation from about 68% to around 94%. A threshold close to 94% means that the room-side surface is still far from condensing under the screening condition, but it does not mean that such a high indoor humidity is expected in the actual house. The RH sensor accuracy of ±5 to ±10 points is small compared with the difference between the monitored indoor RH values, which are 67.5% in Room A and 69.8% in Room B, and the monsoon condensation thresholds of 96.9 to 99.7%. However, this sensor accuracy is not small when compared with the difference to the 80% mould-risk limit, which is reached at an indoor RH of 77.5 to 79.7%, only around 9 to 12 points higher than the monitored values. Therefore, based on this evidence, the monsoon mould-risk margin cannot be considered fully secure.

The mould-risk condition is more critical for the existing roof. Its surface RH reaches the 80% limit at an indoor RH of 54.7%, which is 0.2 points lower than the assumed screening value of 54.9%, meaning that the January surface RH of the existing roof, at 80.3%, is already around the limit. This difference is within the ±5 to ±10 point accuracy of the RH sensors used for monitoring and also within the uncertainty of the assumed indoor condition, so the possibility of mould risk on the existing roof's room-side surface in January cannot be dismissed. The 80% value is used as a screening criterion for monthly mean surface RH, rather than a guarantee that mould will or will not occur. With the retrofit, this threshold increases to 75.3% indoor RH, which is around 20 points above the screening value. Mould growth also depends on the exposure time, the type of substrate and cleaning conditions, and these factors are not covered by a monthly-mean screening approach. Adding EPS also lowers the temperature at the outer face of the roof build-up from 11.4 to 10.1 °C in January, which reduces the smallest interstitial margin at that location from 448 to 335 Pa. Even so, the margin remains positive.

Monitored Conditions

The two monitored rooms showed quite similar conditions during the monsoon. The mean differences between them, which are 0.37 K and 2.3 RH points, are within the stated accuracy of the instruments, and the side-by-side check before the instruments were deployed also showed that the RH readings between units could differ by up to 3 points, so these differences are not taken as actual effects caused by the rooms. Room B gave slightly less favourable monsoon screening results, for example, the smallest interstitial margin was 949 Pa compared with 960 Pa for the existing roof, but the overall conclusions remain the same for both rooms. The event notes also show that windows and doors were open at some times, which means both rooms were naturally ventilated. The mean indoor and outdoor conditions were fairly close, with unweighted differences of 0.9 K and 0.6 K, although the indoor air temperature varied much less than the outdoor air, with standard deviations of about 1.1 K and 2.8 K, respectively. So, the monitoring mainly describes the monsoon conditions in two naturally ventilated rooms only. It does not tell us what the winter indoor conditions would be in a house using portable heaters, and it also does not validate the calculated U-values or the January results.

Omitted Layers

Since the properties of the complete overdeck layers were not available, we assessed a simplified roof assembly instead. Under the monsoon condition, the saturation pressure at the outer-face temperature for the retrofit, which is 3,406 Pa, is higher than the indoor vapour pressure of 2,424

to 2,454 Pa, so adding a vapour-tight layer at this location would not by itself lead to condensation according to the calculation. The January result is different, however, because the saturation pressure at the retrofit's outer-face temperature is 1,234 Pa, which is lower than the indoor vapour pressure of 1,283 Pa. This means that a vapour-tight layer at that face would be predicted to cause condensation, with a margin of −49 Pa and a critical indoor RH of 52.8%, which is below the assumed value of 54.9%. For the existing roof, the margin is positive but quite small at 64 Pa. The sensitivity check also shows how narrow these margins can be, because at 20 °C the vapour-tight margin for the retrofit is 182 Pa at 45% indoor RH, 68 Pa at 49.9%, −49 Pa at 54.9%, and −166 Pa at 59.9%, as given in Table 8. For this reason, the position and vapour resistance of any waterproofing layer need to be assessed separately as part of the complete roof before the 75 mm EPS retrofit is specified. These results should not be applied directly to higher indoor humidity, months that were not modelled, or the whole annual cycle. The thresholds presented here are for the simplified assembly in Table 1 and should not be treated as limits for the complete roof as it is actually built.

Practical Implications

The staining, moss, algae and screed delamination observed on the existing roof point towards water and weathering coming from outside, which are not covered by a diffusion-only calculation, so these defects should not be taken as evidence of interstitial condensation. They should be inspected and repaired before installing insulation, rather than simply being covered by it. The overdeck roof options listed in the BEEN manual include closed-cell insulation materials such as polyurethane, polyisocyanurate and extruded polystyrene, while EPS was kept in this study because it is the material being investigated. Before it is specified, the EPS grade, moisture uptake and compressive performance should be checked, since the conductivity range used here, from 0.029 to 0.041 W/m·K, represents dry-condition values.

Limitations

The results are based on one house, so only the general roof type, which is a flat uninsulated RCC roof, can be considered representative. The assessment uses steady-state calculations with single boundary conditions, and only one insulation thickness of 75 mm was considered. We did not carry out an annual energy simulation, estimate actual energy savings, or predict long-term moisture behaviour. Summer solar gain, thermal mass and day-night temperature changes were also not modelled, so this study does not provide information about the cooling benefit of the overlay. The assessed roof assembly does not include the waterproofing layer, mastic, geotextile, mesh-reinforced protective screed or tile finish, because their properties were not available, and the μ values used for the existing layers are assumed working values, which affect the interstitial results. The January indoor condition of 20 °C and 54.9% RH was taken from curve A for normal occupancy in Figure A.1 of the informative Annex A.1 of ISO 13788:2012, rather than being measured inside the house. The worked example in Table C.1 of the standard would give an RH of 49.9%, and this difference changes the mould-risk and vapour-tight results, as shown in Table 8. The actual winter indoor temperature in a house heated with portable heaters may be lower, which would reduce the heat flows reported here, and the actual RH may also be different. The sensitivity check in Table 8 changes one factor at a time, so it does not represent all these actual conditions.

The monitoring covered only 15 monsoon days in two naturally ventilated rooms of one house. Readings were taken manually, with 20 readings per day that were not evenly spaced in time,

using instruments that were not calibrated against a traceable standard, and the side-by-side check was carried out under only one condition. The sensors were also placed at different heights, around 1.0 m and 0.8 m, on interior partition walls. Because of these limitations, the monitoring cannot support conclusions about winter or annual conditions, and it cannot be used to validate the calculated U-values.

The condensation screening is a simplified application of ISO 13788:2012. The interstitial check uses a single-condition calculation rather than the 12-month condensation and evaporation balance described in Clause 6, so it cannot show whether moisture would build up over a year or dry out during the dry season. The method assumes one-dimensional, steady-state vapour diffusion and constant material properties, and it does not include moisture storage in hygroscopic materials, capillary suction and liquid transport, air movement or rain absorption, as discussed in Clauses 1, 6.2 and 6.3. The standard also explains in its Introduction that the results are less reliable for structures with high thermal and moisture capacity, such as this RCC roof, and Clause 6.3 says that the method is not intended for building elements where rainwater is absorbed. This is an important concern for the existing roof because staining, moss and delamination were observed.

The January outdoor condition is based on a typical-year monthly mean. Clause 4.2.2 specifies monthly means that are likely to occur once in 10 years, or an average-year mean reduced by 2 K when such data are not available, while Clause 4.2.3 d) recommends using an equivalent outdoor temperature for roofs, which can be simplified as the air temperature minus 2 K. Neither of these adjustments was applied in this study. To give an indication of their possible effect, when the outdoor air temperature is reduced by 2 K while the outdoor RH is kept at 73.7% and the indoor RH is read again from Figure A.1 as 52.9%, the smallest interstitial margin decreases from 448 to around 417 Pa for the existing roof and from 335 to around 295 Pa for the retrofit. At the same time, the January surface RH of the existing roof rises to about 84%. The interstitial margins still remain positive, but the existing roof exceeds the 80% mould-risk limit more clearly. Finally, the monsoon condition is based on 15-day mean values, rather than monthly means derived using the methods in ISO 15927-1.

Conclusion

For the top-floor roof we studied, adding a 75 mm EPS overlay changes the calculated steady-state results in several ways. The U-value decreases from 3.70 to 0.41 W/m²K, which is a reduction of 88.8%, and across the EPS conductivity range it stays between 0.35 and 0.48 W/m²K. Under the January steady-state condition, the conductive heat flow through the 25.64 m² roof decreases from around 956 W to about 107 W, while the room-side roof surface temperature increases from approximately 16.3 to 19.6 °C. For the simplified assembly, no surface or interstitial condensation is indicated under the January screening condition or the monsoon conditions in either of the monitored rooms. However, in January the room-side surface RH of the existing roof is 80.3%, which is at the 80% mould-risk screening limit, while with the retrofit it decreases to 58.4%. The January interstitial margin at the outer face of the EPS is 335 Pa, but if a vapour-tight layer is added at this location, condensation would be indicated, with a margin of −49 Pa and a critical indoor RH of 52.8%. In the sensitivity check at 20 °C, the existing roof stays below the 80% limit when the indoor RH is 49.9%, but it clearly goes above the limit at 59.9%. The bounding margin for the retrofit is positive only when indoor RH is around 52.8% or

lower, so the mould-risk and vapour-tight bounding results should not be applied to conditions with higher indoor humidity.

These results are steady-state screening results from a single house, and they do not provide annual energy savings, changes in indoor temperature or long-term moisture performance. For future work, we aim to include the 12-month calculation under ISO 13788 using design outdoor conditions, together with annual dynamic hygrothermal and energy simulations for both the existing and retrofitted roofs. The complete roof assembly should also be assessed, including the waterproofing and finish layers, and different insulation thicknesses should be studied. In addition, longer monitoring over multiple seasons with calibrated instruments should be carried out, including measurements of roof-surface temperature or heat flux.

Acknowledgments

The author would like to thank the academic supervisor for providing supervision during the study, and also the house owner and occupants for allowing access to the building and cooperating during the roof survey and monitoring work.

Funding

The author did not receive any financial support for carrying out the research, or writing the paper.

Conflict of Interest

The author declares that there is no conflict of interest related to this study.

Author Contributions

The author planned and developed the study, carried out the roof survey, collected the monitoring data, did the calculations and also wrote the manuscript.

Data Availability

The January weather data used in this study were taken from the publicly available TMYx weather file for Tribhuvan International Airport (WMO 444540) (Lawrie & Crawley, 2022). The material properties and design values were collected from the published sources which are cited in Table 1. The field monitoring data, including air temperature and relative humidity recorded at three stations from 21 August to 4 September 2026, together with the event notes, were collected by the author during the study, and the roof survey measurements were also taken by the author. These data, along with the calculation workbook used for the U-value, heat-flow, condensation-risk and sensitivity calculations, can be obtained from the author on reasonable request. However, the building location and details about the occupants will not be shared, as this is done to protect their privacy.

Ethical Approval / Consent

The building owner and occupants gave verbal consent for the roof survey and the indoor environmental monitoring to be carried out. No formal ethical review was requested from an institutional ethics committee for this study.

References

BEEN Project. (2024). *Manual on application of building insulation materials* (1st ed.). MinErgy Pvt. Ltd. https://been.minergynepal.com/resources/

BEEN Project. (2026). *Manual for energy-efficient building design* (2nd ed.). MinErgy Pvt. Ltd. https://been.minergynepal.com/resources/

Borgkvist, I. (2016). *Improving indoor thermal comfort in residential buildings in Nepal using energy efficient building techniques* (Report No. TVBH-5093) [Master's thesis, Lund University]. Lund University Publications. https://lup.lub.lu.se/student-papers/search/doc/8874136

Bureau of Energy Efficiency. (2017). *Energy Conservation Building Code 2017*. Ministry of Power, Government of India. https://beeindia.gov.in/

Bureau of Energy Efficiency. (2018). *Eco-Niwas Samhita 2018 (Energy Conservation Building Code for residential buildings), Part I: Building envelope*. Ministry of Power, Government of India. https://econiwas.com/

Chaulagain, H., Rodrigues, H., Silva, V., Spacone, E., & Varum, H. (2016). Earthquake loss estimation for the Kathmandu Valley. *Bulletin of Earthquake Engineering, 14*(1), 59–88. https://doi.org/10.1007/s10518-015-9811-5

Chaulagain, N., Baral, B., & Bista, S. R. (2019). Thermal performance of Nepalese building: A case study of Dhulikhel and Biratnagar. *Journal of the Institute of Engineering, 15*(3), 73–77. https://doi.org/10.3126/jie.v15i3.32012

Department of Urban Development and Building Construction. (2024). *Nepal national building code: NBC 206:2024: Architectural design requirements* (2nd rev.). Ministry of Urban Development, Government of Nepal. https://dudbc.gov.np/

Green Developers Nepal. (2026, August 8). *EPS insulation boards*. https://greendevelopersnepal.com/

International Organization for Standardization. (2012). *Hygrothermal performance of building components and building elements — Internal surface temperature to avoid critical surface humidity and interstitial condensation — Calculation methods (ISO 13788:2012, 2nd ed.).* https://www.iso.org/standard/51615.html

International Organization for Standardization. (2017). *Building components and building elements — Thermal resistance and thermal transmittance — Calculation methods (ISO 6946:2017, 3rd ed.).* https://www.iso.org/standard/65708.html

Khoukhi, M., Abdelbaqi, S., & Hassan, A. (2019). Yearly energy performance assessment of employing expanded polystyrene with variable temperature and moisture-thermal conductivity relationship. *Materials, 12*(18), Article 3000. https://doi.org/10.3390/ma12183000

Kulkarni, K. S., Singh, G., & Premi, R. (2024). A detailed investigation on thermal performance and energy savings of cool roof systems for composite climates of India. *Advances in Building Energy Research, 18*(5), 453–474. https://doi.org/10.1080/17512549.2024.2374553

Künzel, H., & Dewsbury, M. (2022). Moisture control design has to respond to all relevant hygrothermal loads. *UCL Open: Environment, 4*, Article 08. https://doi.org/10.14324/111.444/ucloe.000037

Lawrie, L. K., & Crawley, D. B. (2022). *Development of global typical meteorological years (TMYx)* [Data set]. Climate.OneBuilding.Org. https://climate.onebuilding.org

Meddage, D. P. P., Chadee, A., Jayasinghe, M. T. R., & Rathnayake, U. (2022). Exploring the applicability of expanded polystyrene (EPS) based concrete panels as roof slab insulation in the tropics. *Case Studies in Construction Materials, 17,* Article e01361. https://doi.org/10.1016/j.cscm.2022.e01361

Raimundo, A. M., Sousa, A. M., & Oliveira, A. V. M. (2023). Assessment of energy, environmental and economic costs of buildings' thermal insulation: Influence of type of use and climate. *Buildings, 13*(2), Article 279. https://doi.org/10.3390/buildings13020279

Subedi, R., Poudyal, K. N., & Bhattarai, N. (2026). Assessing the effectiveness of building envelope materials on existing buildings in the sub-tropical climate: A case study in Kathmandu Valley, Nepal. *Building Engineering, 4*(1), Article 4023. https://doi.org/10.59400/be4023

Thapa, S., Bhatta, R., & Rai, Y. P. (2020). Impact of climate change on heating and cooling load demand for sustaining thermal comfort in a residential building: A case study of Kathmandu Valley. In *Proceedings of the 8th IOE Graduate Conference* (Vol. 8, pp. 191–198). Institute of Engineering, Tribhuvan University.

Appendix A

Layer inputs from Table 1 give thermal resistances of 0.0166 m²K/W (plaster), 0.0791 m²K/W (RCC slab), 0.0348 m²K/W (screed) and 2.143 m²K/W (EPS), and equivalent air-layer thicknesses s_d of 0.144 m, 10.0 m, 0.75 m and 4.5 m, respectively. Tables A1 and A2 list the interface values from Equations (5) to (7) with R_{si} = 0.10 m²K/W. The EPS is treated as one layer in Table A1; a check with nine notional EPS sub-layers (ISO 13788:2012, Clause 6.4.1) gave the same smallest margin, at the outer face.

Table A1

Interface Temperatures and Vapour Pressures, January Screening Condition

	Existing roof				**75 mm EPS retrofit**			
Interface	**θ (°C)**	**p (Pa)**	**p_{sat} (Pa)**	**Margin (Pa)**	**θ (°C)**	**p (Pa)**	**p_{sat} (Pa)**	**Margin (Pa)**
Plaster / RCC	15.65	1,278	1,777	499	19.51	1,279	2,267	988
RCC / screed	12.70	926	1,468	542	19.18	1,030	2,221	1,191
Screed / EPS	n/a	n/a	n/a	n/a	19.04	1,011	2,201	1,190
Outer face of build-up	11.40	899	1,347	448	10.08	899	1,234	335

Note. Indoor 20.0 °C, 54.9% RH; outdoor 9.91 °C, 73.7% RH. In the existing roof, the outer face of the build-up is the outer face of the screed.

Table A2

Interface Temperatures and Vapour Pressures, Monsoon Screening Condition (Room A)

	Existing roof				75 mm EPS retrofit			
Interface	**θ (°C)**	**p (Pa)**	**p_{sat} (Pa)**	**Margin (Pa)**	**θ (°C)**	**p (Pa)**	**p_{sat} (Pa)**	**Margin (Pa)**
Plaster / RCC	26.74	2,424	3,509	1,085	27.09	2,424	3,581	1,157
RCC / screed	26.47	2,468	3,454	987	27.06	2,455	3,575	1,120
Screed / EPS	n/a	n/a	n/a	n/a	27.04	2,457	3,572	1,115
Outer face of build-up	26.35	2,471	3,431	960	26.24	2,471	3,406	936

Note. Indoor 27.13 °C, 67.5% RH; outdoor 26.22 °C, 72.6% RH (monitored means, Room A, the primary bedroom). In the existing roof, the outer face of the build-up is the outer face of the screed.